University of Alberta

The role of North Atlantic Current water in exchanges across the Greenland-Scotland Ridge from the Nordic Seas

by

Colin More

A thesis submitted to the Faculty of Graduate Studies and Research in partial fulfillment of the requirements for the degree of

Master of Science

Department of Physics

Spring 2011
Edmonton, Alberta

Abstract

The circulation and gradual transformation in properties of oceanic water masses is a matter of great interest for short-term weather and biological forecasting, as well as long-term climate change. It is usually agreed that the Nordic Seas between Greenland and Norway are key to these transformations since they are an important producer of dense water, a process central to the theory of the global thermohaline circulation. In this study, one component of this deep water is examined – that formed in the Nordic Seas themselves from the inflowing North Atlantic Current. Using Lagrangian particle tracking applied to a 50-year global ocean hindcast simulation, it is concluded that only about 6% of the inflowing North Atlantic Current is thus transformed, and that most of these transformations occur in boundary currents. Furthermore, it is found that the densified North Atlantic water attains only medium depths instead of joining the deep overflows. The model's poor representation of vertical mixing, however, limits the applicability of this study to deep water formation.

Acknowledgements

I wish to thank my co-supervisors, Bruce Sutherland and Paul Myers, for their infinite patience in taking me from overconfident undergraduate to budding scholar. Paul in particular endured many painful hours of questioning and misunderstanding as I slowly built my store of oceanographic knowledge up from nothing. My friends and co-workers were also indispensable assets in this, Arjen Terwisscha van Scheltinga in particular. His advice, philosophy, and knowledge (both academic and otherwise!) was of inestimable value at all stages of this degree.

I would be remiss not to acknowledge the generous financial support of NSERC. Through their excellent post-graduate scholarship program, they funded the bulk of the work in this thesis.

Finally, to my parents, Larry and Laura, and my sister, Heather: none of this would have been possible without you. Thank you.

Contents

List of Tables

List of Figures

Chapter 1

Background

1.1 Introduction

The ocean impacts all regions of the Earth significantly and in many ways. For example, its transportation of heat affects weather systems and regional climates (Bjerknes, 1969; Ueda & Yasunari, 1996; Minobe et al., 2008), its currents and tides affect international shipping and commerce (Newman, 1989; Whipple, 1980), and the nutrients it contains directly support nearly 50% of all life on the planet (National Oceanic and Atmospheric Administration, 2010). This life, in turn, is the main source of animal protein for around a billion humans, and contributes about 15% of humanity's total animal protein intake (Joint WHO/FAO Expert Consultation on Diet, Nutrition and the Prevention of Chronic Diseases, 2003). Therefore, our understanding of the oceans affects numerous aspects of our daily lives both directly and indirectly.

One of the ocean's most important aspects in terms of energy and material transport are its currents. Large-scale systems transport heat and nutrients significant distances. For example, the Gulf Stream and its northern derivatives transport energy over 8000 km from the Caribbean to Greenland, while the Antarctic Circumpolar Current runs endlessly around the entire Southern Ocean. Surface currents such as these are largely wind-driven, typically travelling at speeds of 10-20 cm/s (Knutsen et al., 2005; Hátún & McClimans, 2003; Hansen et al., 2003) and occasionally – particularlarly in the Florida Current – at 250 cm/s or greater (Voituriez, 2006; Pickard & Emery, 1990). In addition, the world's major boundary currents, such as the aforementioned Gulf Stream (east coast of the United States), the Kurushio (Japanese for "Black Tide", east of Taiwan and Japan), and the Agulhas (south of the Mozambique Channel), extend quite deep, up to 1500 meters (Stommel & Yoshida, 1972). The majority of boundary currents are, however, less extreme, with vertical extents of several hundred meters (Yashayaev & Loder, 2009; Kieke & Rhein, 2006). Volume transports vary greatly: the Antarctic Circumpolar Current carries 100-125 Sv (Nowlin Jr. et al., 1977; Orsi et al., 1995) (1 Sv = 10^6 m^3s^{-1}), while the Alaska Current through the Shelikof sea valley carries a mere 0.85 Sv[1] (Schumacher et al., 1989).

In contrast to the relatively high speeds of the wind-driven surface currents, abyssal currents (those below the pycnocline, the region where density changes relatively rapidly) are predominantly baroclinic, driven by relatively small horizontal density differences transporting water at (generally) relatively low speeds. For example, Haine et al. (1998) estimates that it takes 23 years for Antarctic Bottom Water to reach the Crozet-Kerguelen Gap in the Indian Ocean, at an average speed of $1.2 \pm 0.3\,\text{cm/s}$.

The upper and lower systems do not often strongly interact with one an-

[1] Of course, these currents share few physical or dynamical characteristics with one another besides being surface flows

other, instead generally confining their mixing to vertical diffusion and similar processes. Since the lower layers are not forced by atmospheric influences, mixing in them is relatively slow. By contrast, "measurement of the ^{90}Sr content of ocean water has revealed significant amounts at depths to 1000 m. As the only source of this isotope is presumed to be the residue from atom bombs, starting in 1954, this indicates that the rate of vertical mixing in the upper waters may be quite rapid." (Pickard & Emery, 1990). When direct interaction *does* occur, it is usually in the form of larger-scale vertical exchange rather than small-scale mixing. Thus, downwelling and upwelling form crucial links between the surface and the abyss, completing the global cycle termed the Thermohaline Circulation. This refers to the transfer of heat, salt, and other materials between different geographical locations and vertical layers. It is a key consideration to the overall health of our oceans since it serves as a renewal mechanism: rising cold, deep water brings nutrients with it, replenishing the supply contained in the surface waters (Tilstone et al., 1994; Williams & Follows, 1998), while downwelling balances the water rising from the deep (Sarmiento et al., 2004) and ventilates the deep ocean with atmospheric gasses such as carbon dioxide (Bryan & Danabasoglu, 2006; Sarmiento & Gruber, 2002; Lavery et al., 2010).

1.2 Deep Water

1.2.1 Introduction

Very dense water, such as that which needs to be formed for a deeply convective event to occur, typically has a low temperature and high salinity (see figure 1.1). In order to produce it one must therefore have some mechanism for increasing salinity (eg. high evaporation rates) and/or decreasing temperature (eg. cold temperatures, strong winds). Logically, then, if one begins with a relatively cold, saline water mass, formation of truly dense water becomes more efficient. Such conditions exist in a limited number of locations, including the Antarctic Ross and Weddell Seas[2], the Labrador Sea southwest of Greenland, and the Nordic Seas east of Greenland (Marshall & Schott, 1999).

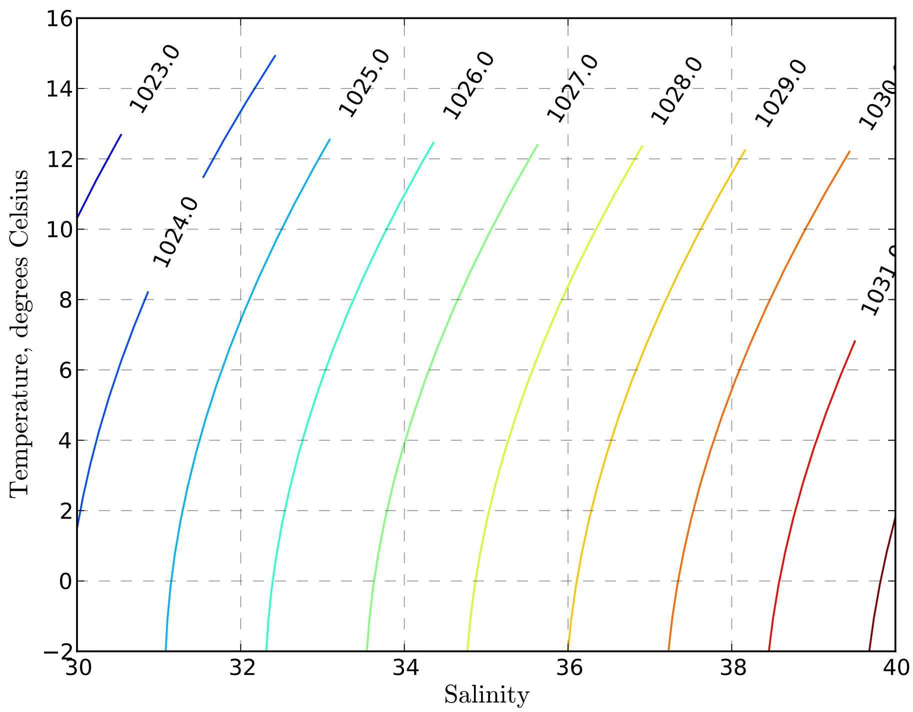

Figure 1.1: Temperature-salinity diagram for typical oceanic temperature and salinity values. Note that near the freezing point, salinity has a much greater effect on density than does temperature. Salinity, by convention, is unitless.

The Antarctic seas produce the world's densest water thanks to extremely cold, dry, and strong winds from the continent massively cooling the sea surface. Through sinking, this leads to a water mass – Antarctic Bottom Water –

[2]Named for the British explorers Sir James Clark Ross and James Weddell, respectively

with potential temperatures[3] in the range of $-2.0°C < \theta < -1.5°C$ and salinities of 34.4-34.6 (Foldvik et al., 1985). About 80% of this is formed in the Weddell Sea (Foldvik & Gammelsrød, 1988). In contrast, Labrador Sea Water tends to be rather warmer and saltier, at about 2.8°C and 34.84 (Yashayaev & Loder, 2009), due to the warmer winters in the area and the significant amounts of salt being pumped into the area by the Sub-Polar Gyre.

Only in the Nordic region, and in particular the Greenland Sea northwest of Norway, does the density of newly formed deep water approach that of Antarctic Bottom Water. The main source of transformable surface water is the inflowing North Atlantic Current, which maintains much of its high-salinity (> 35.3, Hansen & Østerhus (2000)) character even as it travels up the Norwegian coast. However, due to colder ambient air temperatures it does not maintain its initial temperature of $> 9.0°C$ (Hansen & Østerhus, 2000). Strong winds blowing off of the Greenland ice sheet during midwinter cool and evaporate the surface layers, with salinity being raised still further through such processes as brine rejection from sea ice formation. The resulting Denmark Strait Overflow Water which eventually exits the area is only slightly less dense than Antarctic Bottom Water, possessing typical values of potential temperature $\theta < 2°C$ and potential density anomaly $\sigma_0 > 27.8$ kg/m^3 (Tanhua et al., 2005).

Generally, these very dense water masses are formed in a process called deep convection. Understanding how this process occurrs in nature is important for building a model which can represent it, or for quantifying how well an existing model represents it. I will therefore discuss it in some detail here.

[3]Potential temperature is the temperature a parcel of water would have if brought to a specified reference level, usually the surface

1.2.2 Deep Convection

Generally, deep convection occurs in three stages: preconditioning of the surface layers, the actual convection event, and export of the newly formed water mass to surrounding areas (Marshall & Schott, 1999). The final two stages are not necessarily separate from one another (Marshall & Schott, 1999). Overall, convection involves a wide variety of length and time scales, from millimeters to hundreds of kilometers and from seconds to months (Jones & Marshall, 1997; Marshall & Schott, 1999).

Preconditioning

The preconditioning phase sets the properties of the water column to those conducive to vertical mixing. To do so, several tasks must be accomplished.

First, the top several hundred meters of water must have their temperature lowered and/or salinity raised such that the density stratification of the column is reduced – put another way, the squared buoyancy frequency $N^2 = -\frac{g}{\rho_o}\frac{d\overline{\rho}}{dz}$ (where g is the Earth's gravitational constant, $\overline{\rho}$ is background density, and ρ_o is a reference density) is set to a smaller, yet still positive, value. The cooling required for this may be accomplished in several ways, but usually involves cool air temperatures (negative sensible heat flux) and surface winds (negative latent heat flux). Further salinity increases may be achieved through brine rejection from sea ice.

The second task to be accomplished is the raising, or "doming", of the pycnocline to a shallower depth. Convection and mixing to a certain depth will therefore reach a higher density surface than they otherwise would, allowing the formation of even denser water. This effect is usually a consequence of the overall densification of the water column.

This preconditioning phase occurs over quite large geographical areas. However, deep convection occurs only in those areas most extremely affected – generally the interiors of gyres or the edges of sea ice – and over patches mere tens of kilometers in diameter. Timescales vary due to a host of factors, but it is probably safe to say that the preconditioning phase lasts from mid-fall to mid-winter.

The Convective Event

The convective event is generally triggered by the arrival of the low pressure systems associated with winter and their accompanying strong, cold, dry winds (Marshall & Schott, 1999). The surface heat losses associated with these winds act to make the water column unstable – that is, $N^2 \leq 0$. Once this is achieved, convection ensues within the existing preconditioned patches.

However, convection does *not* occur over the entire patch at once, nor does it occur according to the classic, convection-current driven picture. Instead, it occurs within horizontally localized areas something less than 1 km in diameter, and does so within narrow chimneys where particles engage in small-scale turbulent mixing over a depth of several thousand meters (Marshall & Schott, 1999; Yashayaev & Loder, 2009; Khatiwala et al., 2002). The events usually last only a day or two before the water column in the convective region becomes well-mixed (Schott et al., 1993).

Perhaps counterintuitively, there need not be a large density differential over the water column for mixing to be quite vigorous. This is shown by the following idealized buoyancy scaling argument for a fluid parcel from (Marshall & Schott, 1999).

Let buoyancy b be defined as

$$b = -\frac{\rho - \rho_{amb}}{\rho_o} g, \tag{1.2.1}$$

where g is the usual gravitational constant, ρ is the local density of a fluid parcel, ρ_{amb} is the density of the fluid surrounding said parcel, and ρ_o is some reference density, usually taken to be 1000 kg/m^3. Then, if one assumes that (ideal) convection reverses the relative positions of two fluid parcels with buoyancies b_1 and b_2 separated by a vertical distance Δz, the resulting potential energy change of the system is

$$\Delta U_{PE} = \rho_o \Delta b \Delta z, \quad \Delta b = b_1 - b_2,$$

assuming Δz is positive and parcel 1 lies above parcel 2. Neglecting losses to viscosity and other processes, this may be set equal to the induced kinetic energy by energy conservation. Assuming horizontal velocities are of the same scale as the vertical w velocity gives

$$\Delta U_{PE} = |\rho_o \Delta b \Delta z| = 2\left[3\left(\frac{1}{2}\rho_o w^2\right)\right] = U_{KE}$$
$$\Rightarrow w^2 = \frac{1}{3}|\Delta b \Delta z|$$

The "3" in the first equation above is present because there are three spatial dimensions gaining energy; the "2" is present because there are two parcels gaining energy. The buoyancy *flux* is therefore defined to be

$$\mathcal{B} \equiv w\Delta b = (\Delta z/3)^{\frac{1}{2}} (\Delta b)^{\frac{3}{2}} \tag{1.2.2}$$

Since the overturning was triggered by heat loss, it is probably safe to assume that the buoyancy difference between the two parcels is due to a temperature difference rather than salinity or pressure effects. If this temperature difference is small, density can be approximated by a linear equation,

$$\rho \approx \rho_o [1 - \alpha(\theta - \theta_o)], \quad \alpha \approx 0.3 - 0.7 \times 10^{-4}\,\mathrm{K}^{-1} \text{ (greater at depth)} \tag{1.2.3}$$

$$\theta_o \approx -1.2 \text{ to } -1.4^\circ\,\mathrm{C} \text{ (warmer at depth)}^4$$

Here, θ and θ_o represent the actual and reference potential temperatures. Combining equations 1.2.1, 1.2.2, and 1.2.3, the potential temperature difference between two particles may be solved for:

$$(\theta_1 - \theta_2) = \frac{1}{\alpha g}\left[\frac{3\mathcal{B}^2}{\Delta z}\right]^{\frac{1}{3}}. \tag{1.2.4}$$

Taking typical values from Marshall & Schott (1999) for the wintertime Greenland Sea of $\Delta z = 800\,\mathrm{m}$, $\alpha = 0.5 \times 10^{-4}\,\mathrm{K}^{-1}$, $g = 10\,\mathrm{m/s}^2$, and $\mathcal{B} = 6.0 \times 10^{-8}\,\mathrm{m}^2/\mathrm{s}^3$ for the Greenland Sea, one finds a temperature difference $(\theta_1 - \theta_2) \approx 5 \times 10^{-3}\,^\circ\mathrm{C}$ and a vertical velocity of $w \approx 2.5\,\mathrm{cm/s}$. Therefore, a very small potential temperature inversion can lead to quite vigourous overturning!

[4] values are for the Greenland Sea, quoted in Marshall & Schott (1999)

Dispersal

After the deep convection event has occurred, the new water mass it produced must somehow be transported out of the area and stable stratification restored. Which mechanisms control this process are still under research; however, it is generally agreed (Jones & Marshall, 1997; Straneo, 2006) that one key mechanism is baroclinic instability. Horizontal density gradients (high density within the remnants of the convective chimney; low density outside it) are of such magnitude near the surface that baroclinic eddies are formed, serving chiefly to transport buoyant water from the boundary currents into the convective patch and essentially capping the chimney. They also advect some of the newly-formed dense water laterally. The majority of the dense export, however, is accomplished by gravity: the column of dense water simply collapses under its own weight and spreads out at its isopycnal level.

The timescales over which this occurs vary. Jones & Marshall (1997) argue that restratification occurs rather quickly, over the course of only a few days. The spreading of the deep water, however, may take much longer – according to Marshall & Schott (1999), perhaps weeks to months. However, since this spreading of this water could be seen as the genesis for many of the deep currents and overflows, the dispersal phase could be said to occur in perpetuity.

1.3 Nordic Seas Background

1.3.1 Geography

The Nordic Seas (NS; also referred to as the Greenland-Iceland-Norwegian (GIN) Seas) form one of the main conduits of water from one of the freshest regions on Earth (the Arctic), to one of the saltiest (the Atlantic) – the other is the Canadian Arctic Archipelago. In contrast to the relatively shallow (O(200 m), Mauritzen (1996a)), fractured Archipelago, however, the NS represent a relatively deep, direct route between the two. Together, the Canadian Arctic Archipelago and Nordic Seas export a total of around 7.7 Sv water from the Arctic, with the Nordic Seas accounting for 6.25 Sv of that number (Dickson et al., 2007), mostly thanks to the East Greenland Current. In addition, the NS is also a major source of North Atlantic Deep Water (Mauritzen, 1996a).

The Nordic region is shaped roughly like a diamond, its bounds defined by land masses and submarine ridges (see figure 1.2). Greenland marks its extreme western boundary, while the Greenland-Scotland Ridge, which marches from northwest to southeast between its two namesakes, forms the south-western boundary. From Scotland, the border runs north-east along the continental shelf of Europe, crossing the top of the North Sea and continuing up the coast of Norway. The final side of the diamond is completed by the Barents Shelf, with the northernmost point being marked by Fram Strait.

The GIN seas themselves are actually three in number. The Greenland Sea lies in the north, its maximum depth of ~ 3800 m separated from the Iceland Sea to its south-west by the Jan Mayen Ridge. The Iceland Sea is relatively shallow, with a maximum depth of around 2200 m, and is abutted

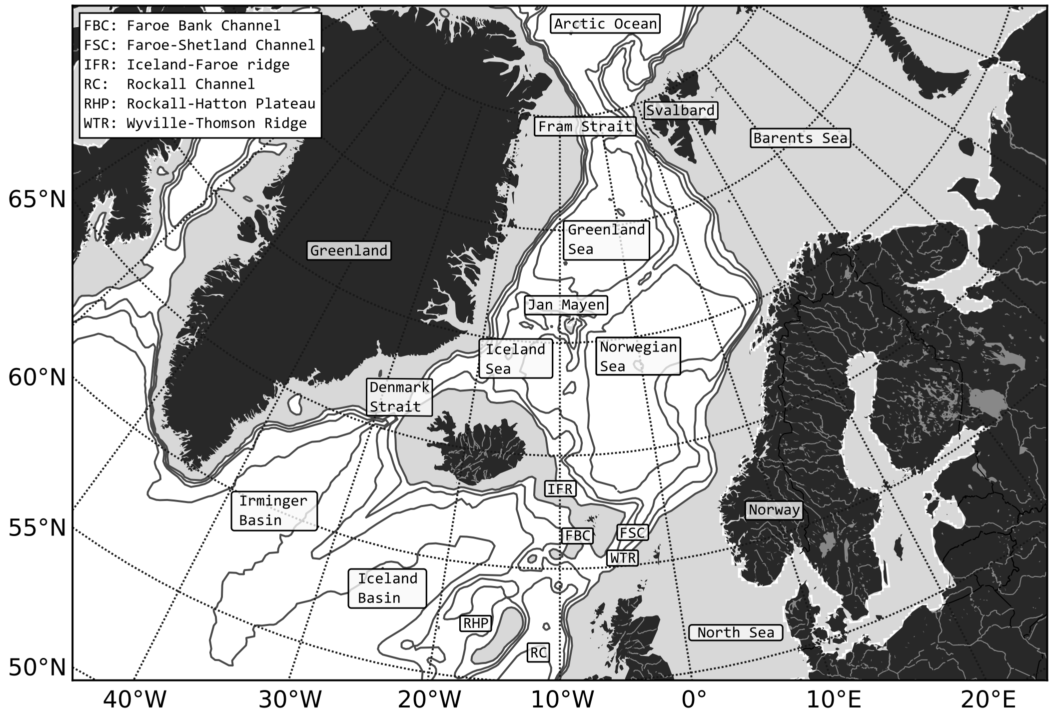

Figure 1.2: Geographic and bathymetric features of the Nordic Seas. See figure 1.3 for details of bathymetry along the Greenland-Scotland Ridge.

on its eastern side by the Norwegian Sea. The latter has two main basins: the deeper Norwegian Basin (3800 m) lies to the south, while the shallower Lofoten Basin (3400 m) is found to the north, adjacent the Greenland Sea's southeastern side (Aksenov et al., 2010)

The main entrances and exits for the NS are over the Iceland-Scotland Ridge, across the Barents Shelf, and through Fram Strait. The latter passage, named after Norwegian explorer Fridtjof Nansen's ship[5], is a rather deep passage with a maximum of 5607 meters at the Molloy Deep (Thiede et al., 1990). It represents the main export pathway from the Arctic for water following the Nordic (as opposed to Canadian Arctic Archipelago) route to the Atlantic – its average flux is around 6 Sv (Dickson et al., 2007).

[5]The *Fram*, specially constructed for polar exploration, was later used by Roald Amundsen for his successful 1910 assault on the South Pole

The Barents Shelf separates the Norwegian Sea from the Barents Sea, and has a mean depth of about 650 m (Smith & Sandwell, 1997). Around 2.2 Sv (Dickson et al., 2007) spills across it from the NS, much of which (1.5 ± 0.8 Sv) eventually recirculates back in through Fram Strait as Arctic Atlantic Water (Mauritzen, 1996b)[6].

Finally, the Greenland-Scotland Ridge forms a continuous submarine wall separating the Iceland and Norwegian Seas from the Atlantic. It is broken by three main passages. To the northwest is the Denmark Strait (DS), with a maximum sill depth of about 620 meters (Hansen & Østerhus, 2000). The DS is where the East Greenland Current exits the NS, exporting about 1.5 Sv in the upper layer (Dickson et al., 2007), with a further 3 Sv exiting in lower layers (Mauritzen, 1996b). Since the majority of this water is from the relatively fresh Arctic (essentially all of the East Greenland Current and, according to Mauritzen (1996b), 2 of the 3 Sv of deep overflow), the DS is a major fresh water export pathway. On the opposite side of Iceland lies the Iceland-Faroe Ridge (IFR), which contains a series of depressions deepening from 420 to 480 m as ones travels to the south (Hansen & Østerhus, 2000). Because of the shallow sill depth, there is not much export over this ridge (Hansen & Østerhus, 2000). Combined with the Faroe-Shetland Channel (FSC) to the southeast, however, there is a combined inflow of 7.0 Sv (Mauritzen, 1996b; Hansen & Østerhus, 2000) to 7.5 Sv (Dickson et al., 2007). The FSC, running between the Faroe Islands and Scotland, contains relatively complex bathymetry which

[6]Neither Dickson et al. (2007) nor Mauritzen (1996b) base their volume flux estimates fully on direct observations. In particular, Mauritzen (1996b) uses an inverse box model merely *initialized* with observational data (along with several estimates where no observations exist), while Dickson et al. (2007) rely on a combination of observations and climate model output

is dominated by the 840 m Faroe Bank Channel. This is the second major export pathway of Nordic overflow waters, exporting another 3 Sv (Hansen & Østerhus, 2000). On the southern side of the Faroe Bank is the much shallower (~ 400 m) Wyville-Thomson Ridge, which mainly concerns itself with Atlantic import (Hansen & Østerhus, 2000).

One last bathymetric feature that should be mentioned is the Reykjanes Ridge, a long tongue extending perhaps 750 km (Smith & Sandwell, 1997) to the south-west from Iceland. This ridge separates the north-east Atlantic into two basins: the Irminger Basin to the northwest, and the Iceland Basin to the southeast.

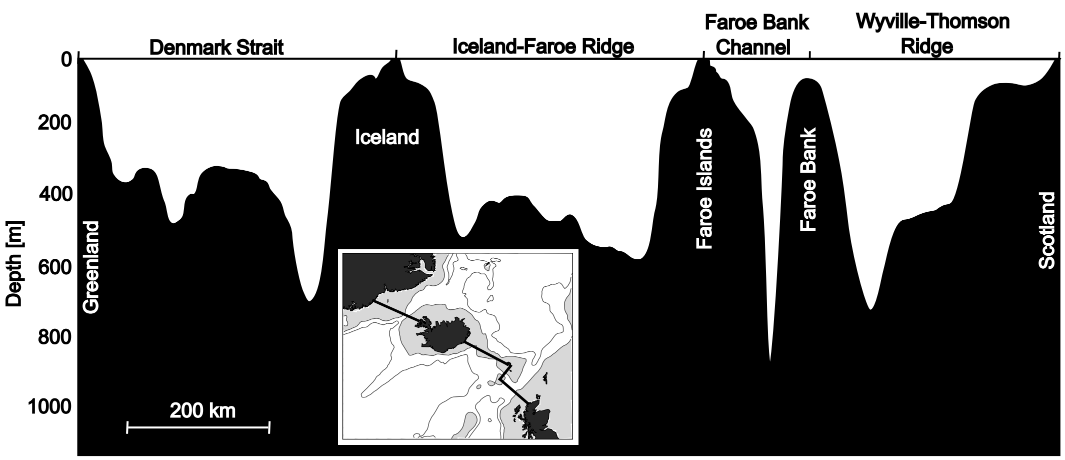

Figure 1.3: Cross-section of the Greenland-Scotland Ridge, using model bathymetry. Based on figure 2 of Hansen & Østerhus (2000).

1.3.2 Currents

To examine the complex layout of the Nordic Seas currents (shown in figures 1.4 and 1.5), I will use the terminology laid out in (Hansen & Østerhus, 2000), beginning with the origins of the North Atlantic Current. Unless otherwise noted, volume figures are those from the box model constructed by Mauritzen (1996b).

Surface Currents

When the Gulf Stream reaches the Northwest Corner off the coast of Newfoundland, part of it bends north-eastward toward Scotland. After crossing the Mid-Atlantic Ridge, it bifurcates at the Rockall-Hatton Plateau as seen in figure 1.4. The southern branch becomes the southbound Canary current, while the remaining 7 Sv or so (Dickson et al., 2007) flows on toward the Greenland-Scotland Ridge.

Hansen & Østerhus (2000) estimate that 3.7 Sv of the former current passes over the Wyville-Thomson Ridge, with another 3.3 Sv crossing over the IFR. The remainder continues around the Reykjanes Ridge as part of the Irminger Current. Over the course of this journey, the current cools noticeably and freshens slightly. After rounding the Ridge, 0.9±0.5 Sv breaks off and enters the Iceland Sea via the Denmark Strait (DS) by forming the North Icelandic Irminger Current. While part of this current recirculates around Iceland and back into the Atlantic (0.7±0.5), the rest follows the bathymetry on the northern side of the Greenland-Scotland Ridge and joins the water that flowed directly over the IFR or through the FSC to form the Norwegian Coastal Current.

Typical salinity and temperature values for inflow through the FSC are 35.3 and 7°C, respectively (Mauritzen, 1996b). The IFR inflow is similar, but the DS water is noticeably fresher and cooler at 35.1 and 4.5°C (Mauritzen, 1996b).

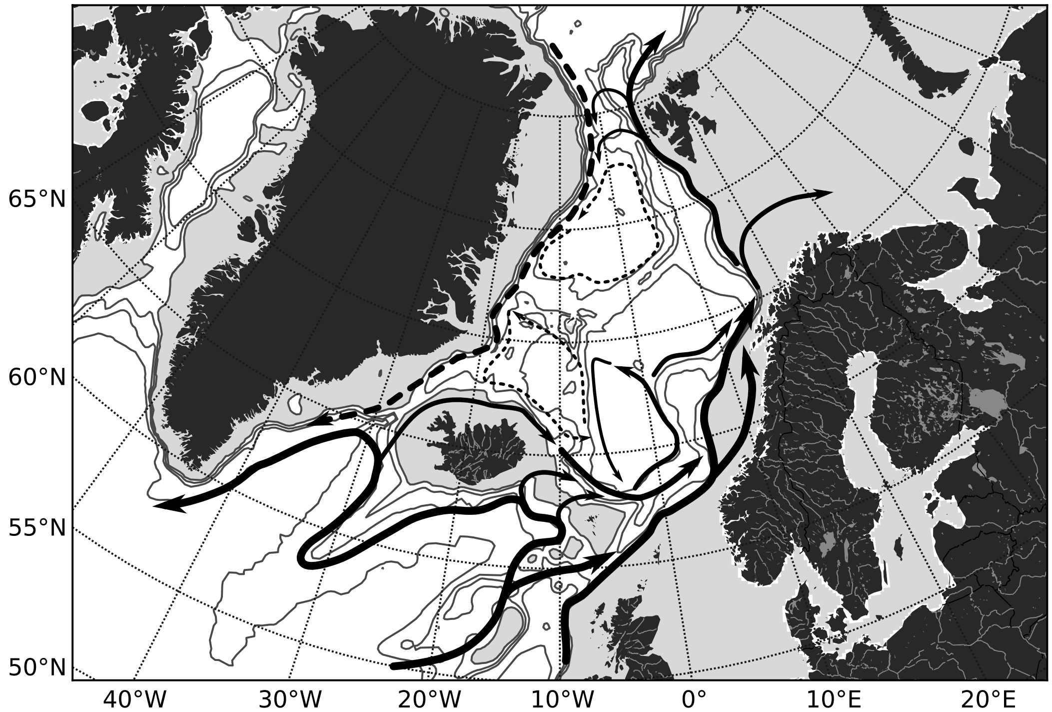

Figure 1.4: Surface currents in the North Atlantic and Nordic Seas. Solid arrows indicate the flow of Atlantic water; dashed and dotted lines show the paths of other water masses. See figure 1.3 for details of bathymetry along the Greenland-Scotland Ridge.

The offshore portion of the Norwegian Coastal Current breaks off and forms its own gyre in the southern portion of the Norwegian Sea, and is called the Recirculated Faroe Current. The majority continues up the western side of Norway relatively undisturbed. Upon reaching the northern coastline of Norway, part of the Norwegian Coastal Current splits off and flows over the sill into the Barents Sea (1.6±0.4 Sv, (Mauritzen, 1996b)), while the remainder continues on towards Svalbard and Fram Strait. At Fram Strait, the current breaks again; this time, most of it heads north into the Arctic regions (3.4±0.8 Sv), while the remainder (1.1±0.5 Sv) turns south again and follows the continental shelf of Greenland. Here, the flow picks up a major contribution of fresh water entering from the Arctic through the western side of Fram Strait

(2±0.7 Sv), and turns into the East Greenland Current.

When the East Greenland Current reaches the Jan Mayen Ridge, yet another division occurs. Part of the Current follows the Ridge eastward and forms a recirculation around the Greenland Sea while the rest, again, continues southward. Upon reaching the DS, the current splits a final time – most continues southward and retains the name East Greenland Current, while some splits off and joins the inflowing Atlantic waters in the North Icelandic Irminger Current.

Deep Currents

In contrast to the relatively well-established surface flow patterns, comparatively little is known about the paths taken by deep water in the NS (shown in figure 1.5). We do know that a significant portion of the overflows are of Arctic origin, having flowed in through Fram Strait, (Hansen & Østerhus, 2000; Mauritzen, 1996b). We also know that deep water is formed in all three basins, but especially the Iceland and Greenland Basins. It is likely that the water from the Greenland Basin joins the greater part of the Arctic inflow and travels to the FSC via the Norwegian Sea, while the remaining Arctic water joins the Iceland Sea water and flows out through the DS (Hansen & Østerhus, 2000).

1.3.3 Convection Areas & Mechanism

The mechanisms by which deep convection occurs in the GIN seas are not dissimilar from those in Antarctica, which *are* dissimilar from those in the

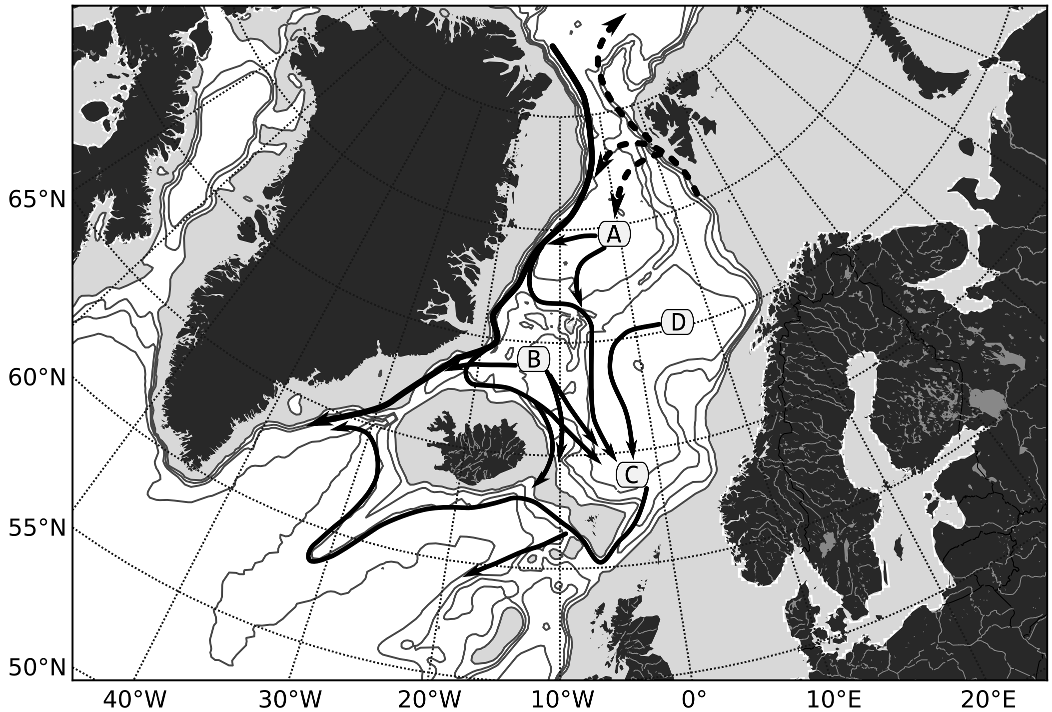

Figure 1.5: Deep current paths in the Nordic Seas region. Dashed line indicates a surface current feeding deep water formation. Locations A, B, C, and D are known deep water formation locations. See figure 1.3 for details of bathymetry along the Greenland-Scotland Ridge.

Labrador Sea and the Mediterranean. From the perspective of raw numbers, buoyancy fluxes are actually rather larger in the latter two when compared to the Nordic region. What allows the GIN seas to be remarkable is the preconditioning phase of convection. The Mediterranean, being very warm, requires high heat fluxes at the surface to destabilize the water column even with correspondingly high evaporation rates. Similarly, the Labrador Sea draws a significant portion of its water from the relatively warm Irminger Current, which means its convective heat fluxes must also be quite high. In the NS, however, even the warm North Atlantic Current-derived water has been significantly cooled and laden with salt by the time convection occurs. Therefore, it needs to lose comparatively little heat at its surface to mix quite deeply. Additionally, in some regions there is the effect of sea ice to consider.

Sea ice is transported down the east coast of Greenland from the Arctic and is recirculated in late fall by the Jan Mayen current to form the Is Oden (Norwegian, "Ice Point"). Beneath it, brine rejection from ice formation and surface cooling from freezing both serve to further densify the upper mixed layer of the ocean. Meanwhile, north of the Is Oden, the Nord Bukta (Norwegian, "North Bay") forms, an ice-free region kept that way by the warm(er) water of the Norwegian Atlantic Current. Here, the characteristic cold, dry winds of a deep convection zone finish the job of creating vertical density instabilities to trigger convective events. Because of the conditioned low-temperature and high-salinity nature of the water, the end product is very dense, and sinks to the bottom of the basin. As mentioned, deep convection also occurs in other areas of the NS, but not quite so dramatically.

Dispersion occurs largely through the baroclinic eddies discussed earlier, while simple overflowing of dense water from the basin also contributes. The latter process may be visualized by imagining the NS filled with a two-layer fluid, light over heavy. Ignoring the effect of in- and outflowing currents for the moment, and switching off convection, it is easily seen that at some point an equilibrium state may be reached – dense fluid fills the bottom of the basin up to the level of the lowest sill depth, above which the lighter fluid exists to the sea surface. If we then switch on deep convection, some of the lighter fluid will be converted into heavier fluid. When this occurs, the newly formed mass will be distributed laterally by baroclinic eddies, but will also tend to sink into the existing lower layer and increase its volume. Thus, the height of the lower layer will increase *above* the lowest sill height, creating a hydraulic head which pushes the denser liquid over the Greenland-Scotland Ridge and into the Atlantic. Also, because in practice NS deep water is heavier than Atlantic water on the south side of the Greenland-Scotland Ridge (figure 5 of (Hansen & Østerhus, 2000) shows a good illustration of the front between the two), this overflow will tend to rush turbulently downhill, thus entraining even more water in its wake.

1.4 Thesis Outline

Within this study, I will be addressing two main questions:

1. What pathways are taken within the Nordic Seas by that part of the inflowing North Atlantic Current water which joins the deep overflows across the Greenland-Scotland Ridge?

2. How much of the inflowing North Atlantic Current water is transformed *within the Nordic Seas* into mid-depth water, which subsequently exits over the Greenland-Scotland Ridge?

To answer these questions, I first discuss general circulation model theory, then outline the specifics of the ORCA025-KAB001 configuration which I use (section 2.1). I explore Lagrangian particle tracking theory in section 2.2. I then validate the ocean model in section 3.1, and set up my particle tracking experiments in section 3.2.

Section 3.3.1 validates the Lagrangian experiments, while the remainder of chapter 3 develops their results. I shall answer question (1) in the first part of section 3.3.2 by plotting the paths, both seasonally and decadally, of only those particles which exit across the Greenland-Scotland Ridge below 200 m.

This gives insight into the flow characteristics and transformation processes of these deep particles. Question (2) is answered in the second part of the same section by comparing the number of Atlantic-bound Lagrangian particles to the total number which flowed into the Nordic Seas.

Finally, I show in section 3.3.3 that this outflowing North Atlantic Current-derived water is not actually part of the deep flow, but is instead a mid-depth water mass. This is partly due to the transformations it experiences (relatively small heat losses in particular), and partly due to the model's poor representation of vertical mixing. Results are summarized in chapter 4.

Chapter 2

The Models

2.1 Ocean Model

2.1.1 Introduction

The NEMO (Nucleus for European Modelling of the Ocean) project is a global effort that is the basis for a variety of ocean and climate modelling programs. NEMO itself is a collection of engines related to ocean modelling, including the OPA (Océan PArallélisé) ocean dynamics and thermodynamics module, the LIM (Louvain la-neuve Ice Model) series of ocean/sea ice interaction models, and a variety of other components relating to chemical and biological tracers, nested-grid communication schemes, and data assimilation techniques (Madec, 2008).

One major program that uses NEMO as its basis is the French DRAKKAR project. Within the context of this project, a series of NEMO configurations were built using the ORCA025 one-quarter degree global mesh. These configurations were created with two main purposes in mind: first, to create a four-dimensional record of the global ocean for the period from 1958 to 2004;

second, to use this record in the forcing schemes of higher-resolution, basin-scale models (DRAKKAR Group, 2010).

The ORCA025-KAB001 configuration (hereafter referred to as just KAB001) was selected for this study for several reasons. First, the data set it produces has existed for several years and has been reasonably well-validated by other studies in the Mediterranean Sea (Tsimplis et al., 2008; Lazure et al., 2009) and the South Pacific (Koch-Larrouy et al., 2007; Feng et al., 2008). Second, thanks to its relatively high quarter-degree resolution, the configuration is able to resolve many of the mesoscale eddies which are important for heat and salt exchange, and therefore deep water formation, in the Nordic region (the typical Rossby radius in the Nordic region is about 7 km (Chelton et al., 1998), compared to about 14 km between model grid points, so smaller eddies will not be well-represented. However, those 50 km or larger in diameter will be). Finally, and not least importantly, the data was readily available.

The ocean component used by the version of NEMO in use (Version 3.1) is based on release 9.1 of the OPA model. OPA is responsible for the motion and properties of the seawater itself – that is, its momentum, temperature, and salinity. Separate modules are used for calculating tracers such as carbon dioxide and oxygen-18; however, the equations for these may be written down along with the seawater equations. I begin by outlining the primitive equations used for both seawater and tracers, then discuss the boundary conditions, meshes, parameterizations, and forcing schemes used by the KAB001 configuration.

2.1.2 Assumptions

Nearly all geophysical fluid models are based on discretized differential equations derived from the Navier-Stokes relations, and OPA is no exception. Usually the fluids involved are assumed to be stratified in density, and exist in a coordinate system rotating relative to the stars. In addition to these, the OPA component of NEMO makes a few further assumptions (Madec, 2008):

1. **spherical Earth approximation:** gravitational equipotential surfaces are assumed to be spherical, instead of being based on the actual shape of the geoid. Thus, at any point on the Earth, gravity points in the downward direction.

2. **thin-shell approximation:** the total depth of the ocean h is said to be small in comparison to the radius of the Earth R. Thus, for example, quantities involving the length $R + h$ can be approximated by just R.

3. **Boussinesq hypothesis:** with the exception of their contribution to bouyancy forces, density variations are neglected.

4. **incompressibility hypothesis:** a volume of fluid is assumed to maintain a constant volume; therefore, the three-dimensional divergence of the velocity field is set to zero

5. **hydrostatic hypothesis:** vertical momentum conservation is reduced to the hydrostatic equation. As a result, vertical convective processes vanish from the Navier-Stokes equations and must be parameterized instead.

6. **turbulent closure hypothesis:** it is assumed that small-scale processes which affect the large-scale are able to be parameterized in terms of large-scale features.

These assumptions are listed roughly according to their robustness, from most to least. The spherical Earth approximation is really quite good – Tapley et al. (2005)'s data shows a variation in the geoid, relative to the mean sea level of a reference ellipsoid[1], of ±100 m (see figure 2.1). This is compared to the Earth's nominal radius of about 6371 km (Lide, 2000). The thin-shell approximation is also excellent – the average depth of the world ocean, 3.795 kilometers (Encyclopædia Britannica, 2010), is only about 0.060% of the 6371 km radius (Lide, 2000), which is certainly very small.

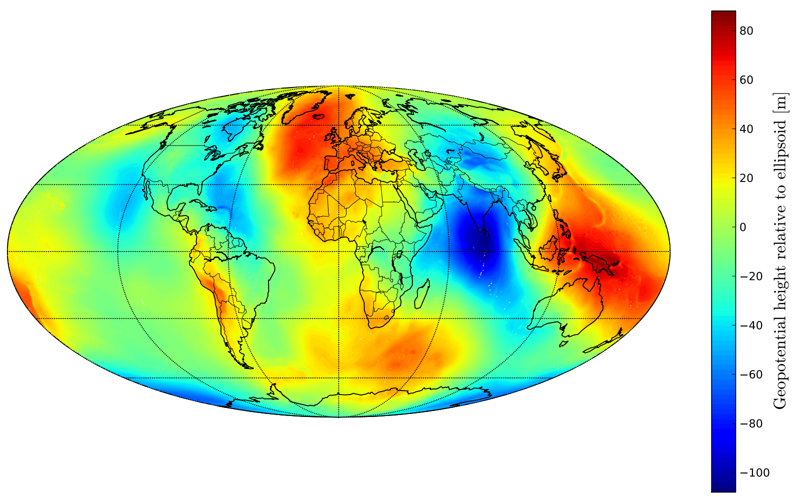

Figure 2.1: Variation in geoid height relative to the mean sea level of a reference ellipsoid for the GGM02 geoid model based on data from the GRACE satellites (Tapley et al., 2005)

The Boussinesq approximation is said to be valid if the vertical length scale L of the system in question is $\ll c^2/g$, where c is the speed of sound in the fluid and g is the gravitational field strength (Kundu & Cohen, 2008). Taking L to be 3795 m as before, c in seawater ($T = 4$°C, $S = 35$, depth= 1000m) to be 1468 m/s (Wong & Zhu, 1995), and g to be 9.8 m/s^2 (Halliday et al., 2001), $c^2/g \approx 219,900 \gg 3795$. Therefore, the Boussinesq approximation is

[1] $A_e = 6378136.3\,\mathrm{m}$, $1/f = 298.257$, (GMM02 Group, 2004)

valid for the ocean.

The incompressibility hypothesis is still fairly good, but slightly weaker. In the depths of the ocean water does get compressed by pressure to a non-trivial degree, but these compressibility effects occur over long enough length and time scales that they can be effectively ignored in the primitive equations. For example, an extreme vertical velocity is on the order of 3-6 cm/s (Marshall & Schott, 1999), which only occurs during deep convection. More usually, vertical velocities are something less than 1 cm/s. Assuming a parcel of water is transported at the (rather extreme) 6 cm/s, it will take 23 hours to descend 5000 m. Near the surface, a kilogram of seawater displaces about 970 cm^3 (Fofonoff & Millard Jr., 1983). At 5000 m, that same kilogram of water displaces only 950 cm^3 (Fofonoff & Millard Jr., 1983), or about 2% less. Therefore, even in the event of strong, sustained (and likely unrealistic) deep convection, the water still only changes its density by 2% over the course of a day due to pressure effects.

Much less certain is the hydrostatic assumption. It is valid as long as the horizontal velocity scale is much larger than the vertical velocity scale (Kundu & Cohen, 2008). Generally this is the case – a typical boundary current may have a horizontal core velocity of 30 cm/s, but essentially no vertical speed. In the case of vigorous mixing or deep convection, however, the situation is different – such events often occur near the centres of gyres, away from boundary currents, where horizontal speeds thus *may* approach those in the vertical. In such a situation, the hydrostatic equation rapidly loses its fidelity. As stated, though, generally flows are more horizontal than vertical, and so generally the approximation is valid.

The turbulent closure hypothesis is the weakest assumption made. To be reliable, it requires that good parameterizations of the small-scale processes be made and that all such processes are considered – both of these requirements are difficult to meet, given the vast geographical area covered, the different length, velocity, and time scales involved, and the inherent complication of real-world physical processes. This is still an active area of research with much work remaining to be done, but modern parameterizations for such things as lateral diffusion and eddy-induced mixing are really quite good in the general case (Deacu & Myers, 2005; Smith & Gent, 2004).

2.1.3 Primitive Equations

The equations of motion for a fluid under these assumptions are developed in many sources; for one example, refer to Chaper 4 of Kundu & Cohen (2008). The NEMO model implements these equations in spherical coordinates. However, this adds complication to their derivation without necessarily adding physical insight, so for simplicity I will follow Kundu's example and derive them in Cartesian coordinates. Written thus, the primitive equations for a fluid are:

$$\begin{aligned} \frac{D\mathbf{u}}{Dt} + f\hat{\mathbf{k}} \times \mathbf{u} &= -\frac{1}{\rho_o}\vec{\nabla}p - \frac{g\rho}{\rho_o}\hat{\mathbf{k}} + \mathbf{A}, \qquad (2.1.1) \\ \frac{D\rho}{Dt} &= 0 \\ \vec{\nabla} \cdot \mathbf{u} &= 0 \end{aligned}$$

along with an equation of state. The meanings of the variables used are shown in Table 2.1. The first equation states conservation of momentum. The sec-

Symbol	Meaning
$\vec{\nabla}$	gradient operator
$\vec{\nabla}_h$	horizontal gradient operator; $(\hat{\imath}, \hat{\jmath})$ components only
$\mathbf{u}$	3-dimensional velocity field
$\mathbf{u}_h$	$u\hat{\imath} + v\hat{\jmath}$ only, for $\mathbf{U} = (u, v, w)$
t	time
z	vertical coordinate
ρ	total density
ρ_o	reference density
p	total pressure
f	coriolis parameter for point on Earth, $2\mathbf{\Omega} \cdot \hat{\mathbf{k}}$
$\mathbf{\Omega}$	angular velocity vector of Earth
$\hat{\mathbf{k}}$	vertical unit vector
g	scalar gravitational acceleration
$\mathbf{A}$	friction force per unit mass
$\mathbf{A}_h$	friction force per unit mass, horizontal directions
T, S	temperature, salinity
$\mathbf{D}^{\mathbf{u}}$	small-scale momentum parameterization
D^T	small-scale temperature parameterization
D^S	small-scale salinity parameterization
$\mathbf{F}^{\mathbf{U}}$	momentum surface forcing term
F^T	temperature surface forcing term
F^S	salinity surface forcing term

Table 2.1: Definitions for variables used in equations

ond specifies the conservation of internal energy, while the third is a statement of mass conservation for an incompressible fluid. Note that here the internal energy change is said to equal zero; in reality (and in the equations used by the model), it actually equals a small term which allows for diffusion.

The material derivative in the momentum equation may be written as follows:

$$\begin{aligned}\frac{D\mathbf{u}}{Dt} &= \frac{D}{Dt}\left(u_i\hat{x}_i\right) = \frac{\partial}{\partial t}\left(u_i\hat{x}_i\right) + \mathbf{u}\cdot\vec{\nabla}\left(u_i\hat{x}_i\right)\\ &= \frac{\partial\mathbf{u}}{\partial t} + \left[\mathbf{u}\cdot\vec{\nabla}\left(\mathbf{u}\right)\right]\end{aligned}$$

Using the vector identity $\vec{\nabla}(\mathbf{a}\cdot\mathbf{b}) = (\mathbf{a}\cdot\vec{\nabla})\mathbf{b} + (\mathbf{b}\cdot\vec{\nabla})\mathbf{a} - (\vec{\nabla}\times\mathbf{b})\times\mathbf{a} - (\vec{\nabla}\times\mathbf{a})\times\mathbf{b}$, it may then be rewritten as:

$$\frac{D\mathbf{u}}{Dt} = \frac{\partial\mathbf{u}}{\partial t} + \left[(\vec{\nabla}\times\mathbf{u})\times\mathbf{u} + \frac{1}{2}\vec{\nabla}(\mathbf{u}\cdot\mathbf{u})\right]$$

Combining the momentum equation of (2.1.1) with equation (2.1.3), the horizontal components (ie. zonal and meridional, denoted by a subscript "h") of the momentum equation may be found:

$$\frac{\partial\mathbf{u}_h}{\partial t} = -\left[\left(\vec{\nabla}\times\mathbf{u}\right)\times\mathbf{u} + \frac{1}{2}\vec{\nabla}\left(\mathbf{u}\cdot\mathbf{u}\right)\right]_h - 2\mathbf{\Omega}\times\mathbf{u} - \frac{1}{\rho_o}\vec{\nabla}_h p + \mathbf{A}_h \qquad (2.1.2)$$

By assumption, the vertical component of momentum conservation reduces to the hydrostatic approximation:

$$\frac{\partial p}{\partial z} = -\rho g \qquad (2.1.3)$$

Note that there is no explicit vertical velocity in equation 2.1.3; this will be important when we discuss the Ariane system in section 2.2.

The equations for the property tracers (heat and salinity) are very similar to one another. The time evolution of an ideal tracer's scalar concentration Q can be expressed as a sum of three terms: the advection of that tracer to or from a particular area; the effect of small-scale physics on that tracer; and forcing of the tracer through the boundaries of the domain. This is outlined by equation 2.1.4:

$$\underbrace{\left(\frac{\partial Q}{\partial t}\right)}_{\text{time evolution}} = -\underbrace{\left(\nabla\cdot(Q\mathbf{u})\right)}_{\text{advection}} + \underbrace{\left(D^Q\right)}_{\text{small-scale physics}} + \underbrace{\left(F^Q\right)}_{\text{surface forcing}} \qquad (2.1.4)$$

Now, if I split the frictional ($\mathbf{A}_h$) term of equation 2.1.2 in two – one for small-scale processes and one for interactions with the domain boundary – and write a version of equation 2.1.4 for both temperature and salinity, I can finally write down the primitive equations quoted in the OPA manual ((Madec, 2008)). Together with an equation of state relating density to temperature, salinity, and pressure, these are:

$$\frac{\partial \mathbf{u}_h}{\partial t} = -\left[\left(\vec{\nabla} \times \mathbf{u}\right) \times \mathbf{u} + \frac{1}{2}\vec{\nabla}\left(\mathbf{u} \cdot \mathbf{u}\right)\right]_h - f\hat{\mathbf{k}} \times \mathbf{u}_h - \frac{1}{\rho_o}\vec{\nabla}_h\left(p\right) + \mathbf{D}^{\mathbf{u}} + \mathbf{F}^{\mathbf{u}} \tag{2.1.5}$$

$$\frac{\partial p}{\partial z} = -\rho g$$

$$\vec{\nabla} \cdot \mathbf{u} = 0$$

$$\frac{\partial T}{\partial t} = -\vec{\nabla} \cdot \left(T\mathbf{u}\right) + D^T + F^T$$

$$\frac{\partial S}{\partial t} = -\vec{\nabla} \cdot \left(S\mathbf{u}\right) + D^S + F^S$$

$$\rho = \rho\left(T, S, p\right)$$

In order of appearance, equations (2.1.5) are: (1) momentum balance in the horizontal; (2) the hydrostatic assumption in the vertical; (3) the nondivergence, or incompressibility, condition; (4) the tracer equation for temperature; (5) the tracer equation for salinity; and (6) the equation of state for seawater (in practice, the one proposed in (Jackett & McDougall, 1995) is used by OPA) (Madec, 2008).

The various terms involving D's in the tracer and horizontal momentum conservation equations represent the parameterizations chosen to close the problem to small-scale processes, as required by assumption #6, while the F-terms represent surface forcing. Note that there are vector and scalar versions for both. The vector forms relate to velocity – one value in each of the u-, v-, and w-directions (the u and v parameterizations are often, even usually, identical to one another). The scalar expressions relate to the two tracer equations – since both of those equations describe scalar quantities, one needs only a scalar parameterization for their closures.

In the case of the F-series of parameterizations, it's important to recognize that *surface* does not necessarily mean *air-sea* (or air-ice) *boundary*. In fact, it means any interface between water and some other material. This means there are two surfaces to consider: the aforementioned air-sea (or air-ice) boundary, and the sea floor itself. Ordinarily, both heat and salt fluxes between the sea floor and the open ocean are so minimal (over shorter, order-century, timescales) as to be ignored, even in such heat- and nutrient (ie. salt)-rich environments as undersea vents and volcanoes[2]. On the other hand, coastal regions can contribute to both heat and salt balances through river runoff, while sea ice changes the twain during both formation (brine rejection increases local salinity) and melting (meltwater decreases local salinity). Of course, precipitation and evaporation are also major contributors to the $\mathbf{F}$ -terms.

In addition to the tracers, the $\mathbf{F}$ terms for momentum need to be taken into account. Because of friction, there is momentum transfer between seawater and the ocean boundaries. On the sea floor this transfer tends to retard motion, while at the sea surface wind stresses are a major driver of oceanic surface currents. Both the small-scale and boundary forcing parameterizations

[2]Actually, authors such as Emile-Geay & Madec (2008) suggest such areas increase temperatures by up to half a degree in the abyss, and may increase the volume fluxes of deep waters. However, such ideas have not yet been incorporated into most models.

will be examined in more detail in sections 2.1.6 and 2.1.7.

2.1.4 Grid

Using a grid system where variables are staggered spatially with respect to one another tends to have significant advantages over one where all variables exist at the same spatial point. One of these advantages is a much more accurate representation of waves. For example, when equations for gravity or Rossby waves are solved numerically, errors in frequency and group velocity tend to be of smaller magnitude than when using an unstaggered grid (Haidvogel & Beckmann, 1999). In addition, staggered grids tend to be much more stable numerically than unstaggered grids (Arakawa, 1966).

With this in mind, the OPA model discretizes its equations on a three-dimensional, staggered Arakawa C-grid (Madec, 2008). This particular grid variant reproduces gravity waves more accurately at mid-latitudes than many other alternatives, while maintaining acceptable accuracy at higher latitudes (assuming the grid's spatial resolution is relatively high) (Haidvogel & Beckmann, 1999). In fact, OPA implements this scheme by using five separate meshes: one for tracers, one for each of the u-, v-, and w-velocities, and one for the Coriolis parameter f. Values from each of these meshes are linearly interpolated onto the others for calculation purposes.

At the centre of each grid cell are the tracer points – points that relate to salinity, temperature, and other chemical or biological quantities. In the centre of both zonal faces of the cell are u-velocity points, with v-velocity points configured in a similar fashion on both meridional faces. There are four

Coriolis parameter points on each cell, one in each of the four vertical edges at the same depth as the tracer points. Finally, there are two w-velocity points horizontally aligned with the tracer point and embedded the top and bottom faces. This configuration is illustrated graphically in figure 2.2.

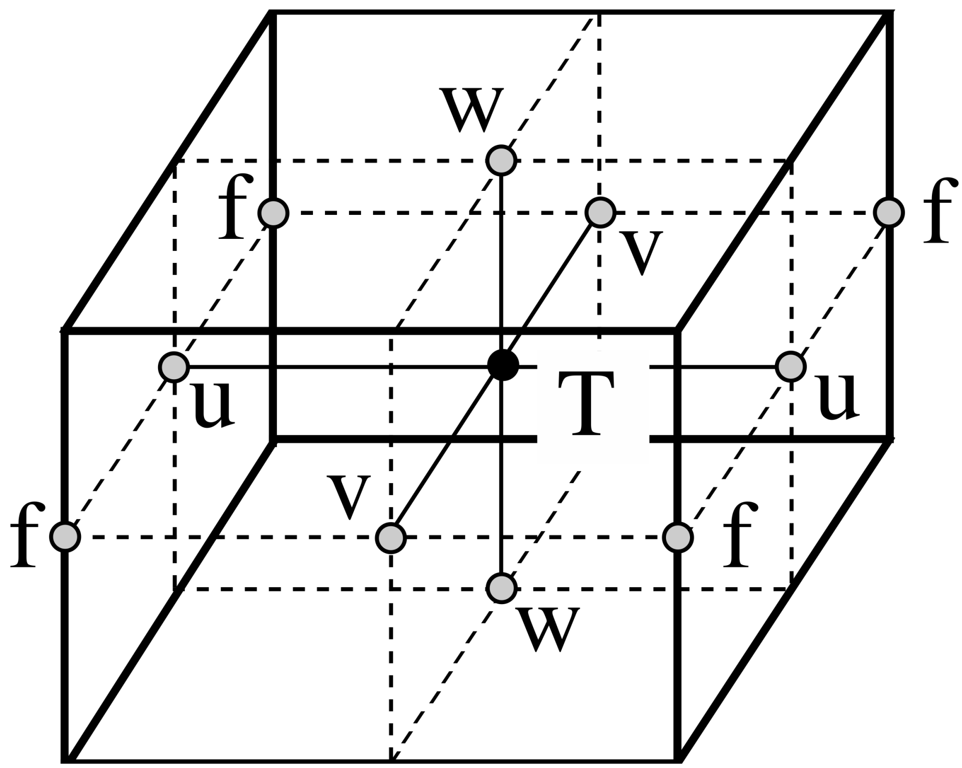

Figure 2.2: Arrangement of variables in a three-dimensional Arakawa C-grid. T indicates a tracer point, u the zonal velocity, v the meridional velocity, w the vertical velocity, and f the Coriolis parameter. The x- (zonal) direction is toward the right; the z- (upward) direction is toward the top of the page. *Source: NEMO Ocean Engine (Madec, 2008)*

The tracer mesh is the first to be created when configuring the model. To do so, one begins by determining the geographical (horizontal) locations of the points. In the case of the ORCA025 mesh, the desired nominal resolution is one-quarter of a degree. This means that, at the equator, cell spacing is 27.75 km. As one travels further from the equator, however, the closer together lines of longitude become, and therefore the smaller the separation of the grid cells[3]. In general, cell spacing at a particular latitude θ is nominally $S = S_o \cos(\theta)$, where S_o is the spacing at the equator. However, ORCA025 uses a tripolar arrangement, placing poles (in particular the North pole) over land to avoid dealing with various unpleasant numerical issues associated with the polar topological singularity (Roberts et al., 2006). Combined with the variation in spacing with latitude, this means that the distance between grid points in the Arctic Ocean is about 10 km; in the Weddell Sea, 7 km; and at 60°N, 14 km.

Once these lateral positions have been determined, the depth coordinates must be computed. In the case of ORCA025 there are forty-six of these depth levels, which are defined using the continuous function shown in equation 2.1.6 (Madec, 2008). Here, z_o is the depth in meters, k is the depth index of the point in question (increasing with depth), and the constants are given in Table 2.2. This function ensures that the levels are concentrated near the surface (in order to capture interesting dynamics such as mixed-layer depths, thermal fluxes, precipitation/evaporation, and so on) while being more separated at depth (where the ocean tends to be more quiescent and less stratified).

$$z_o(k) = h_{sur} - h_o k - h_1 \ln \left[\cosh \left(\frac{k - h_{th}}{h_{cr}} \right) \right], \tag{2.1.6}$$

The depths thus calculated are the same for all horizontal grid points – that is, for a point (i, j) in the horizontal grid, the depth $z(k) = \text{constant} \ \forall \ (i, j)$. However, not all vertical levels are necessarily used by every horizontal point. In fact, none of the horizontal points in practice use all forty-six available depth levels. Instead, the maximum depth in a given column is determined from the

[3]In both the zonal and meridional directions. Because the horizontal grid is isotropic, changing one horizontal dimension also changes the other

Constant	Value
h_{sur}	-2143.959 m
h_o	127.4511 m
h_1	123.0758 m
h_{th}	23.5630
h_{cr}	9.0000

Table 2.2: Values for constants in equation 2.1.6 (from (Molines et al., 2006))

known bathymetry of the world ocean, as determined from a combination of sources including the etopo2 2-minute resolution file produced by the National Geophysical Data Center, the Smith and Sandwell Version 8.2 satellite-derived bathymetry, IBCAO (International Bathymetric Chart of the Atlantic Ocean) data in the Arctic, and various sources for Antarctic regions (Molines et al., 2004). If the depth of the ocean floor at a horizontal point (i, j) is determined to be H, then only the first $k \in \left\{0...N \mid z(k) + \frac{1}{2}e_3(k) < H\right\}$ depth levels will be defined (where the scale factor e_3 is defined in equations 2.1.7), with the remaining levels being ignored. The ORCA025 configuration also makes use of partial step topography. If the depth H lies within a model cell, that cell may be defined, but only for a depth of $H - \left(z - \frac{1}{2}e_3\right)$, thus "partially filling" that cell with seawater. The end result of this bathymetry creation process is shown in Figure 2.3.

It should be noted that, in addition to the above-named bathymetric data sources, some hand-editing of mesh points was also performed. Most notable for this study is the doubling in width of the Denmark Strait and the digging of a deeper channel on its Atlantic side in an effort to improve the downstream properties of water leaving the Nordic Seas (Molines et al., 2006). The effect of this editing on my study will hopefully be small; to quote the ORCA team, "we note that in a short experiment with NATL4[4], the effect of widening the

[4] a regional version of ORCA025

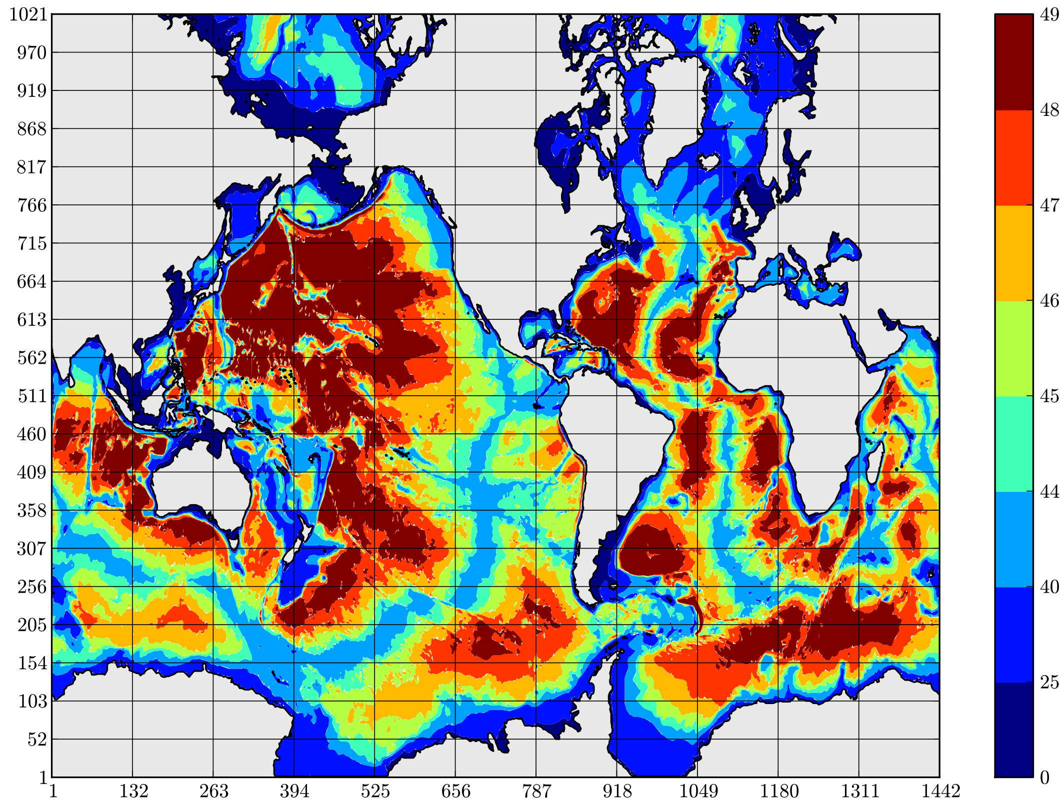

Figure 2.3: Bathymetry of the world ocean in model grid coordinates for a NEMO configuration similar to KAB001. Both use the ORCA025 horizontal grid; however, the configuration shown here uses 49 depth levels instead of KAB001's 46. *Based on Drakkar ORCA025 experiments ((Molines et al., 2004)), but using the GLORYS1V1 global mesh.*

Denmark Strait by a factor of two did not lead to an increase of the overall transport because the velocities became smaller in the same proportion as the increase in area". Despite no net change in net transport, "the properties of the waters downstream [on the Atlantic side] improved somewhat, and the overturning increased by at least one Sverdrup". That said, as will be discussed in Section 2.1.6, the entrainment of water by overturning processes is still poorly parameterized.

With both the horizontal and vertical positions of the T-grid (tracer grid) set, the grids for the other variables may be developed. The spatial positions of the u- and v- grids are interpolated from the T-grid in the zonal and meridional directions, respectively – they retain the same depths as the T-grid for a given vertical index k. Similarly, the w-grid is interpolated from the T-grid, but retains the horizontal positioning of the latter while bracketing it above and below at at indices k and $k + 1$, respectively. The $k = 1$ position of the the w-grid is always at the surface ($z = 0\,\mathrm{m}$).

The scale factors produced by the mesh-creation procedure together define the volume of the grid cells, and thus are important for both the actual running of the model (the factors are involved in practically every calculation involving bulk properties) and later analysis (salt fluxes, heat transports, and so on being intimately linked to water volumes volumes). Letting the radius of the Earth be equal to a, in Cartesian coordinates these factors are (Madec, 2008):

$$\begin{aligned}
e_1 &= (a+z)\sqrt{\left(\frac{\partial \phi}{\partial i}\cos\theta\right)^2 + \left(\frac{\partial \theta}{\partial i}\right)^2} \\
e_2 &= (a+z)\sqrt{\left(\frac{\partial \phi}{\partial j}\cos\theta\right)^2 + \left(\frac{\partial \theta}{\partial j}\right)^2} \\
e_3 &= \left(\frac{\partial z}{\partial k}\right)
\end{aligned} \tag{2.1.7}$$

Note that because the ORCA025 configuration uses a tripolar grid, the derivatives $\left(\frac{\partial \phi}{\partial i}, \frac{\partial \theta}{\partial j}, ...\right)$ are not necessarily equal to 1. In fact, these equations are valid for any spherical coordinate system in any orientation.

2.1.5 Kinematic and Sea Ice Boundary Conditions

In any implementation of the primitive equations shown in equations 2.1.5, there are several kinematic boundary conditions that must always be satisfied. These conditions are based on solid physical laws, not the parameterizations that will be invoked extensively in later sections. There is one of these conditions for each of the surfaces involved in the problem – in this case, the sea floor and the sea surface.

Fluid flow does not penetrate through solid walls. Thus, any currents at the bottom of the ocean must flow parallel to the sea floor. This is mathematically equivalent to saying that the dot product of the velocity vector and the sea floor's normal vector must be zero, which places a restriction on the vertical velocity w. If the bathymetry at a given point (i, j) on the horizontal grid is given by $H = H(i,j)$, this restriction is written as

$$\mathbf{u} \cdot \vec{\nabla}(H) \equiv 0 \quad \Rightarrow \quad \boxed{w|_{z=bottom} = -\mathbf{u}_h \cdot \vec{\nabla}_h(H)}$$

The second kinematic boundary condition also places a restriction upon w, but occurs at the sea surface. Here, w must match exactly the rate of rise or fall of the ocean-air interface, a requirement which is more complicated than it may seem at first.

If the sea surface height anomaly from the mean for some position on the horizontal grid (i,j) is denoted by η, then w will depend on the time rate of "stretching" of the water column directly below that point: $\frac{\partial \eta}{\partial t}|_{z=\eta}$. In addition, bulges or depressions in the surface of the ocean may be advected into the area, so w also depends on an advection term: $\mathbf{u}_h|_{z=\eta} \cdot \vec{\nabla}_h(\eta)$. Finally, w may be affected by water being added or removed through precipitation (P) or evaporation (E). Therefore, the sea surface boundary condition may be expressed as:

$$w|_{\text{surface}} = \underbrace{\left[\frac{\partial \eta}{\partial t}\right]}_{\text{local stretching}} + \underbrace{\left[\mathbf{u}_h|_{z=\eta} \cdot \vec{\nabla}_h(\eta)\right]}_{\text{advection}} + \underbrace{[P - E]}_{\text{precipitation/evaporation balance}}$$

Sea ice has a major effect on oceanic conditions, especially near the surface. The ice physically serves as an intermediary between the wind and the final wind stress "felt" by the sea surface. When it melts, fresh water is injected into the surface layers, while when it forms, salt is injected through the process of brine rejection. The development of an ice model which combines realistic rheology with reasonable computational cost and accurate thermodynamics is a continuing effort (Lipscomb, 2001; Feltham, 2008). ORCA025 uses the LIM2 ice model to represent these processes, which represents ice dynamics reasonably well (Bouillon et al., 2009). However, since the majority of my domain of interest is ice-free (the exception being the portion near Greenland in winter), the ice model's potential inaccuracies are likely one of the smaller sources of uncertainty.

2.1.6 Small-Scale Parameterizations

Small-scale processes (those which occur over a spatial extent less than that between model grid points) must be parameterized for any general circulation model to function properly (Madec, 2008). These parameterizations show up in the $\mathbf{D^u}$, D^T, and D^S terms of equations 2.1.5, and generally relate to diffusive and eddy processes – energy for $\mathbf{D^u}$, salt for D^S, and heat for D^T.

The $\mathbf{D^u}$ terms generally involve separating the horizontal and vertical components from one another. These two parts can then be expressed in a variety of ways. In the case of KAB001, a horizontal biharmonic operator on velocity is used to determine the horizontal momentum diffusion component, with its viscosity parameter varying proportionally with cell volume. In the vertical, a turbulent kinetic energy scheme is implemented wherein the amount of mixing is determined chiefly by the vertical shear in velocity and the stability of the water column (Molines et al., 2006; Madec, 2008). The greater the shear, and the less the stratification, the more energy is lost (essentially to heat).

Typically, the eddy viscosities used in the horizontal are greater than those in the vertical, since timescales for horizontal mixing are usually shorter than those in the vertical. The exception to this is when the squared buoyancy frequency $N^2 = -\frac{g}{\rho_o}\frac{d\overline{\rho}}{dz}$ becomes negative, indicating an unstable water column. When this condition arises in nature, the column begins to overturn on itself, thus mixing and removing the instability. In the case of the model, however, the hydrostatic assumption has been made with the effect that these natural mixing processes are precluded. To parameterize the process instead, the model drastically increases the vertical diffusion coefficients from 10^{-4} (momentum) or $10^{-5}\,\mathrm{m}^2/\mathrm{s}$ (tracers) to $10\,\mathrm{m}^2/\mathrm{s}$ when $N^2 \leq 0$ (Molines et al., 2006). This has the effect of "tricking" the model into radically increasing the degree of vertical diffusion, thus "mixing" the water and removing the instability (Madec, 2008).

Despite this scheme, vertical mixing remains a known weak spot in many ocean models. In particular, the mixing and entrainment of overflow waters are not well understood, much less parameterized, as of yet (Legutke & Maier-Reimer, 2002), and deep convection remains similarly poorly represented (Marshall & Schott, 1999). These two processes are key to the formation and downstream evolution of water in the Nordic basins, so weaknesses in them will undoubtedly have a detrimental effect on my results. This will be shown in section 3.3.3.

The tracer terms D^T and D^S share their vertical diffusion and mixing schemes with those for momentum. However, in the horizontal they use a harmonic (as opposed to biharmonic) operator, calculated along isopycnals instead of depth levels. The diffusion coefficient varies inversely with grid size, and so is greatest at the equator and smallest near the (mesh) poles.

2.1.7 Surface Forcing Conditions and Restoration to Data

Surface forcing terms are represented by $\mathbf{F}^{\mathbf{u}}$, F^T, and F^S in the primitive equations, and may occur at either the sea floor or the sea surface.

Over ordinary timescales (in this case, $O(50)$ years), there is generally an insignificant amount of heat and/or salt gained or lost through the ocean floor (Madec, 2008). There is, however, significant momentum exchange due to friction. In the OPA model, this exchange is modelled as another diffusive process:

$$A^{vm} \frac{\partial \mathbf{u}_h}{\partial z} = \mathbf{F}_h$$

Here, A^{vm} refers to the coefficient selected for the vertical mixing parameterization discussed earlier, while $\mathbf{F}_h$ represents the actual momentum flux with the sea floor. This latter term that must be further parameterized. KAB001 does this by assuming a relation which is nonlinear in horizontal velocity (Molines et al., 2006):

$$\mathbf{F}_h = C_D \sqrt{u_b^2 + v_b^2 + e_b}\, \mathbf{u}_h^b,$$

where b specifies parameter values at the boundary, h specifies the horizontal direction, e_B is the turbulent kinetic energy, and C_D is the coefficient of drag.

Interactions at the sea surface are much more complicated. Wind stresses exert momentum fluxes which drive surface currents, while atmospheric conditions add or draw heat from the water. Meanwhile, precipitation, evaporation, sea ice, and runoff influence salinity. Because of the extreme complication of the processes involved, these boundary conditions are not generally parameterized directly, but are instead drawn from data or empirical bulk formulae. This data could come from actual observations, or reanalysis products, or a combination of both.

The OPA model requires six input data fields to drive ocean dynamics. They are:

- the two components of the wind stress vector, (τ_u, τ_v)
- net solar radiation, Q_{sr}
- net non-solar heat flux (ie. downward long-wave radiation, sensible and latent heat fluxes), Q_{ns}
- evaporation minus precipitation for liquids, EMP
- evaporation minus precipitation for solids (eg. ice, snow), EMP_s

KAB001 first initializes global temperature, salinity, and other relevant fields using values from the World Ocean Atlas (NODC, 1998). It then defines the forcing fields for the rest of the run with the CORE (Coordinated Ocean-ice Record Experiments) dataset, which itself is derived from the NCEP (National Centers for Environmental Prediction) reanalysis fields using the bulk formulae developed by Large & Yeager (2004). The wind and heat fluxes are placed directly into the model at each timestep, while freshwater fluxes are implemented as virtual salt fluxes. For example, if fresh water is being added through the melting of sea ice, the model removes salt from the surface layers. If fresh water is removed through evaporation, the model adds salt to the surface layers.

If allowed to evolve in time under the influence of only these forcings, the model will begin to drift away from observations for a variety of reasons including (but not limited to) imperfect forcing fields, imperfect parameterizations, and an inability to resolve sub-grid-scale processes. Therefore, one or more fields of the model are relaxed back toward observations in the following fashion.

For the purposes of illustration, consider sea surface temperature[5]. If the model's surface temperature at some surface point at some time t is given by $T_m(t)$, and the climatological temperature at the same time is $T_{bc}(t)$, a restoration timescale τ is chosen. This represents the amount of time over which the model value will converge to the forcing value, assuming no further dynamic evolution of the model. This allows the calculation of the necessary heat exchange per unit of time which needs to be inserted into the sea surface to have the desired effect. If the volume change with temperature $\frac{\partial V}{\partial T} \approx 0$, this can be represented as:

$$\frac{\Delta q}{\Delta t} = [T_{bc}(t) - T_m(t)] \frac{C_p}{\tau}, \tag{2.1.8}$$

where q is heat per unit volume to be added per unit of time, and C_p is the constant-pressure heat capacity of seawater. This can be converted to a temperature addition per unit of time so that

$$\frac{\Delta T}{\Delta t} = \frac{1}{C_p}\frac{\Delta q}{\Delta t} = \frac{T_{bc}(t) - T_m(t)}{\tau}, \tag{2.1.9}$$

which is intuitively obvious (I could have written it down straight away, but strictly speaking it arises from the conserved quantity of heat, not the arbitrary unit of temperature). Thus, the new temperature at that grid point is given

[5]KAB001 does not actually restore on temperature outside of the polar regions, but I believe a discussion of temperature restoration is more informative than one for salinity

by

$$T_m'(t+1) = \frac{(\tau - 1)T_m(t) + T_{bc}(t)}{\tau},$$

and it can be seen that after τ timesteps, the new temperature will, in fact, be T_{bc}. Note the use here of T' instead of an undecorated T; this is because, in addition to the relaxation calculation, other processes will also have affected the local temperature between times t and $t+1$. Therefore, T' represents the new temperature *assuming no other changes occur*.

Since the model values *do* dynamically change at each timestep (that is, in addition to the restoration term there are other terms for radiation, sensible heat flux, etc.), the model temperature will never actually reach the climatological temperature. Instead, it will merely be “pulled” in the direction of the climatology with a strength determined by τ: the larger τ is, the weaker the restoration strength. In choosing the restoration timescale value, care must be taken to strike a balance between restoring too strongly (damping eddies and not allowing new processes to evolve), and not restoring enough (and thus allowing unrealistic values to evolve).

The ORCA025-KAB001 experiment relaxes the top 10 meters (2 depth levels) of sea surface salinity in non-polar regions to World Ocean Atlas values over a relatively weak timescale of 300 days. There is no restoration of sea surface temperature. Both temperature and salinity are relaxed at all grid points (3D restoration) in the polar regions, over the relatively strong timescale of 181 days (DRAKKAR Group, 2007). For the geographical definitions used for “polar” and “non-polar”, refer to figure 2.4. These choices were made to accurately model mid-latitude processes which require accurate large-scale property values (achieved with strong, 3-D polar relaxation), while still allowing dynamical processes to evolve relatively freely (achieved with weaker SSS relaxation). Between the two areas is a buffer zone with a restoration timescale increasing towards the equator. The purpose of this zone is to smooth the transition from stronger to weaker restoration.

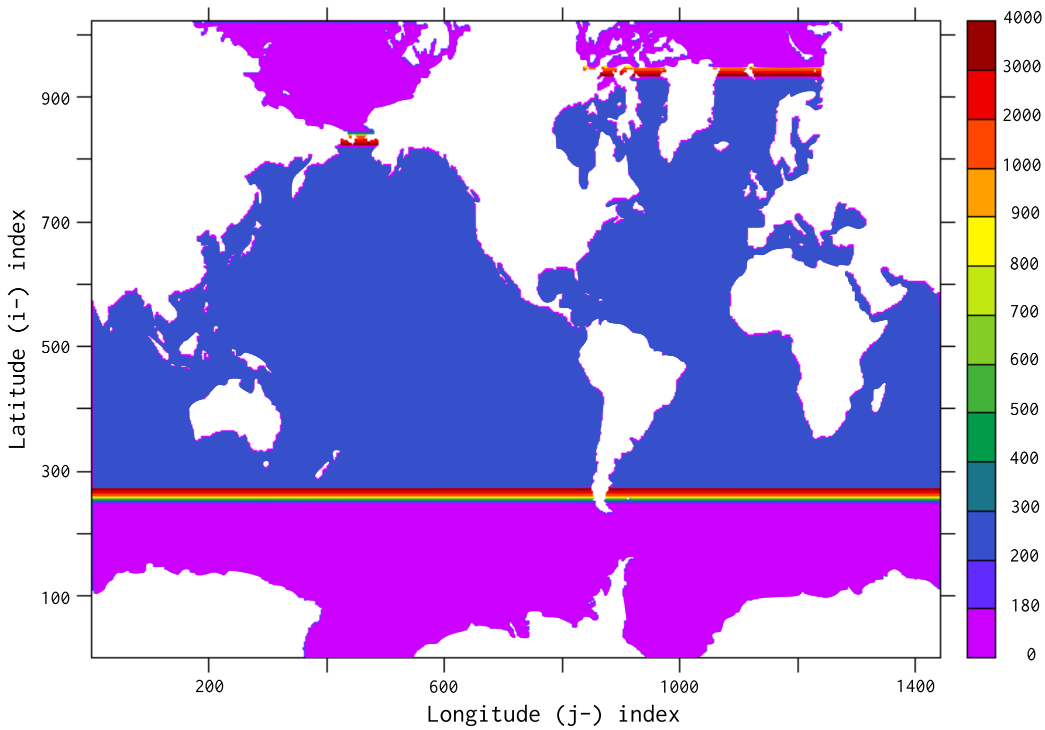

Figure 2.4: Restoration timescales in days for the ORCA025-KAB001 model. Modified version of http://wiki.ifm-geomar.de/wikiocdoc/index.php/Image:ORCA025-KAB001_damping.gif, retrieved July 26, 2010

As may be seen in figure 2.4, the region of strong polar restoration starts at the latitude of Svalbard, thus cutting through the extreme north-western portion of *my* region of interest. On one hand, this restoration will likely not affect the fate of northward-flowing Norwegian Coastal Current water – the strong restoration occurs after it passes out of the Nordic Seas. On the other hand, the restoration will affect the Arctic inflow, potentially impacting downstream dynamics (eg. transports through the Denmark Strait), ice formation

Setting	Value
Integration period	1958-2004
Ocean timestep	24 minutes
Output	5-day averages
Variable arrangement	Arakawa C-grid
Horizontal resolution	global 1/4° (27.8 km maximum, 5.6 km zonal/3.1 km meridional minima)
Vertical resolution	46 unequally-spaced depth levels
Sea ice model	LIM2
Sea ice/ocean coupling	every 2 hours
Surface forcing data	Large & Yeager (2004)
Surface forcing scheme	CORE (Griffies & et. al., 2009)
Katabatic winds	excluded
3D T, S restoration timescale (polar)	181 days
Sea surface salinity (top 10 m) restoration timescale (low-latitude)	300 days
Lateral mixing (momentum)	horizontal biharmonic operator
Lateral mixing (tracers)	isopycnal harmonic operator
Vertical mixing (momentum)	turbulent kinetic energy
Vertical mixing (tracers)	turbulent kinetic energy
Convection scheme	enhanced vertical diffusion
Bottom boundary layer	diffusive nonlinear friction

Table 2.3: Summary of settings used in the DRAKKAR ORCA025-KAB001 model

areas (eg. the formation of the Is Oden), and convection sites (eg. water mass properties in the Nord Bukta). While this issue is unavoidable, it will likely not significantly impact the flow of the North Atlantic Current-derived water masses I am interested in.

2.2 Lagrangian Particle Tracking

2.2.1 Motivation & Concept

In general, climate models take an Eulerian viewpoint on the world. They track changing velocities, pressures, temperatures, and other diagnostics at fixed points in space, but do not track the subsequent evolution of these properties in a particular parcel of fluid over time.

In a Lagrangian approach, the position and tracer values of such a fluid parcel *is* tracked through time – instead of calculating values for a set of fixed points over a range of times, the values are calculated for a set of moving virtual particles. Spatially, it could be said that the paradigm shifts from measuring the velocity at a fixed point to measuring the position of a moving point. In this way, one can track the time evolution of the particles in question.

Since most ocean and climate models are written from the Eulerian viewpoint, most Lagrangian schemes are written as add-ons to the base model code – that is, the Eulerian fields are calculated first, then the Lagrangian equations are applied to them. This procedure can be performed either online or offline from the model in question. If done online, the Lagrangian calculations can take full advantage of all the internal parameters calculated but not necessarily saved with the model, such as horizontal and vertical diffusion rates, local temperature gradients, and (critically) near-instantaneous velocities. Unfortunately, this is a not-insignificant addition to the model's complexity and, therefore, its computational cost.

If, however, the Lagrangian calculations are performed offline, the computational cost may be decreased because of the necessarily simpler implementation used (due to not being able to take into account the internal parameters as mentioned), or at least separated from the main model and thus made more convenient. It also allows particle tracking to be run on models that were never intended to have this performed internally, as is the case in my study. Unfortunately, running Lagrangian code offline also makes it less accurate – instead of using the actual fields calculated at each model timestep, one must usually make do with fields averaged over some period of time. This averaging effectively damps exceptional velocity events, such as eddies, which are often crucial to transformation processes. By using data with a relatively high temporal resolution, however, this damage may be controlled.

In addition, the internal parameters are obviously difficult, if not impossible, to take into account, thus decreasing the accuracy of the particles' positions even further. On the whole, however, Lagrangian particle tracking provides a tool which is "good enough" for most uses, and adds considerably to our understanding of many processes. The specific tool which I use is called Ariane, and was built specifically to deal with fields produced on the ORCA family of grids.

Ariane does not directly model small-scale processes. Recall that much of the convective transport and mixing in the KAB001 model is actually implemented by allowing extremely high diffusion rates in the vertical, instead of explicitly calculating (sub-grid-scale) vertical velocities. Since these velocities are not saved (or even accounted for), Ariane does not know about them. Therefore, the number of particles which experience vertical mixing and deep convection in Ariane will likely be less than the number that would in reality.

2.2.2 Equations

The basic equations used by Ariane (and most other, similar, programs) is quite simple. If $\vec{x_i}(x, y, z)$ denotes the position of a particle at some timestep i, let $\vec{v_i}(x, y, z)$ denote the background (Eulerian) velocity field at that position. If Δt denotes the length of the timestep, the equation is (Blanke & Raynaud, 1997):

$$\mathbf{x}_{i+1}(x, y, z) = \mathbf{x}_i(x, y, z) + \mathbf{v}_i(x, y, z)\ \Delta t \tag{2.2.1}$$

In execution, the scheme is similarly simple. The velocity field at the point (x, y, z) is interpolated from the surrounding velocity data points (Ariane uses a bilinear interpolation scheme), equation 2.2.1 is applied, and the new position is saved. In addition, Ariane (bilinearly) interpolates density, temperature, and salinity data at each position for each particle. After all these calculations have been performed, the process is repeated for the next timestep.

The process gets more complicated if the velocity for a particle will not be well-defined over the duration of a given timestep. This occurs if the particle passes out of one grid cell and into an adjacent one at some time between one timestep and the next. In order to maintain accuracy, one must devise a way to (1) detect if a particle *will* exit a gridcell during a calculation, and (2) deal with it if it does.

2.2.3 Crossing Times and Locations

The amount of time it will take a particle to cross from one side of a grid cell to the other (see Figure 2.2 for the layout of a typical cell) is given by the relation (Blanke & Raynaud, 1997)

$$\Delta s = \frac{1}{\Delta F} \ln \left(\frac{F_o + \Delta F}{F_o} \right) \tag{2.2.2}$$

in general, or if $\Delta F = 0$, the limit as $\Delta F \to 0$:

$$\Delta s = \frac{1}{F_o} \tag{2.2.3}$$

The parameters for both of these equations are given in Table 2.4.

Parameter	Value/Meaning
Δs	time to cross cell, given the flux difference ΔF
ΔF	difference in volume flux between two opposing faces of a cell $(F(i+1) - F(i))$
F_o	volume flux through the face with the lower index, $F(i)$

Table 2.4: Meaning of parameters appearing in Equations 2.2.2 and 2.2.3

The calculation shown by equation 2.2.2 or 2.2.3 is performed in each of the $\hat{\imath}$, $\hat{\jmath}$, and $\hat{\mathbf{k}}$ directions at each timestep; Δs will be defined in at least one of them, due to the assumption of nondivergence (this assumption, incidentally, is valid here in all situations, since it is built into the OPA model. Thus, all output fields will respect the nondivergence condition perfectly. In fact, the w field is not explicitly calculated by OPA from the primitive equations – it is calculated from the nondivergence of the water column, with an algorithm similar to Ariane's for the same calculation! (Madec, 2008; Blanke & Raynaud, 1997)). If the smallest of the times defined thus is less than the duration of the timestep, the particle in question will exit the grid cell at some point before that timestep is completed, and it therefore gets special treatment.

This treatment is equivalent to using Equation 2.2.1, but replacing Δt with Δs. At the endpoint of that calculation, the particle will have entered the adjacent grid cell. Then, the various flux values that the equation is implemented with are recalculated for the new cell, and the time integration performed once more over time interval $\Delta t - \Delta s$. The particle's position at the end of this second calculation is the one that is saved to the output files, and is also the one that salinity, temperature, and density are interpolated onto. For my experiments, Ariane saved particle position and property values every three days.

Chapter 3

Analysis

3.1 Model Validation

3.1.1 Large-Scale Properties

In order to confirm that the model is producing reasonable results, let us examine the typical currents it produces both near the surface and at depth.

Surface

Figure 3.1 shows the velocity field at a depth of 10 meters, averaged over the 36-month period beginning in October 1984. This depth was chosen to capture the dynamics of the surface layer, while averaging over such a long time period removes the high-frequency variations which would otherwise potentially mask the mean flow. I chose a period of three years to match the length of my Ariane experiments – the fields shown are what the particles in the experiments would, on average, experience during their runs. October 1984 was arbitrarily chosen to represent a typical experiment; plots for other experiments look similar.

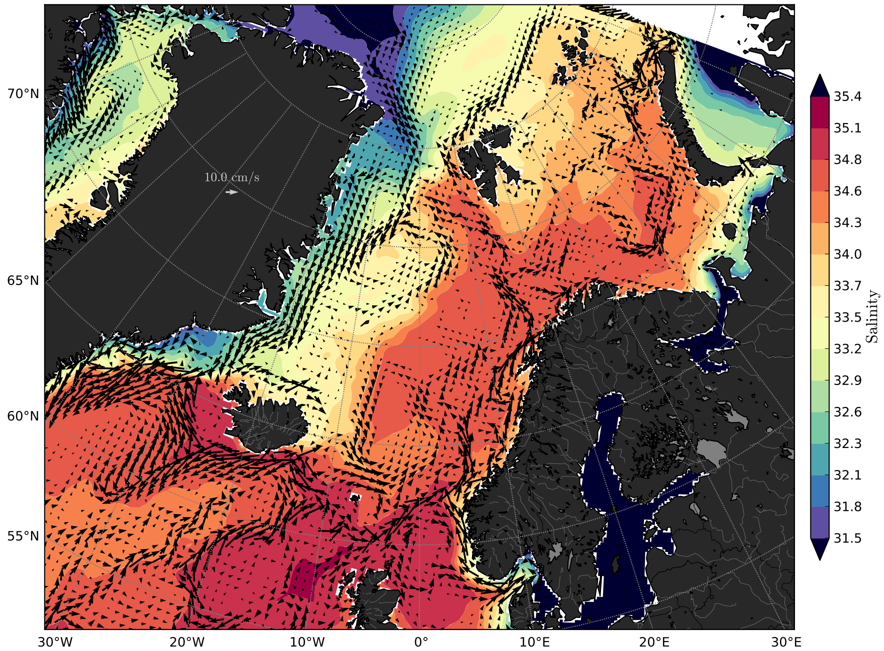

(a) 10 meters, salinity contours

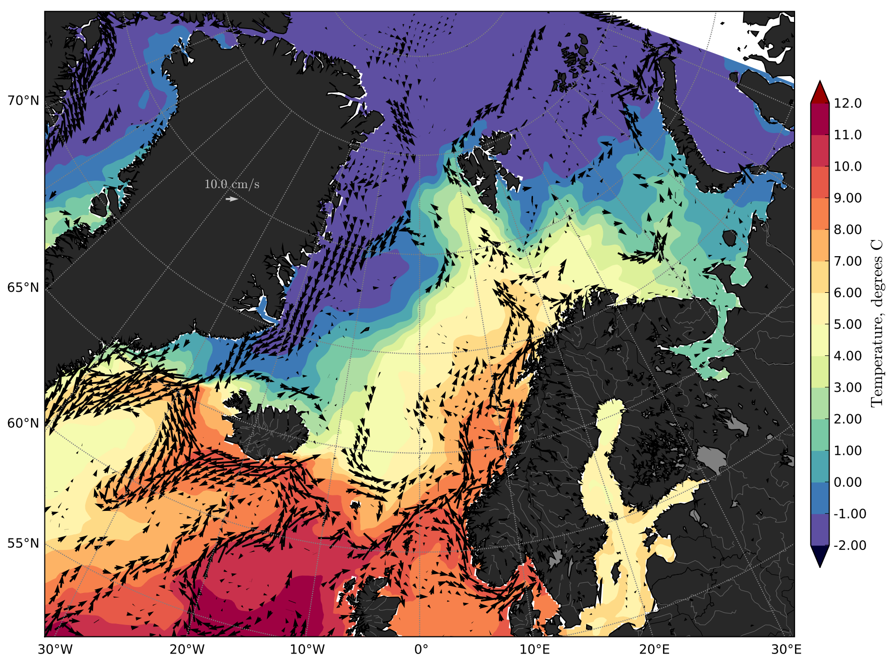

(b) 10 meters, temperature contours

Figure 3.1: Arrows show velocity at a depth of 10 meters for every third horizontal gridpoint, averaged over the three-year period beginning in October 1984. Points with velocity less than 2 cm/s have no arrow. The colours in (a) show salinity averaged in a similar fashion at the same depth; colours in (b) show averaged temperature. The velocity scale arrow is found in Greenland.

In both plots, the signature of warm, salty North Atlantic Current water is clearly evident along the west coast of Norway and extends across the GIN seas about half-way to Greenland. Notice also the recirculation around the Jan Mayen Ridge (the cause of the wintertime Is Oden – refer to section 1.3.3), the center of which is relatively cold compared to its surroundings. A weaker gyre is also visible in the southern Norwegian Sea. Both of these are quite steady in that they are visible in essentially any season or year of interest, though they do vary somewhat in strength. Other, occasionally quite strong, gyres exist as well (particularly, and crucially, around the Icelandic Sea), and we will see evidence of them in sections 3.3.1 and 3.3.2. However, they tend to not be as persistent in time as the ones seen in figure 3.1, and so are not visible in it.

Temperature distributions in the Norwegian Sea are consistent with those shown by Aagaard et al. (1985), though surface salinity is too low (averaging about 34.7 instead of the observed 35.0). The Greenland Sea is likely too fresh as well at 33.8, compared to the observed “< 34.8”. The temperature there agrees with observations, however, at about 2°C.

The major surface pathways are all represented in terms of velocities. The currents through the DS and FSC may be seen, with that over the IFR less so. The latter is likely because the flow exists only over a narrow horizontal extent which is rather changeable in position, causing its signature to be weakened in any long-term average. Notice also that the majority of the flow through the FSC is *to* the Nordic region, as opposed to that through the DS where the flow is predominantly *from* the GIN seas.

The bifurcation of the Norwegian Coastal Current is clearly represented, centered at about 65°N, with the current splitting just to the south of there (where the shelf widens) and reconnecting just to the north. Also notice the good representation of the East Greenland current in terms of both current strength and temperature/salinity properties. Together, then, the model's surface characteristics seem acceptable.

Mid-Depth

Figure 3.2 is similar to figure 3.1, except drawn at 500 meters depth. Salinity is noticeably higher compared to figure 3.1a at all points, but changes in the temperature field are not so uniform. On the entire eastern side of the region, temperatures are lower than near the surface, while on the western side, they are higher. This is because the temperature and salinity properties of both the Norwegian Coastal Current and the East Greenland Current (especially the latter) do not extend very deep, perhaps only 200 m (see figure 3.6). Since these currents are relatively warm and cold, respectively, the water beneath each will be relatively colder and warmer than the currents themselves.

The gyres near the surface seen in figure 3.1 are still present at this depth, and are especially evident in the temperature field. They are probably also visible in the salinity field, but because salinity variations at this depth are generally quite small, a different colour scale would need to be used to see them. For the purposes of comparison I have elected to use the same colour scale for figures 3.1 and 3.2.

Salinity at 35.0 in the Norwegian Sea and 34.8 in the Greenland Sea

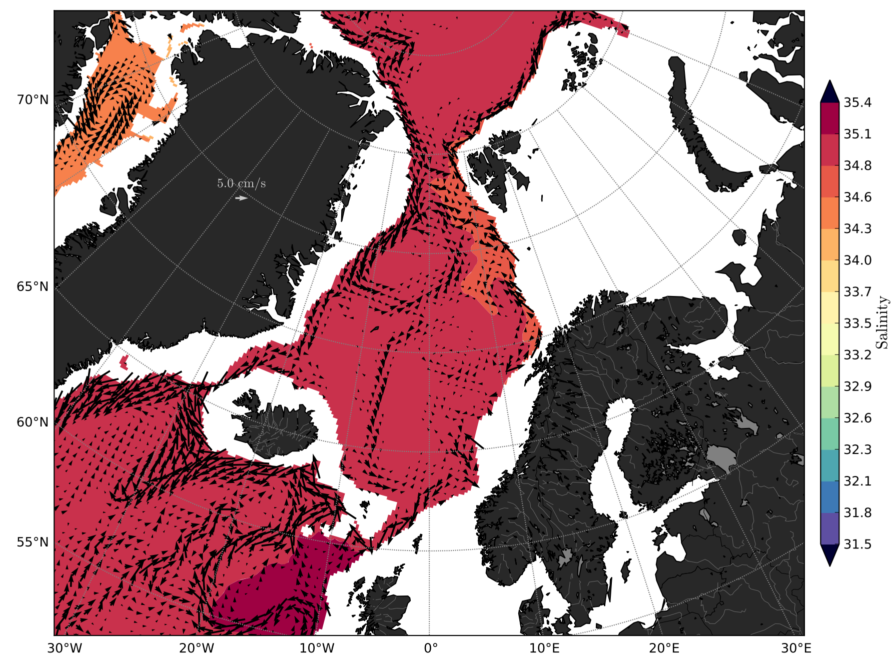

(a) 500 meters, salinity contours

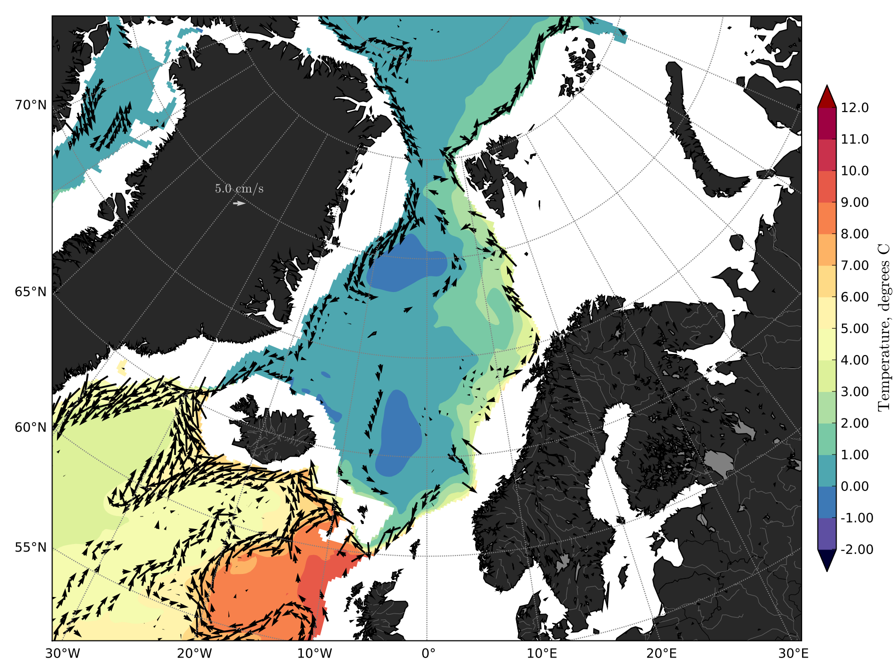

(b) 500 meters, temperature contours

Figure 3.2: Arrows show velocity at a depth of 500 meters for every third horizontal gridpoint, averaged over the three-year period beginning in October 1984. Points with velocity less than 1 cm/s have no arrow. The colours in (a) show salinity averaged in a similar fashion at the same depth; colours in (b) show averaged temperature. The velocity scale arrow is found in Greenland.

matches Aagaard et al. (1985); temperature in the Norwegian Sea matches observations as well, at 3-5°C, and in the Greenland Sea at 1-2°C.

There is clearly little inflow at this level, as will be confirmed in section 3.1.2. We will see that both the DS and the FSC are mainly exporters below 200 meters, while the IFR is essentially an impenetrable barrier. Notice in particular the outflow of the FSC, turning north upon exiting to flow through the Faroe Bank Channel, in agreement with Hansen & Østerhus (2000). In September 1998 Hansen et al. (2001) observed velocities of up to 50 cm/s in the Faroe Bank Channel, which at first seems to suggest the model is under-representing the outflow. However, the fields shown here are averaged over three years, likely masking many high-velocity events.

It is also interesting to note that at the bifurcation of current around the Rockall-Hatton Plateau (about 57°N, 15°W), both the 10 meter and 500 meter plots show much of the water flowing around the northern and western sides of the rise instead of following the southern, more direct, route to the FSC. This may explain the higher-than-expected transports across the IFR, to be discussed in section 3.1.2.

Mixed-Layer Depth

In order to see how well the model represents the classic deep convection sites, let us next examine the mixed-layer depths in the Nordic region. These tend to be highly variable in both space and time, and are thus difficult to present in only a few figures. To attempt to do so, I have plotted the mean mixed-layer depth (defined, in this case, as the depth at which the density has increased by 0.01 kg/m^3 from its surface value), along with its standard deviation, for March in the consecutive years 1964-1966, 1983-1985, and 2002-2004, in figure 3.3. March is the month that tended to have the deepest mixed-layer depths.

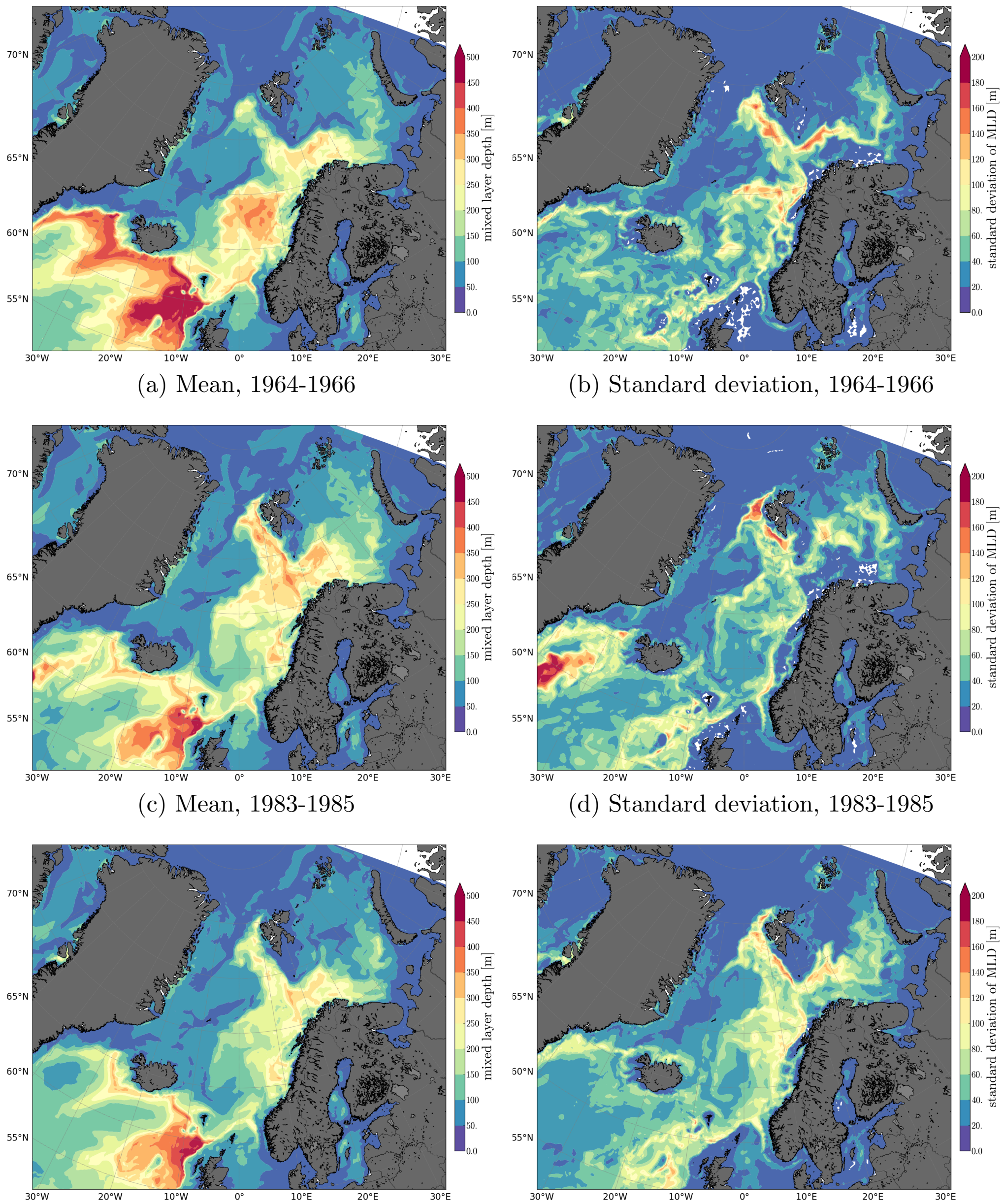

(a) Mean, 1964-1966

(b) Standard deviation, 1964-1966

(c) Mean, 1983-1985

(d) Standard deviation, 1983-1985

(e) Mean, 2002-2004

(f) Standard deviation, 2002-2004

Figure 3.3: Mean and standard deviation of March mixed-layer depths for the years 1964-66, 1983-85, and 2002-04.

From these plots, we can see that the there is usually a region well-mixed to around 300-400 m northwest of Norway throughout the model run – in fact, much of the Norwegian Sea as a whole tends to be mixed down to around 250 m. Another persistently well-mixed area, this time to deeper than 450 m, is found south-west of the Faroe-Shetland Channel at about 60°N, 10°W. The areas with noticeable mixing also tend to have large standard deviations, indicating that they are quite variable over the averaging period. In contrast, in other areas where we would expect a large mixed-layer depth due to deep convection, such as in the center of the gyres around Greenland Sea and the southern Norwegian Sea (seen in section 3.1.1), the mixed-layer depth is quite shallow (50-100 m) and has quite low standard deviations. Therefore, the model does not appear to represent deep convection properly in these areas.

Overall, then, the model seems to represent current paths and properties quite well, provided one is confined to predominantly horizontal flows. However, it does not appear to represent deep convection very well, probably due to its somewhat simplistic method of dealing with conditions conducive to such mixing – that is, merely switching vertical diffusion to a very high value. It is therefore unlikely that my Lagrangian particles will exhibit classical convective behaviour along their trajectories, since these processes are not being explicitly represented by the model. The model likely does represent the formation of mid-depth water masses reasonably well, however, since the processes which create such masses do not rely on energetic vertical mixing or deal with steeply sloped isopycnal surfaces. This, combined with the fidelity at which the horizontal currents are represented, ensures that interesting dynamics will still be experienced by the particles.

3.1.2 Virtual Sections

Having now gained a good understanding of the large-scale, regional picture, let us examine the behaviour of the straits which connect the Nordic Seas to the North Atlantic. To do so, I defined three virtual sections along the Greenland-Scotland Ridge by picking start and end points (in latitude/longitude coordinates) for each section. I then found the model grid points which were closest to these geographical locations. Finally, the model points which most closely approximated a great circle line between these two endpoints for each section were found. The termini used and the great circle distances between them are shown in table 3.1, along with the mean and maximum depths of the straits thus defined. The resulting sections are shown graphically in figure 3.4.

Section	**Start**	**Finish**	**Length (km)**	**Mean Depth (m)**	**Maximum Depth (m)**
Denmark Strait (DS)	68.6° N 27.1° W	66.4° N 23.0° W	300	601	1435
Iceland-Faroe Ridge (IFR)	64.4° N 14.6° W	62.2° N 7.2° W	442	378	619
Faroe-Scotland Channel (FSC)	61.4° N 6.9° W	58.5° N 6.6° W	323	444	1040

Table 3.1: Start point, end point, distance spanned, and depth statistics for the virtual sections described in section 3.1.2.

Volume Transports – Mean Flows

I first calculated the volume transports across each strait for both an upper (nominally, above 200 meters depth) and a lower (below 200 meters) layer, with total transports for each layer being calculated by adding together the contributions from each strait.

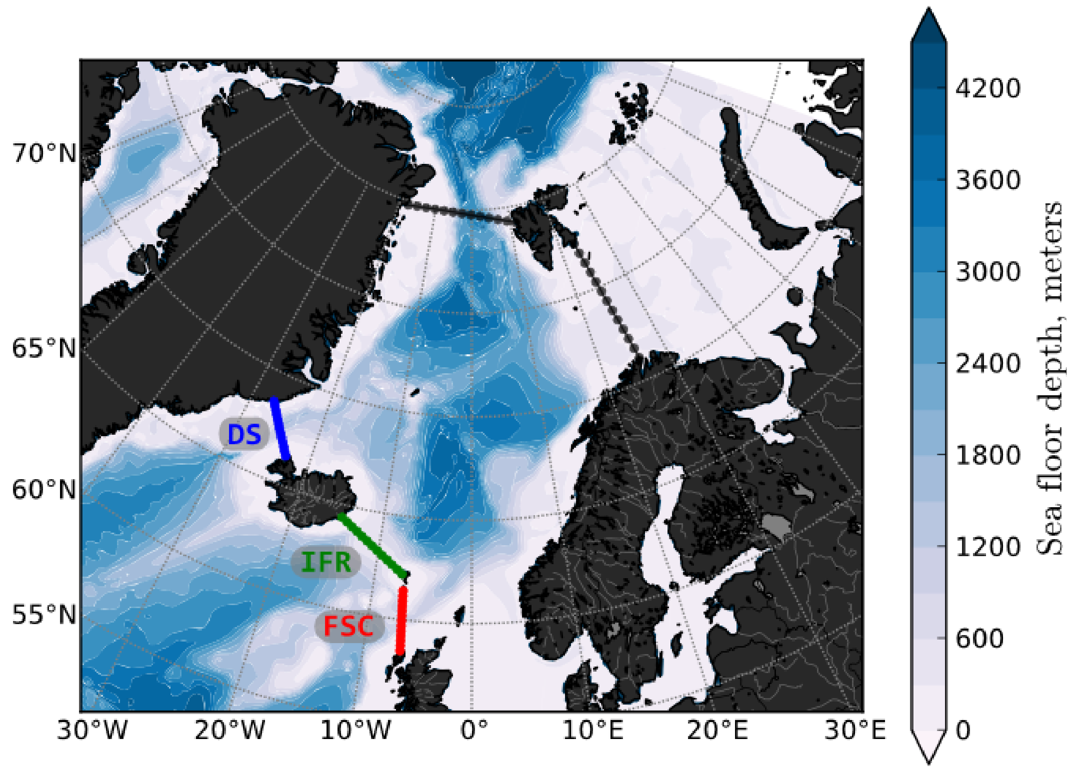

Figure 3.4: Geographic positioning of sections, along with their abbreviations as defined in table 3.1.

The choice of 200 meters as the cutoff level is somewhat arbitrary, since there is no clear (depth) distinction between surface and deep flows. However, this depth seemed a reasonable compromise between being deep enough that the deep flows are not unduly influenced by the surface flows, while being shallow enough that the surface flows are not unduly influenced by the deep. A 90-day average filter was applied to the resulting timeseries, of which the outcome is shown in figure 3.5. The filtering was performed to remove much of the noise from the original signal; without it, the plots appear somewhat unclear when shrunk to printable size.

The mean values and associated standard deviations for the unfiltered timeseries are shown in table 3.2. The surface layer of the IFR actually imports the most water, while also exporting a large amount. The inflowing water is mostly of North Atlantic Current origin, while the export is likely part of the North Icelandic Irminger Current recirculating around the eastern side of Iceland. The same North Icelandic Irminger Current makes up the majority of the DS surface import, but most of the flow in that strait is export from the East Greenland Current. Finally, near the surface the FSC is almost strictly an importer of water, with a very little (again from the North Icelandic Irminger Current) recirculating out past the Faroe Islands.

The deep characteristics are quite different. Below 200 meters, the FSC exports vast quantities of water, while the DS exports a full Sverdrup less (FSC = 4.28 Sv; DS = 3.27 Sv). However, the FSC continues to import a notable quantity (1.82 Sv) as well, largely due to the North Atlantic Current extending well below 200 m. In contrast, the DS imports very little via the much shallower North Icelandic Irminger Current. The IFR, meanwhile,

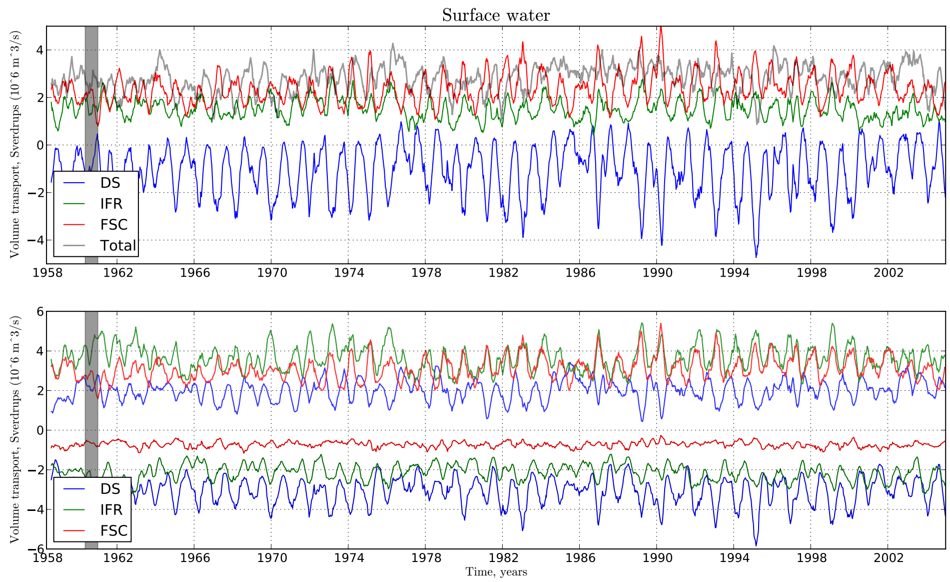

(a) Volume transport from surface to 200 m

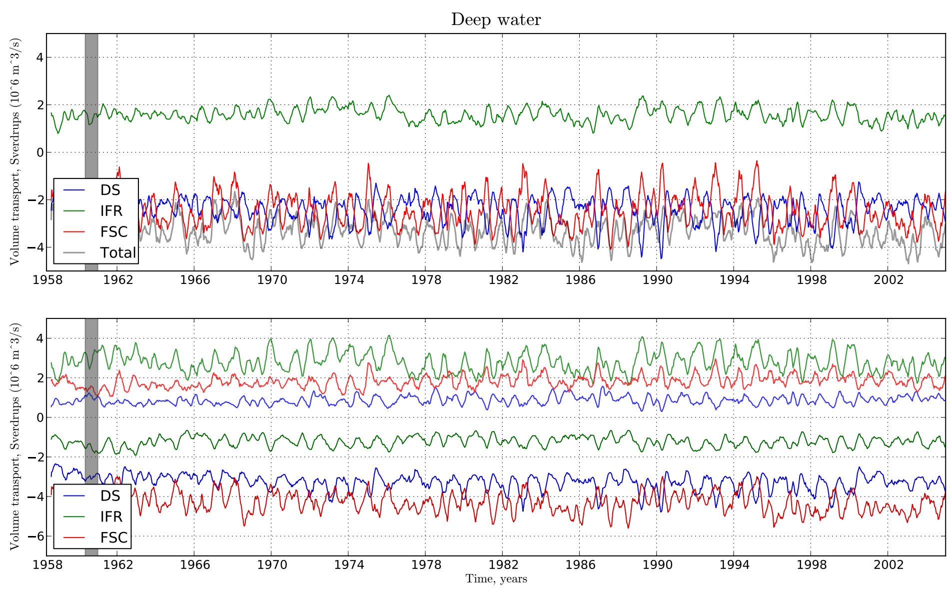

(b) Volume Transport from 200 m to bottom

Figure 3.5: Surface and deep volume transports across the three sections. The upper portion of each subplot shows the total transport across each strait, averaged over the previous 90 days. The lower portion of each shows components both in to (+) and out of (-) the Nordic Seas through each strait. Due to missing model data in 1960, values in the grey regions are not to be trusted.

stands in marked contrast to the other two straits by continuing as a net importer of water. This is likely due to its much shallower mean and maximum depths – 66 meters shallower than the FSC on average, and 421 meters less at maximum – which limits the amount of deep water able to be exported.

Overall, the model fluxes are of consistently greater magnitude than those actually observed. For example, according to Mauritzen (1996b)'s inverse box model, total Atlantic inflow through all three straits should be about 8 Sv; instead, KAB001 predicts 8.75 Sv just in the top 200 m. The same paper specifies 0.5 Sv of recirculation from the North Icelandic Irminger Current through the IFR; instead, KAB001 predicts 2.1 Sv. Many of these differences, particularly in the IFR case, may be attributable to meandering currents. If the flow curves enough, it may get counted as outflow, then turn back in as inflow, or vice versa. Despite most transports being off by a factor of two or more, it is likely that the *proportions* and, just as importantly, the variability, between various transports remain realistic.

Section	**Mean Transport (Sv)**			**Std. Dev. (Sv)**
	+	−	**Total**	**Total**
`Upper (0 - 200 m)`				
Denmark Strait (DS)	2.00	-3.08	-1.08	1.80
Iceland-Faroe Ridge (IFR)	3.65	-2.14	1.51	0.88
Faroe-Shetland Channel (FSC)	3.10	-0.73	2.37	1.15
Total	8.75	-5.94	2.81	1.32
`Lower (200 m - bottom)`				
Denmark Strait	0.87	-3.27	-2.40	1.00
Iceland-Faroe Ridge	2.80	-1.22	1.58	0.50
Faroe-Shetland Channel	1.82	-4.28	-2.46	1.32
Total	5.49	-8.77	-3.28	1.11

Table 3.2: Mean transports across the entrance straits for the entire model record (1958-2004), along with their associated standard deviations. Positive mean values represent transport *into* the Nordic Seas.

All straits, at both surface and deep levels, exhibit a clear annual cycle. However, there does not appear to be a significant long-term trend to the total transport or its components over the model record at either level.

In terms of variability, that of the surface FSC flow is dominated by the volume of inflowing water; the outflow is so small that its variability has little impact on the total. Surface flow over the IFR similarly appears governed by the inflow, but here the picture is complicated by the fact that both inflow and outflow rates vary with each other – that is, as the inflow flux increases, so does the outflow flux. However, the inflow changes seem to have the higher magnitude overall, thus setting the variability.

The surface DS variability is, again, different than the other two straits: as the inflow flux increases, the outflow flux decreases, and vice-versa. Thus, both flows appear at first glance to set the overall variability together. However, from the hydrographic cross-sections of the strait to be seen in section 3.1.3, it seems clear that the East Greenland Current is the dominant factor – when it strengthens, it tends to widen and decrease the area available for the North Icelandic Irminger Current to flow into the Icelandic basin.

Deep variability is quite similar to that near the surface, with two exceptions. First, the variability tends to be slightly less than that at the surface (~ 0.94 Sv vs. ~ 1.28 Sv). Second, the FSC inflow/outflow relationship is reversed, this time with the latter dominating the former. That said, the inflow still has a fairly high mean value (1.82 Sv) since the inflowing North Atlantic Current water extends well below my arbitrary level of 200 m in this area.

In total, the IFR is the only net importer of water. The FSC is a net exporter, but only just – its strong deep flows are nearly balanced by strong surface flows of great horizontal and vertical extent. The DS has strong outflowing currents both on the surface and in the deep, making it the greatest exporter of the three. The total flow both at the surface and in the deep through the DS tend to be out of phase with that for the IFR and FSC, which will be confirmed in the next section.

Adding together the total upper and lower transports, it is apparent that the Nordic region exports a net 0.47 Sv on average. Much of the additional export water (ie. that which did not originally enter the Nordic and Arctic regions over the Greenland-Scotland Ridge) is from the Pacific via Bering Strait, with an insignificant amount contributed by continental runoff. Typical total transports through Bering Strait are 0.8 ± 0.5Sv. If the resulting outflow is split evenly between the Canadian Arctic Archipelago and the GIN seas (a reasonable assumption, based on the budgets presented in (Dickson et al., 2007)), this implies that the latter should export about 0.5 Sv, which agrees well with the model.

Volume Transports – Correlations

The zero-lag cross-correlations between the various volume transport time-series are shown in table 3.3. The high degree of anticorrelation (-0.680) in the surface flows between the Denmark Strait and the Faroe-Shetland Channel is of particular interest, since it suggests that one somewhat compensates for the other. This is likely dependent on how far south the eastward-flowing branch of the sub-polar gyre is pushed; if it is further south, flow through the FSC would likely increase while that through the DS would decrease, with the opposite holding true if the sub-polar gyre comes further north. In fact, Taylor & Stephens (1998) observe that in high-North Atlantic Oscillation years, the North Atlantic Current generally moves further north compared to low-North Atlantic Oscillation years (with a time lag of several years). Therefore, a similar link between the relative transports of the DS/FSC and the Oscillation likely exists, but is beyond the scope of the present study. A similar situation may exist between the DS and the IFR, since they are also somewhat anticorrelated with one another, though in this case the relationship is weaker (-0.452) and it is difficult to say what causes the fluctuations. Finally, the relatively strong relationship of the total flow to that through the DS and IFR (0.468 and 0.334, respectively) suggests that those two straits contain much of the variability of the total, while the FSC remains somewhat more predictable in its annual cycle. In sum, these results match nicely with the ideas put forward by Serra et al. (2010).

Upper (0 - 200 m)				
	DS	**IFR**	**FSC**	TOTAL
DS	1.000	-0.452	-0.680	0.468
IFR	-0.452	1.000	0.328	0.334
FSC	-0.680	0.328	1.000	0.163
TOTAL	0.468	0.334	0.163	1.000

Lower (200 m - bottom)				
	DS	**IFR**	**FSC**	TOTAL
DS	1.000	-0.526	-0.563	-0.012
IFR	-0.526	1.000	0.181	0.197
FSC	-0.563	0.181	1.000	0.771
TOTAL	-0.012	0.197	0.771	1.000

Table 3.3: Tables of correlation coefficients between the various volume transports across the entrance straits. The value of -0.012 (DS/Total) has a probability of occurring randomly of about 50%; all other values have negligible probability of occurring randomly. Note that "Total" means total import/export across the Greenland-Scotland Ridge.

The total deep transport is very weakly correlated with the transports through the DS and IFR (-0.012 and 0.197, respectively), while being strongly linked to the FSC (0.771). The irrelevance of the IFR is relatively easy to accept, since it does not extend very deep and tends to import (rather than export) water from the Nordic Seas. The irrelevance of the DS, however, is more puzzling. The reasons behind this are unclear, but the fact that much of the DS outflow is of Arctic, rather than Nordic, origin, may be a good place for future work to begin.

3.1.3 Hydrography

Setup

Having now gained a good understanding of the relative importance and interrelationships of flows over various parts of the Greenland-Scotland Ridge, I wish to characterize the water masses present in each of the straits. To do so, I rotated the model u- and v-velocity components into their true zonal and meridional components. I then bilinearly interpolated them onto thirteen (endpoint-inclusive) evenly-spaced locations along the virtual sections discussed earlier. This interpolation was done independently for each depth level.

Because of concerns regarding computational cost, and for practical reasons involving the Ariane program (to be discussed in section 3.2), this interpolation was only done in January, April, July, and October of every fourth year from 1962 to 2000. Combined with the use of only thirteen (horizontal) points in each section, this resulted in an undersampling of available data in both space and time, but preserved the general hydrographic structure in each section and season while reducing the amount of data to a manageable amount. (For reference, the virtual sections used in section 3.1.2 contained the following number of horizontal model points: DS=28, IFR=27, FSC=20). Let us first discuss the Denmark Strait section, shown in figures 3.6a to 3.6c.

Denmark Strait

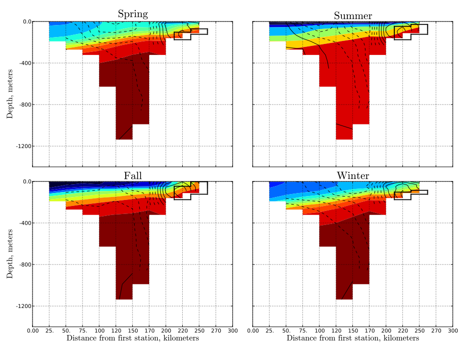

(a) Mean salinity

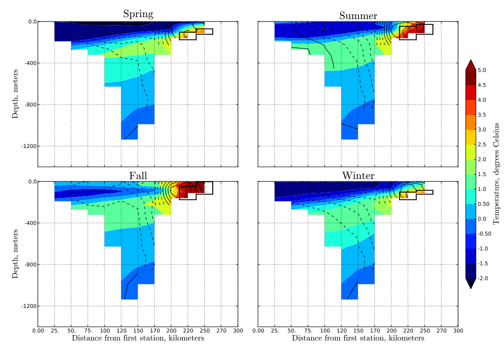

(b) Mean temperature

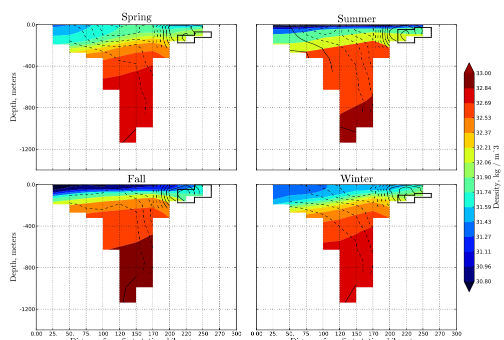

(c) Mean potential density, referenced to 1000 meters

Figure 3.6: Spatially interpolated salinity, temperature, and potential density in the **Denmark Strait**, averaged seasonally every four years from 1962-2000. Contour lines represent cross-strait velocity, and are spaced 3 cm/s apart; solid lines indicate flow into the Nordic Seas, and dashed lines from them. The zero contour is solid. The regions enclosed in thick black lines are those defined to contain North Atlantic Current water (see table 3.4). The left ends of the plots are in Greenland, while their right ends are in Iceland.

It is clear that the water near the surface and hugging the coast of Iceland remains much warmer than its surroundings, with this tendency strongest in the summer months and weakest in winter and spring. A similar, though much weaker, signature exists in the salinity plots. Ironically, the effects of high temperature and salinity somewhat cancel one another out when calculating density, causing the surface isopycnals to stay relatively flat. Even so, they do tend to slope downward slightly near Iceland. Due to the very fresh water in the East Greenland Current, they also form a broad downward slope toward Greenland, leaving a noticeable peak about three-fifths of the way across the strait. This could be seen as a rough boundary between the influence of outflowing water in the East Greenland Current and the inflowing water of the North Icelandic Irminger Current. It is also clear that in winter the strength of the North Icelandic Irminger Current decreases while that of the East Greenland Current increases, thus promoting export of surface water. The opposite is true in summer, coinciding well with the timeseries shown in figure 3.5a. Finally, notice the clear temperature signal of the East Greenland Current: in summer, it tends to be very broad, and constrained quite near the surface due to its buoyancy. Even in fall, after a summer of (relatively) strong warming of the upper waters, there is a distinct tongue of cold water perhaps 150 meters below the surface.

Iceland-Faroe Ridge

Figures 3.7a to 3.7c show a somewhat different situation over the Iceland-Scotland Ridge. Plots of both temperature and salinity for individual months indicate water properties that are somewhat homogeneous in the vertical, especially in winter. The lateral position and strength of inflowing Atlantic water varies from month to month, but tends to be separated from the Icelandic coast by cooler water presumably wrapping around the island's northern side.

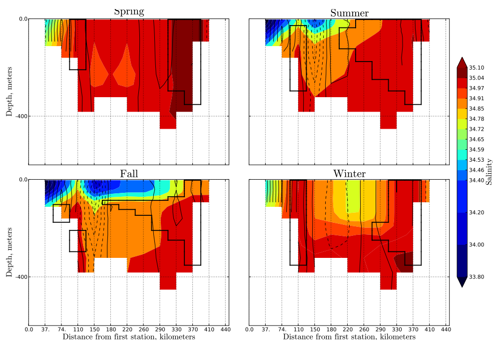

(a) Mean salinity

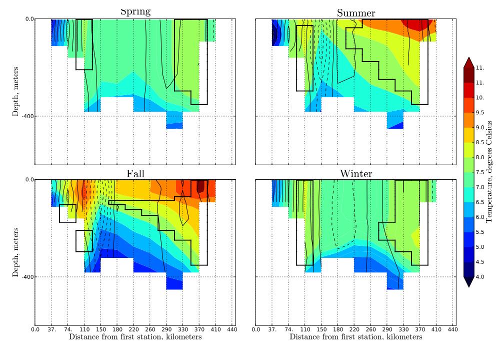

(b) Mean temperature

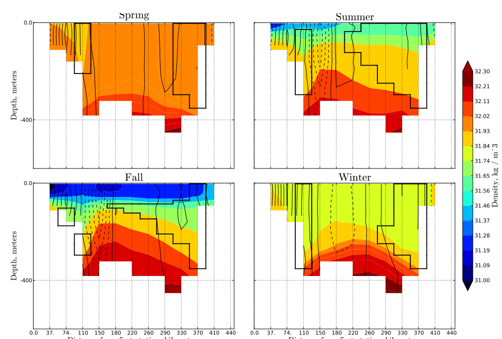

(c) Mean potential density, referenced to 1000 meters

Figure 3.7: Spatially interpolated salinity, temperature, and potential density over the **Iceland-Faroe Ridge**, shown in a fashion similar to figure 3.6. The left ends of these plots are in Iceland, while their right ends are in the Faroe Islands.

The vertical homogeneity of properties, the erratic positioning of currents, and the highly variable relative strengths of the currents suggest that much of the behaviour in this area is eddy-driven. It is also interesting to note that more structure tends to appear as summer wears on, while convective activity in the winter tends to reset the system. This pattern is most apparent in the temperature and salinity plots, but is also noticeable in the potential densities. In general the the deep overflows here are not strong due to the sill's rather shallow depth.

Faroe-Shetland Channel

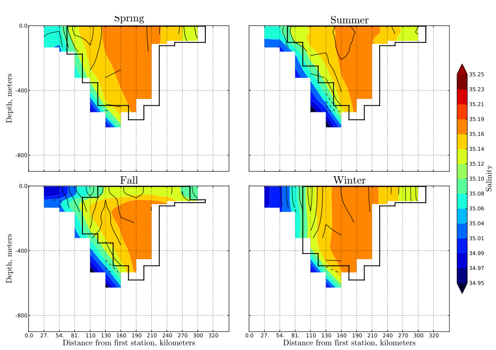

(a) Mean salinity

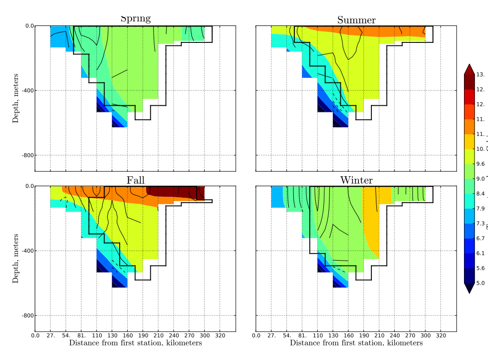

(b) Mean temperature

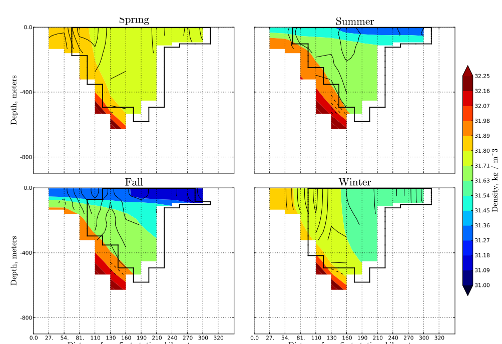

(c) Mean potential density, referenced to 1000 meters

Figure 3.8: Spatially interpolated salinity, temperature, and potential density in the **Faroe- Shetland Channel**, shown in a fashion similar to figure 3.6. The left ends of these plots are in the Faroe Islands, while their right ends are in Scotland.

In contrast to the IFR, properties in the FSC (shown in figures 3.8a to 3.8c) are relatively steady. There is a persistent flow of North Atlantic water on the southern side of the strait which extends quite deep, even past 400 meters. There is also a persistently strong outflow at greater depths which does not show up well in these contour plots, but which can be easily inferred from the deep transport timeseries shown in figure 3.5b.

Temperature-Salinity Diagrams

Figure 3.9 characterizes the water masses found in the entrance straights. Clearly, the coldest and densest ($\sigma_{1.0} \approx 1028.0\,\mathrm{kg/m^3}$) water tends to be found in the Denmark Strait – notice the hook-like structure near $S = 34.9$ and $T = -0.5$°C which extends upward at almost constant salinity until about 2°C. This is a likely constituent of the deep overflows. A similar mass exists in the Faroe-Shetland Channel, though its signature is not nearly as strong. It doesn't, however, appear to exist at all over the Iceland-Faroe Ridge. Therefore, it is likely that the majority of very dense water in the model exits through the Denmark Strait.

In addition to the densest water, the Denmark Strait also contains the lightest ($\sigma_{1.0} \approx 1025.5\,\mathrm{kg/m^3}$) and freshest ($\sim 31.7$) water thanks to the East Greenland current. That current's abundance of fresh water comes from both the Arctic and runoff from Greenland, as evidenced by its solidly subzero temperature. In comparison to the two extreme signals, the signature of the North Icelandic Irminger Current in the DS is relatively weak, as shown by the comparative lack of points meeting the definition of that water mass.

The masses in the IFR and FSC fall into a much narrower tempera-

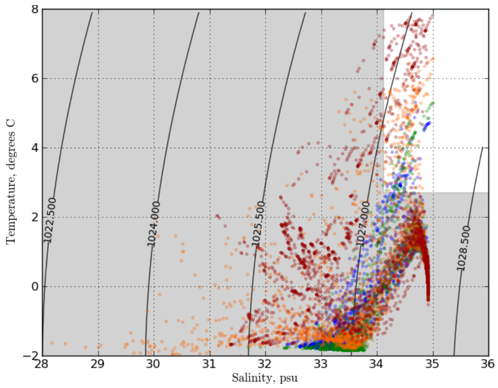

(a) Denmark Strait

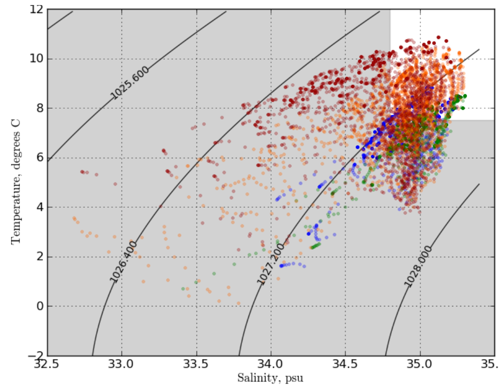

(b) Iceland-Faroe Ridge

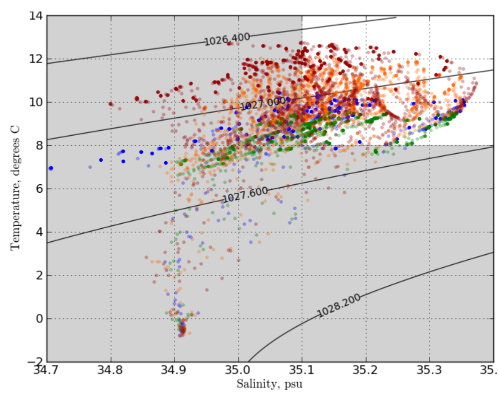

(c) Faroe-Shetland Channel

Figure 3.9: Spatially interpolated temperature/salinity data for all years and months for which model data was projected onto the virtual sections. Colour indicates season; points *not* in the region with the gray background are defined to be part of the North Atlantic current.

ture/salinity/density regime. The IFR water appears to be particularly well-mixed, and exhibits a noticeable seasonal cycle by running from cold and saline (6−8°C, 34.7−35.3) in spring to warm and fresh (8−11°C, 34−35) in fall. The FSC appears to contain distinct water masses, but it is difficult to demix them from one another and thus draw conclusions about their various behaviours. However, the FSC is generally about 2°C warmer and 0.2 saltier than the IFR. Also, both the IFR and FSC contain a significant number of points which *do* match the criteria for North Atlantic Current water, plotted outside the grey area (see section 3.2).

It should be mentioned here that points representing surface water are somewhat overrepresented here, compared to those representing deep water. This is because of the model's concentration of depth levels near the surface (see section 2.1.4 for details).

3.2 Setup of the Lagrangian Experiments

3.2.1 Sampling Intervals

The motivation for using the Ariane tool was to track the inflowing North Atlantic water's position and properties over time, with the end goal of characterizing the behaviour of that part of the inflow which becomes the deep overflow. These outflow properties and strengths are likely to change over a range of timescales from short (seasonal) to long (decadal). On the other hand, to try and characterize the outflow for every output timestep of the model (ie. every five days) would be impractical.

Therefore, a balance had to be struck between the amount of data being amassed (a function of time resolution and number of particles used) and practicality. To this end, it was decided to initialize particles for use with Ariane in winter (January), spring (April), summer (July), and fall (October) every four years from October of model year 1960 to October 2000. The particles would then be tracked for a period of three years (36 months) following their initialization, calculated using one-day timesteps. I did not initialize particles earlier in the model output because of missing tracer (temperature/salinity) data in the first four months of 1960.

3.2.2 Hovmöller Diagrams

Because of the relatively large number of experiments to be run (forty-one), it would have been impractical to manually define the properties of North Atlantic Current water for each section and for each experiment, especially if the chosen start times were changed later on. On the other hand, creating

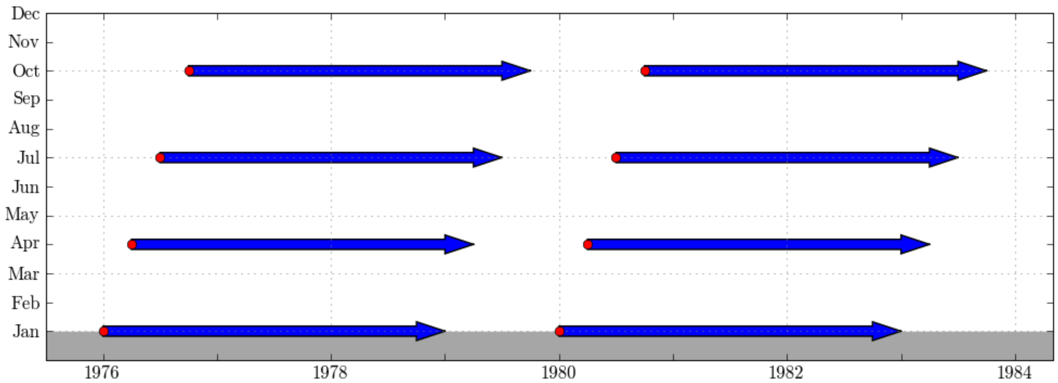

Figure 3.10: Schematic of initialization times and run lengths for Ariane experiments. Particles are initialized in each season, every four years, and are tracked for the three years (36 months) following their start times.

a time-dependent definition would be complicated at best, and probably not worth the effort. A third option was to define a fixed lower limit for temperature and salinity at each inflow strait, making the assumption that inflow from the North Atlantic Current would be the warmest and saltiest water in the area. In order to justify the validity of this decision, I examined Hovmöller diagrams of averaged temperature and salinity in each strait over the entire model record. If mean values stayed relatively constant over the model run, and the distinction between North Atlantic Current and Nordic/Arctic water relatively clear, the fixed-lower-bound method would be acceptable.

Note that these figures were made with depth-averages on the actual model points (the same ones used in section 3.1.2), not the interpolated points used in section 3.1.3, and are, therefore, absolutely true to the model output.

Denmark Strait

Consider first the plots for the Denmark Strait, shown in figure 3.11. The surface averages show clear signatures in both temperature and salinity of

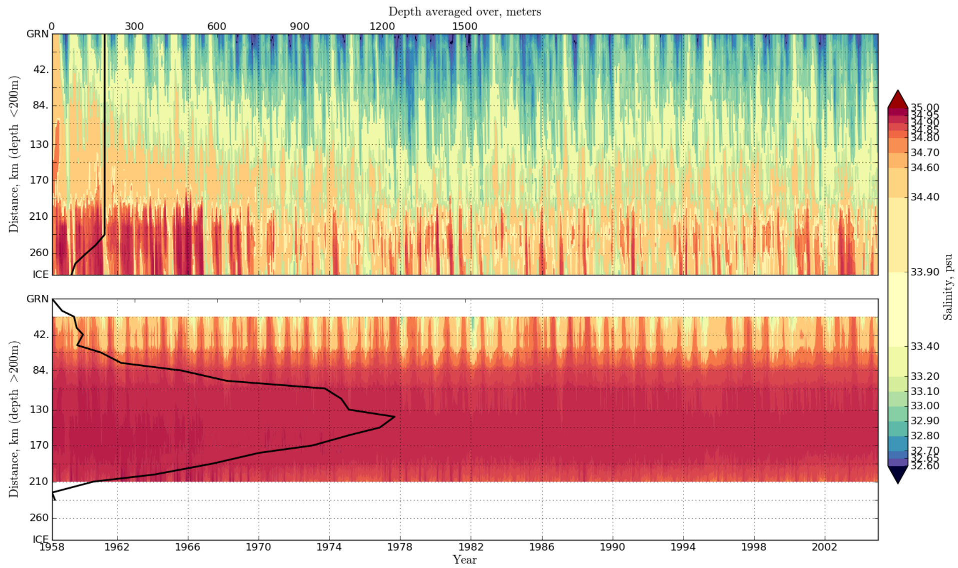

(a) Salinity

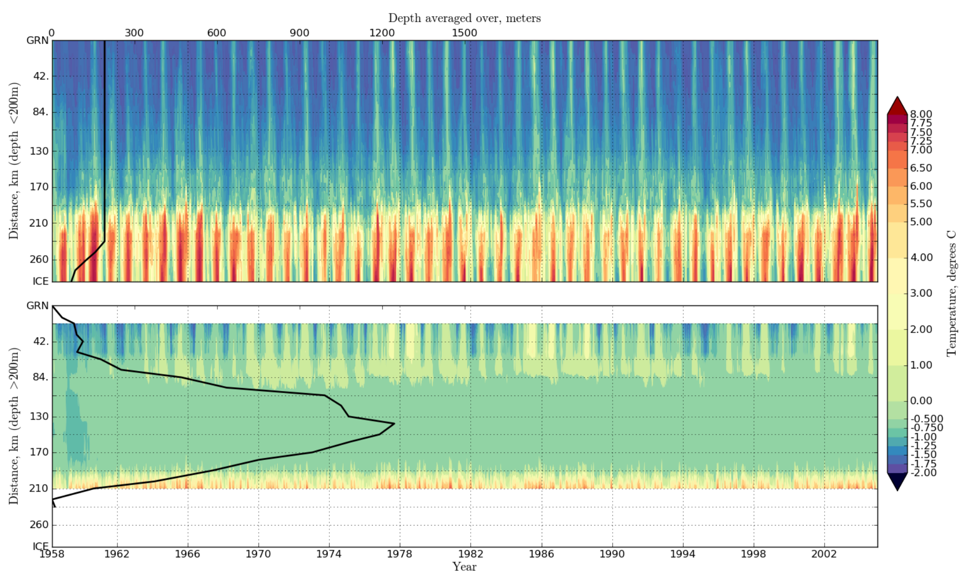

(b) Temperature

Figure 3.11: Hovmöller plots of depth-averaged temperature and salinity in the **Denmark Strait**, 1958-2004. From top to bottom, the plots run from Greenland to Iceland. The upper portion of each subplot is the depth-weighted average from the surface to either 200 meters or the bathymetry, whichever is less. The lower portion is the average from 200 meters to the bathymetry. The thick black line overlayed on the left-hand side of each plot represents the depth averaged over.

two distinct water masses. These masses are the cold and fresh (nominally < 0°C, < 33.0) East Greenland Current to the north, and the relatively warm and salty (nominally > 5°C, > 34.4) North Icelandic Irminger Current further south. Both currents exhibit both short- (seasonal) and long-term (decadal) variations, yet maintain their essential character throughout.

The deep plots of the figure confirm the hypothesis that the North Icelandic Irminger Current stays relatively near the surface. The centre of the strait maintains a steady set of properties – about -0.75 to -0.50°C and 34.85-34.95 – with variability along the edges due to the local currents. The variability along the northern (Greenland) edge of the strait extends at least 100 km into the strait, and is of relatively large magnitude ($\delta D = \pm 1.2$, $\delta T = \pm 2$°C), suggesting that the East Greenland Current is still a significant force even below 200 m. In contrast, the variability along the south (Icelandic) side of the strait, presumably due to the North Icelandic Irminger Current, extends only perhaps 20-30 km into the strait and is of smaller salinity magnitude (~ 0.2). Its temperature magnitude is greater (~ 8°C), but the water being transported here is of much higher temperature compared to the local mean, resulting in relatively greater variations compared to an equal volume of cooler water. This suggests that the North Icelandic Irminger Current mostly remains above 200 m.

Iceland-Faroe Ridge

Next, the surface-layer plots for the Iceland-Faroe Ridge (figure 3.12) show a clear recirculation around the southeastern edge of Iceland, carrying water noticeably colder and fresher than its surroundings (< 5°C vs. ~ 7°C on average; < 34.5 vs. ~ 35 on average). The flow across the rest of the area seems to

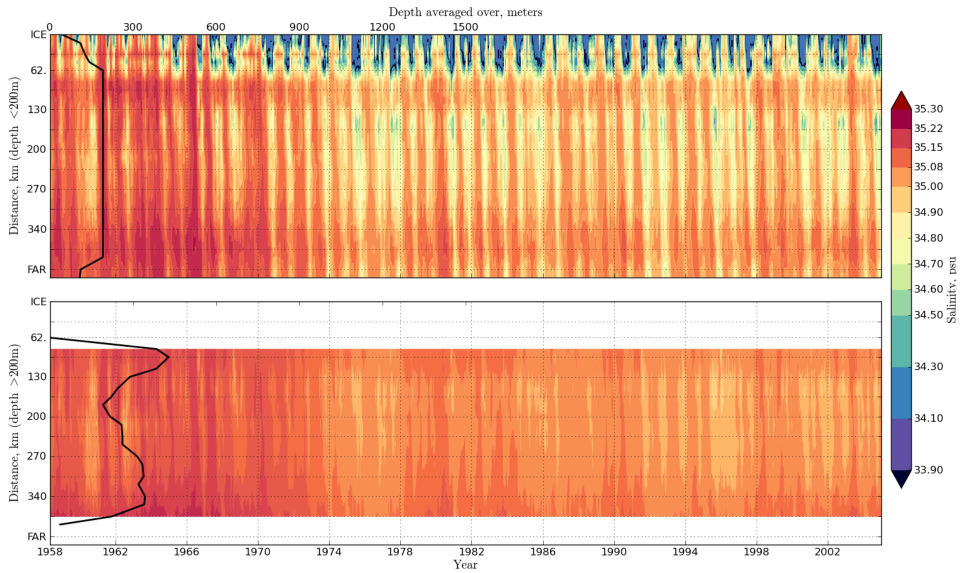

(a) Salinity

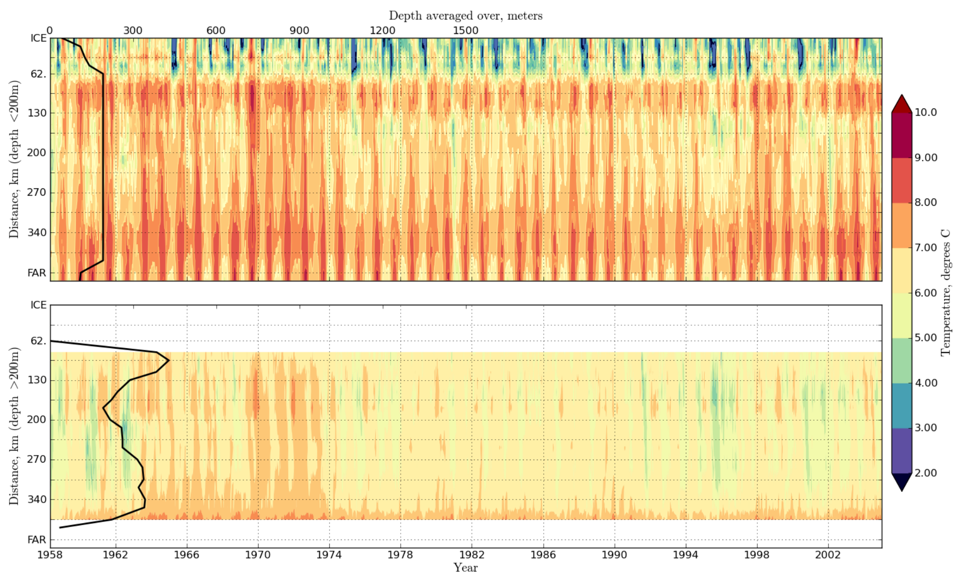

(b) Temperature

Figure 3.12: Hovmöller plots of depth-averaged temperature and salinity over the **Iceland-Faroe Ridge**, 1958-2004. From top to bottom, the plots run from Iceland to the Faroe Islands. The upper portion of each subplot is the depth-weighted average from the surface to either 200 meters or the bathymetry, whichever is less. The lower portion is the average from 200 meters to the bathymetry. The thick black line overlayed on the left-hand side of each plot represents the depth averaged over.

be relatively even, with small rises in temperature and salinity in the vicinity of shelf breaks (70-120 km, 340-420 km). Overall, a strong seasonal signal is present. The vastly more salty ($> \sim 35$) period from 1958-1972 is likely associated with a known high-salinity period in the North Atlantic at that time (Reverdin et al., 1997).

The deeper layer shows similar cross-strait structure compared to the top 200 m, though with the notable absence of a North Icelandic Irminger Current, suggesting that recirculation remains near the surface. It is interesting to note the relative stability in properties here, however – both temperature and salinity remain in relatively narrow ranges ($5 - 8$°C, $34.9 - 35.15$ (post-1972), respectively). This lack of variability suggests that much of the transport occurs near the surface.

Faroe-Shetland Channel

Finally, consider the Faroe-Shetland Channel plots shown in figure 3.13. The temperature in the surface layer tends to be high at all points in the strait, rarely dropping much below 7°C, and is very seasonal. The southern end of the strait tends to be slightly warmer (as a result of the inflowing North Atlantic Current) than the north, however, where there is water exiting the Nordic region through a recirculation around the Faroe Islands. Further evidence of these patterns may be found in the salinity plot, where the northern end of the strait is noticeably fresher (as low as ~ 34.9 for timescales of a season or so) than the south (salinities may reach the same absolute values there, but over much smaller space and time extents). Also, there is here again a period of noticeably higher salinity from 1958-1972, dropping from a mid-strait average

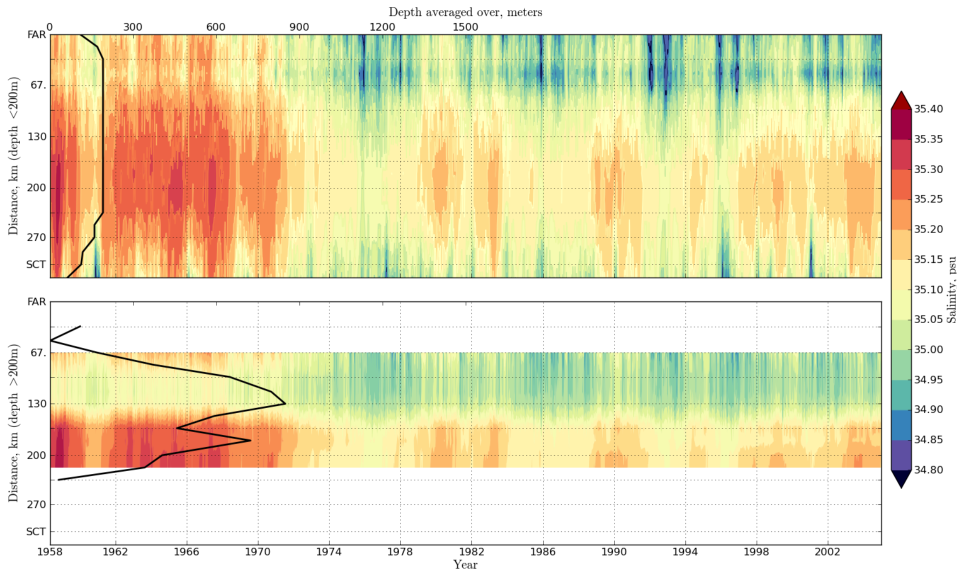

(a) Salinity

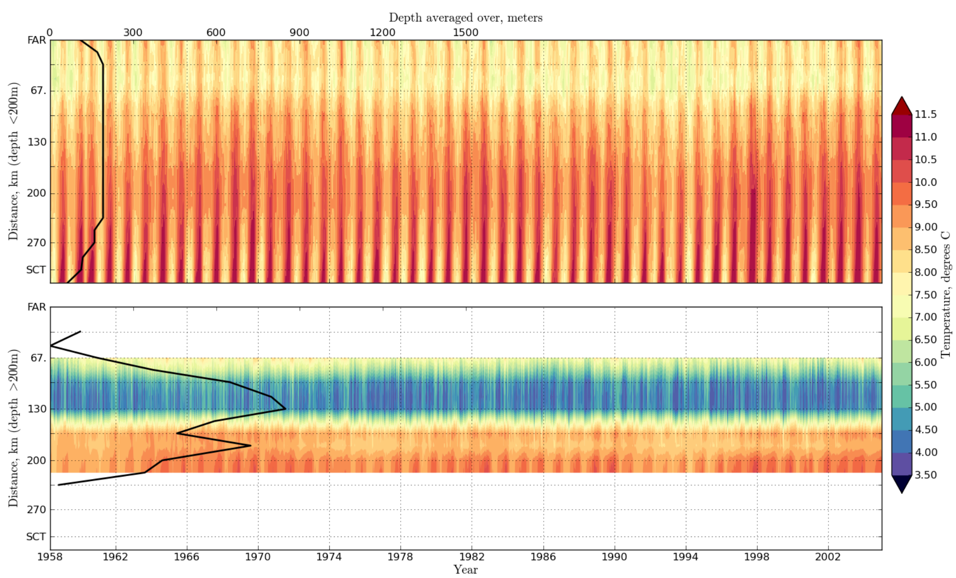

(b) Temperature

Figure 3.13: Hovmöller plots of depth-averaged temperature and salinity in **Faroe-Shetland Channel**, 1958-2004. From top to bottom, the plots run from the Faroe Islands to Scotland. The upper portion of each subplot is the depth-weighted average from the surface to either 200 meters or the bathymetry, whichever is less. The lower portion is the average from 200 meters to the bathymetry. The thick black line overlayed on the left-hand side of each plot represents the depth averaged over.

of around 35.3 to around 35.1 in later years, and a more noticeable decadal signal than in the other two straits.

At deeper levels, a curious effect is apparent in the distinct separation of differing values in both temperature and salinity. The FSC along this section has two main fractures, with a deeper path to the north and a shallower one to the south. Water in the northern valley tends to be quite cold and rather fresh (< 6°C, < 35.05) compared to its southern counterpart (> 9°C, > 35.10). This suggests an inflowing North Atlantic Current component to the south which extends rather deep (ie. well below 200 m), and a strong overflow path predominantly through the northern channel.

Overall

In all straits, inflowing water of North Atlantic Current origin is noticeably warmer and saltier than its surroundings – more so in the FSC, less so in the DS. Variability is strong on annual timescales, with some areas also exhibiting decadal changes. However, excepting higher salinities in all areas prior to 1972 associated with a known high-salinity period in the North Atlantic (Reverdin et al., 1997), there is no long-term trend of note. In most cases the North Atlantic Current water remains warmer and saltier than its surroundings, with even its minimum values being only slightly less than the maximum values of these surroundings. Therefore, even though defining a fixed lower bound on temperature and salt is by no means ideal, or even "good" (especially prior to 1972), it can be taken as an "approximation of the truth", and will likely lead to a majority of particles being inserted in the North Atlantic Current. In fact, it will be seen in section 3.3.2 that nearly all particles are part of the inflowing waters (see in particular figures 3.17c and d, showing the minority of "captured" particles which were misplaced, and figure 3.15, showing the low probability of particles being placed in outflow rather than inflow).

3.2.3 Initial Particle Positions

Based on these diagrams, I am confident that, while not ideal, defining North Atlantic Current water using an appropriate, fixed lower bound on both temperature and salinity is not unreasonable. The definitions I chose are shown in table 3.4. In making these choices, I erred on the side of caution – I would rather miss some part of the inflow than place particles in the outflow.

Hansen et al. (2003) shows S= 35.15 and T= 7°C for IFR water northeast of the Faroe Islands, while Rudels et al. (1999) gives figures of 35.1 and 6°C for DS water. The model, then, appears to be too fresh, but represents temperature reasonably well.

Section	**Min. salinity**	**Min. temperature (°C)**
Denmark Strait (DS)	34.12	2.70
Iceland-Faroe Ridge (IFR)	34.80	7.50
Faroe-Shetland Channel (FSC)	35.10	8.00

Table 3.4: Criteria for North Atlantic water in each of the three entrance straits. The third criterion for all straits is that velocity must be *into* the Nordic Seas.

Once the points in each section which met this criteria were found, around 2300 virtual particles were inserted in their vicinity. Because of the initialization algorithm I used, initializing a more precise number of particles was not possible. Fortunately, for my study the absolute number of particles is not of the utmost importance, so long as it is not too low. By too low, I mean that certain parts of the inflow may be represented by only one or two particles, or that certain parts of the current are over- or under-represented. By having a large enough number of particles, I hope to ensure that I both represent all parts of the current well, and capture all possible paths taken by the currents. Eighty percent of the particles were distributed randomly at a distance of up to half a grid index both horizontally and vertically from all included points – the depth of each cell was taken into account here, ensuring that the particle density was the same at all levels. The remaining twenty percent were placed in a 3D Gaussian distribution about the included grid point with the highest to-Nordic-Seas velocity in an effort to concentrate them near the current's core. A sample distribution of points for each section is shown in figure 3.14.

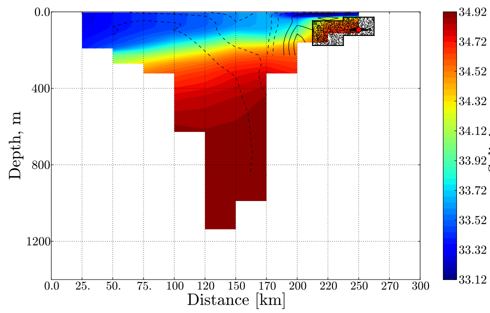

(a) Denmark Strait

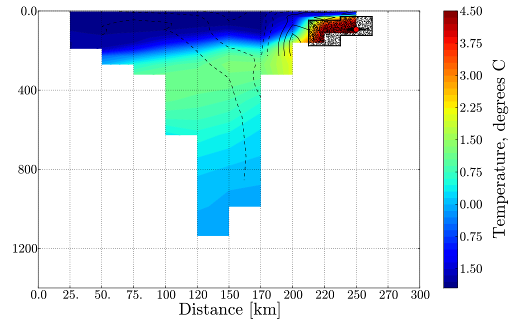

(b) Denmark Strait

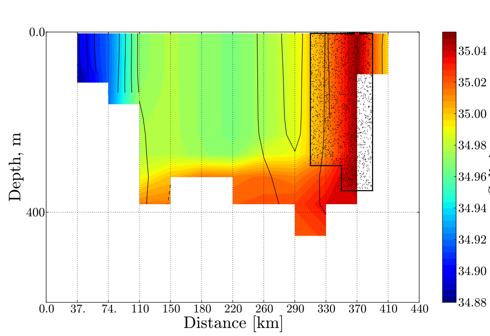

(c) Iceland-Faroe Ridge - salinity

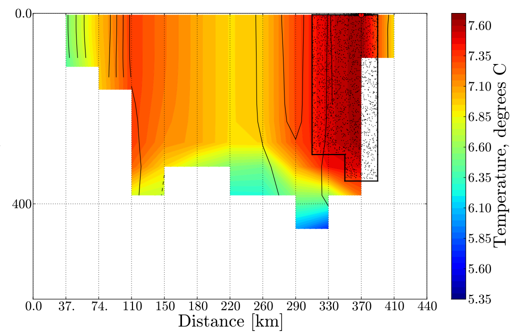

(d) Iceland-Faroe Ridge - temperature

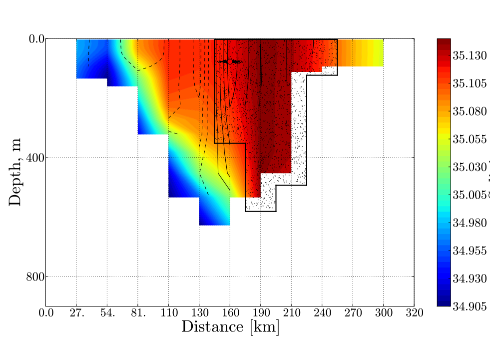

(e) Faroe-Shetland Channel - salinity

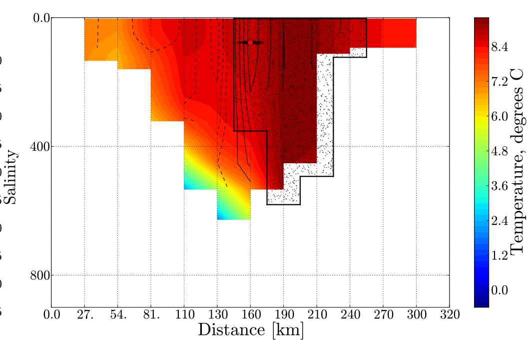

(f) Faroe-Shetland Channel - temperature

Figure 3.14: Sample distribution area for virtual particles in each entrance strait. The thick black line encloses all points defined as North Atlantic Current water, similar to in figures 3.6 to 3.8, while the small black dots represent the particles. This particular distribution is for the October 1984 experiment. Velocity contours appear at ±(5, 10, 15, 20, 30) cm/s. Solid velocity lines are into the GIN seas; dotted lines are from them.

3.3 Results

3.3.1 General Particle Tracks

The Lagrangian paths for particles released in October 1984 are shown in figure 3.15 – this experiment coincides with the average sea state discussed and shown earlier in figures 3.1 and 3.2. These tracks are fairly representative of all months and years in their general characteristics.

Particles started in the Denmark Strait follow two major pathways. The dominant one is to flow southeast and join the Norwegian Coastal Current, subsequently turning northward. A few particles spill across the Barents Sill into that sea, but most continue north into the Arctic. The second, less important, path is to circulate around the Iceland Sea, subsequently either recirculating into the North Icelandic Irminger Current and joining the first path, or exiting through the Denmark Strait.

Particles initialized over the Iceland-Faroe Ridge also follow two main paths. The less important one has them leaking back through the Faroe-Shetland Channel after passing the Faroe Islands, joining the the water already flowing along the Atlantic face of the Greenland-Scotland Ridge. The particles then either continue on with the North Atlantic Current water or, because they are in the water closest to the ridge, recirculate back through the IFR. The second, and more dominant, pathway is the same as for the DS, wherein particles join the northward-flowing Norwegian Coastal Current after passing the FSC. More of these leak into the Barents Sea compared to the DS particles, but again, most flow into the Arctic through Fram Strait. A very few continue all the way around into the East Greenland Current and either

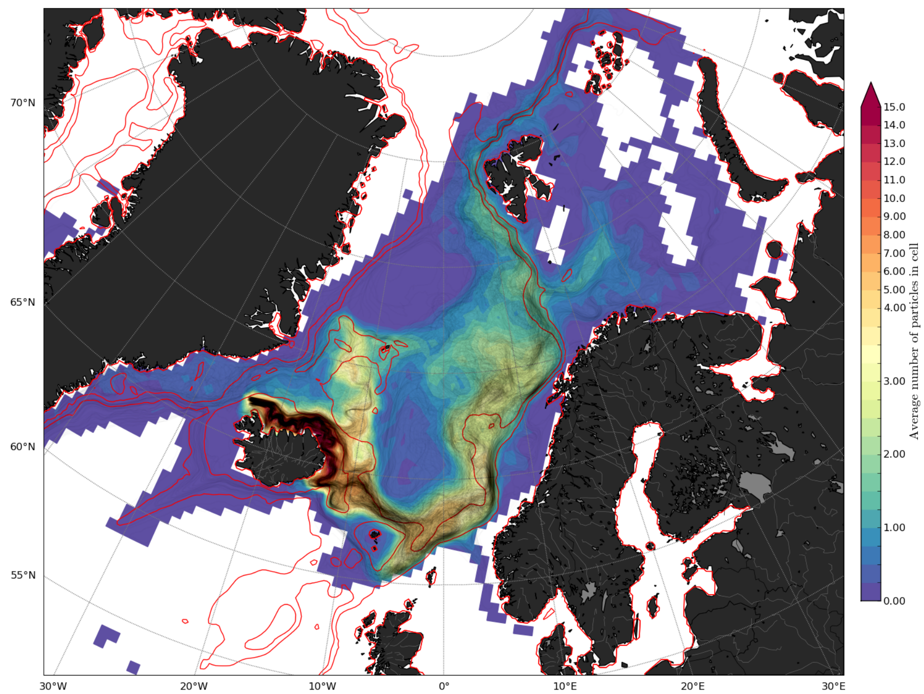

(a) Denmark Strait start

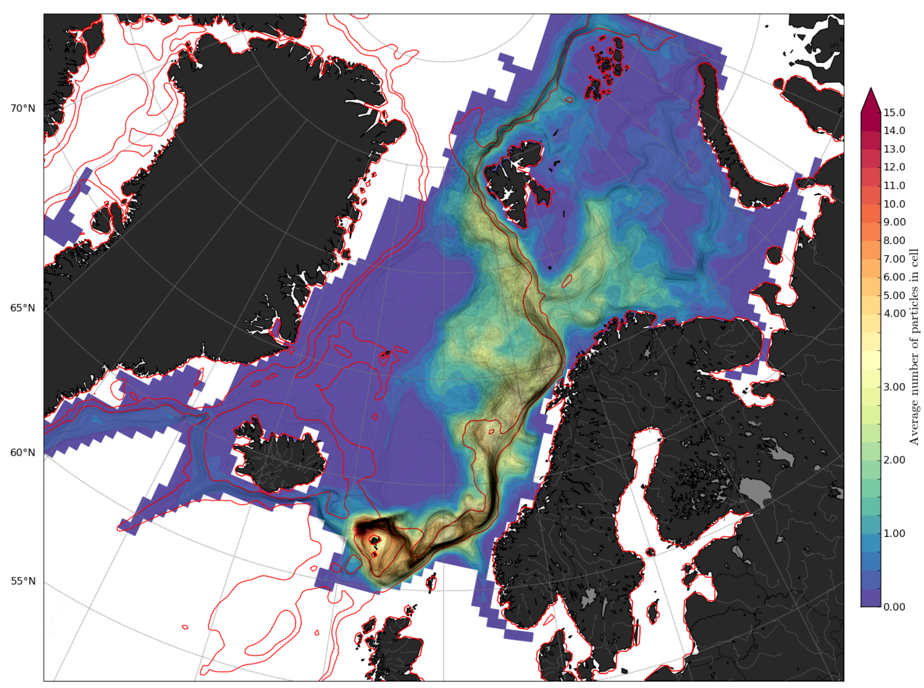

(b) Iceland-Faroe Ridge start

Figure 3.15: Continued on page 88

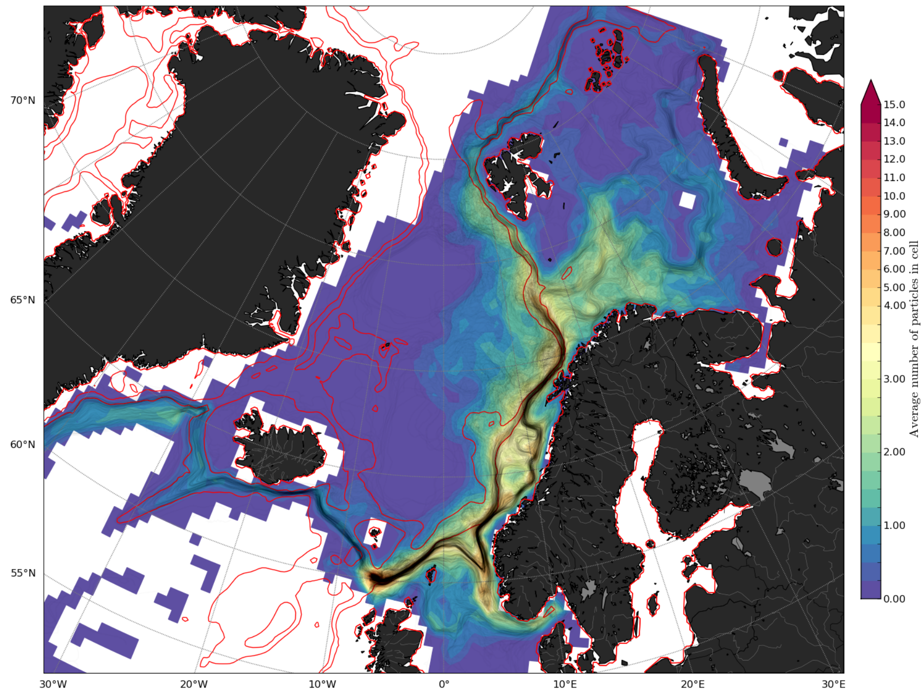

(c) Faroe-Shetland Channel start

Figure 3.15: Continued from page 87. Track lines for all particles in the three-year period following October 1984. A new model grid was created by retaining every third point in the original. This new grid was then used to find the average horizontal particle density over the course of the thirty-six month run, which forms the colour scale. The 500 m and 1500 m isobaths are shown in red. Plot for the Faroe-Shetland Channel is shown on the next page.

circulate in the Greenland Sea gyre or exit through the Denmark Strait.

Particles which begin in the FSC also mostly join the Norwegian Coastal Current. Even more of them flow into the Barents sea compared to the IFR particles, since they are in the part of the current closest to the Barents shelf, but again most of them flow through Fram Strait with an exceptional few joining the East Greenland Current. The secondary path for FSC particles is to flow a short way in to the southernmost part of the Norwegian Sea, sink, and then exit again through the FSC.

Based on these plots, and the velocity fields in figures 3.1 and 3.2, I am confident that the model has produced reasonable flow fields and that the Ariane tracker is working properly. Therefore, I continue by viewing only those tracks produced by particles which overflow within the three-year timespan of each experiment.

3.3.2 Overflow Particle Tracks

As outlined earlier, exchanges between the Atlantic and Nordic regions occur mainly across three straits, with each strait having possible inflow (into the Nordic Seas) and outflow (into the Atlantic) components. This means that North Atlantic Current water in any particular strait which eventually flows back into the Atlantic (within the three-year period of my experiments) can take three possible routes. Therefore, nine individual routes must be analysed for each experiment, one for each inflow/outflow pairing.

To do this, I defined a set of boxes for each strait. Particles must pass through certain of these boxes below a specified depth in order to be classified as deep water – consistent with my earlier discussion, 200 meters was chosen as this minimum depth for all straits – and is not allowed to pass through the others. Particles which met these requirements for each inflow/outflow strait pair were deemed to have overflowed, and their paths plotted in figures 3.16 to 3.18.

Early work on this system demonstrated that nearly all particles which "overflowed" according to it entered the deep limb of the East Greenland Current, skirting the coasts of Greenland. Therefore, to ensure that I only captured deep (or at least non-surface) water, another box was positioned north of Cape Farewell with a minimum pass-through depth of 300 meters. In fact, we will see in section 3.3.3 that, on average, the captured particles double their depth between overflow and a point 750 km downstream, so the change in minimum depth from 200 m to 300 m does not seem unreasonable (the Greenland box is about 780 km in a straight line from the Denmark Strait, and is considerably farther from the other two).

Two complications arose during this analysis. First, many of the particles existing near the Iceland-Scotland Ridge tend to flow around the Faroe Islands, forming a local gyre. Unfortunately, that land mass is where I have chosen to separate the Iceland-Faroe Ridge virtual section from the Faroe-Shetland Channel virtual section. Therefore, when trying to detect particles in the one strait, but not the other, these particles are likely excluded. However, the number of these particles, compared to the total which overflow, is quite small – perhaps five to ten percent for IFR overflows, and less than one percent for FSC overflows. Therefore, excluding them is unlikely to significantly impact my overall results. I have tried to limit the problem in the IFR overflow case by allowing the particles to pass through the FSC if they are no deeper than 150 meters. In practice, doing so produces results nearly identical to those if the FSC is completely blocked.

The second complication stems from the fact that particle positions were output from Ariane only every three days. This means that, in exceptional circumstances, particles may have travelled a considerable distance between outputs. For example, if the average current speed is 10 cm/s, the particle will have moved 26 km in three days; if the current is 28.9 cm/s, it may have travelled 75 km. Therefore, if a detection box is too narrow, a particle may simply skip across it without being detected. Since the average speed of most particles is around 8 cm/s, this did not present a problem in most cases – I just ensured that all boxes were at least 75 km across, which guaranteed detection in all but highly unusual cases. However, just south of the Faroe Islands, there is an outflow jet in the model which may produce local velocities of 40, or even 50, cm/s (consistent with the previously mentioned observations of Hansen et al. (2001)). At the same time, these particles would flow through the narrowest part of the detection box for the FSC-FSC strait pair. This presented some difficulty since one side of the box could not be moved much further north or west (it would interfere with the IFR), and the other side could not be moved further east (it would interfere with the initial positions of the particles). Therefore, it is inevitable that some of these particles (perhaps 100-200) were not detected – an insignificant number compared to the 5000+ which were.

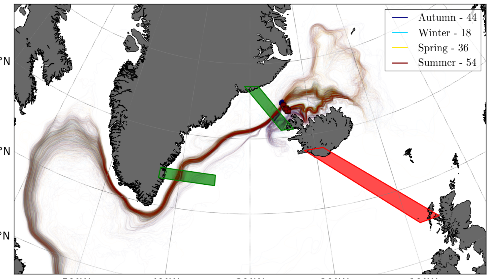

(a) Exit through the Denmark Strait (seasonal colouring). 1552 particles total.

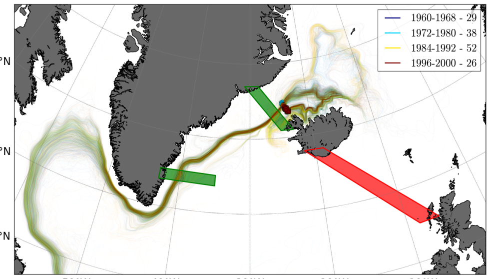

(b) Exit through the Denmark Strait (decadal colouring). 1552 particles total.

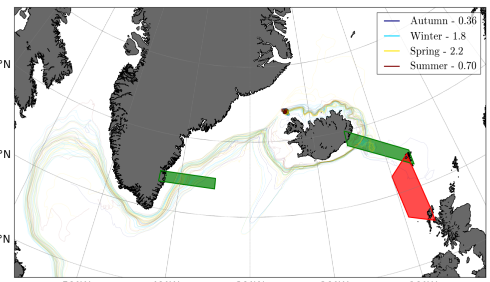

(c) Exit over the Iceland-Faroe Ridge (seasonal colouring). 51 particles total.

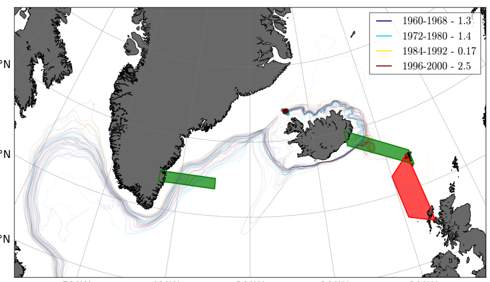

(d) Exit over the Iceland-Faroe Ridge (decadal colouring). 51 particles total.

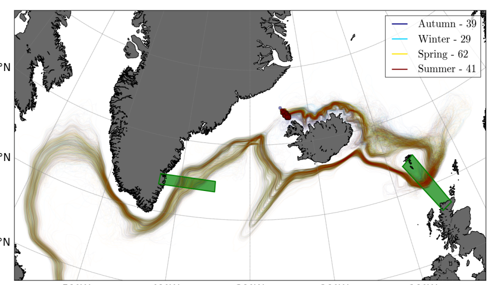

(e) Exit through the Faroe-Shetland Channel (seasonal colouring). 1744 particles total.

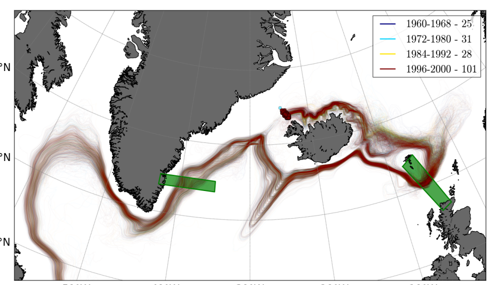

(f) Exit through the Faroe-Shetland Channel (decadal colouring). 1744 particles total.

Figure 3.16: Paths of all particles which are initialized in the **Denmark Strait**, and exit as deep water. Particles must pass through the green box near the southern end of Greenland at 300 m or deeper, and through the other green boxes at 200 m or deeper. They may not pass through the red box at all in (a) and (b), and no deeper than 150 m in (c) and (d). Coloured dots represent start locations for particles, using the same colouring as the lines in each plot. Numbers in legend represent number of particles per insertion to be captured as outflow.

Denmark Strait Inflow

Let us first discuss the paths of particles captured after being initialized in the Denmark Strait, shown in figure 3.16. One of the first things noticed is that very few of the total number of particles initialized actually overflow – only 3347 of 79373, or 4.2%. Of these, 46.4% return back through the Denmark Strait, 52.1% flow through the Faroe-Shetland Channel, and a mere 1.5% cross over the Iceland-Faroe Ridge. Upon examining the other inflow straits, we will observe a similar pattern in that the FSC consistently exports the most particles, and the IFR very few.

There are clearly two routes followed by the overflowing particles shown in figures 3.16a and (b). Both paths initially follow the North Icelandic Irminger Current around the north side of Iceland, then are shed off and are picked up in countercurrents returning to the Denmark Strait. The more dominant of these currents flows more or less directly west, while the other takes the particles in a single orbit of the Icelandic basin. Both routes merge together as they exit the Nordic area, becoming a part of the East Greenland Current. The longer, circum-basin route extends for 2000 km or more and takes six months or greater to complete. The more dominant southern route is only about 1000 km long, and takes as little as 2-3 months to complete.

The latter route is taken with equal preference regardless of which season or decade a given experiment was begun. However, the more northern circulation seems to be taken significantly less frequently in recent (1996-2004) years compared to the 1970's and 1980's. The most particles (52/insertion) joined the outflow when they were inserted in July (and so exited sometime in the fall), while January insertions outflowed the least (26/insertion).

Very few particles starting in the DS flowed over the Iceland-Faroe Ridge, as shown in figures 3.16c and (d). Those that did tended to stay in the North Icelandic Irminger Current before exiting over the northernmost channel in the IFR. This lack of outflow may be due to two reasons: one, the strait is mainly an importer of water; and two, it is relatively shallow, and therefore does not allow much of the deep water to overflow regardless of its sources. Any water that does pass through it follows a fairly rigid path 800-1000 km in length, and does so in 6-8 months. There does not appear to be any preference in either season nor decade.

In contrast to the previous two entrance/exit combinations, where particles followed a well-defined path from inflow to outflow, particles exiting through the Faroe-Shetland Channel (shown in figures 3.16e and (f)) tend to fill well-defined areas instead. These areas do not depend on month or decade of initialization. After rounding Iceland as part of the North Icelandic Irminger Current, the particles break off to cool and sink on the Nordic side of the Greenland-Scotland Ridge. A minority, presumably still near the surface when passing abeam the FSC, continue on in the direction of the Norwegian Coastal Current before spinning off, cooling, and sinking. The eddy-driven nature of this process is borne out by the distribution in travel times, shown in figure 3.20a, in that there is no definitive spike in the distribution. Instead, particles begin to arrive after about six months of travelling, with their numbers peaking after about a year. After two years, most particles have exited. The FSC is the main overflow strait for Denmark Strait inflow, counting for over half of the total. This route was followed most by particles inserted in spring (62/insertion) as opposed to winter (29/insertion), and was followed much more in the 1996-2000 period than in any other decade (101/insertion, vs. 28/insertion on average for the other periods). The North Atlantic Oscillation shifted suddenly from positive to negative index in 1996 (Hurrell & Deser, 2009), which according to Taylor & Stephens (1998) would cause the North Atlantic Current to shift southward with a lag of several years. After this North Atlantic Oscillation event, the index returned to a (weakened) positive state for the rest of the decade, presumeably moving the North Atlantic Current back to the north. The oscillation in the main current feeding the Nordic Seas import from the Atlantic may therefore play a role in this anomaly.

Iceland-Faroe Ridge Inflow

Next consider the particles initialized over the Iceland-Faroe Ridge, plots of which are shown in figure 3.17. Here again, only a minority of particles exit as deep water – a mere 4878 of a possible 86991 (5.6%) over the fifty-year model run. Fully 98.3% of those exit through the Faroe-Shetland Channel, with only 1.1% flowing back over the IFR and an insignificant 0.6% going through the DS.

Flow from the IFR to the DS is sporadic at best, with particles choosing one of two paths. Those entering on the northern side of the ridge tend to circulate the Icelandic Sea, joining the East Greenland Current outflow after a relatively short journey of 2000-3000 km. Those entering on the south side tend to circulate for 5000-7000 km around the entire Nordic region, travelling north to Fram Strait with the Norwegian Coastal Current and south with the East Greenland Current. Interestingly, both routes take a similar amount of time, $2 - 2\frac{1}{2}$ years.

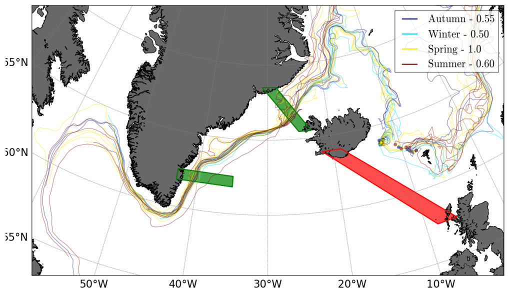

(a) Exit through the Denmark Strait (seasonal colouring). 27 particles total.

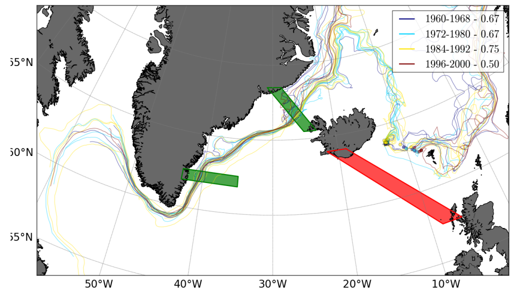

(b) Exit through the Denmark Strait (decadal colouring). 27 particles total.

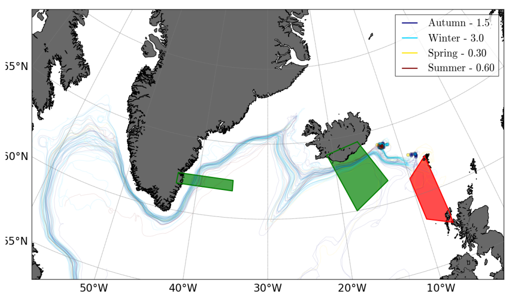

(c) Exit back over the Iceland-Faroe Ridge (seasonal colouring). 56 particles total.

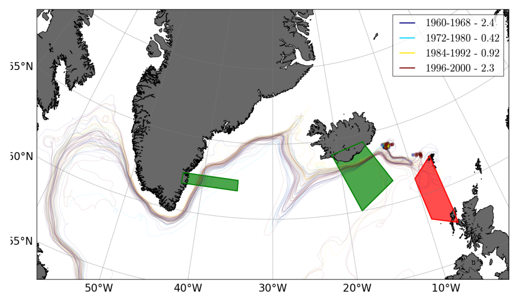

(d) Exit back over the Iceland-Faroe Ridge (decadal colouring). 56 particles total.

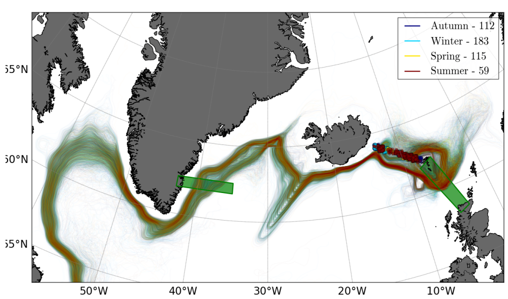

(e) Exit through the Faroe-Shetland Channel (seasonal colouring). 4795 particles total.

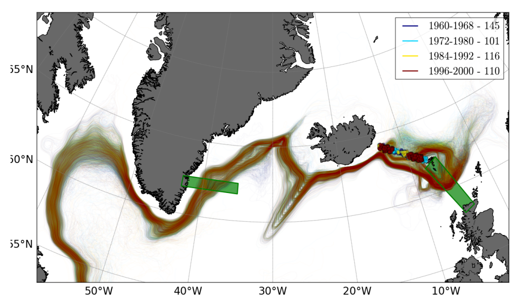

(f) Exit through the Faroe-Shetland Channel (decadal colouring). 4795 particles total.

Figure 3.17: Paths of all particles which are initialized over the **Iceland-Faroe Ridge**, and exit as deep water. Particles must pass through the green box near the southern end of Greenland at 300 m or deeper, and through the other green boxes at 200 m or deeper. They may not pass through the red box at all in (a) and (b), and no deeper than 150 m in (c) and (d). Coloured dots represent start locations for particles, using the same colouring as the lines in each plot. Numbers in legend represent number of particles per insertion to be captured as outflow.

Flow exiting back over the IFR does not appear to be actual overflow water. Instead, the particles seem to have been placed randomly in areas where the water is already dense and exiting the Nordic area, and simply join the outflow. This is not really surprising, considering the undersampling of velocities and properties in my particle initialization algorithm. In fact, it is actually somewhat encouraging to see that so few particles were poorly placed in this manner – mostly in fall and winter. In any case, none of the flow over this ridge appears to have entered the Nordic region via the IFR.

The majority of overflowing IFR particles travel through the Faroe-Shetland Channel. To get there, they tend to follow relatively well-defined paths directly between the IFR and FSC, with a few exhibiting eddy-like tendencies to the north and east of the IFR (possibly even travelling with the Norwegian Coastal Current for a short while), before sinking and joining the deep outflows. Their numbers are comparable in all decades, hovering at about 110 per insertion. The outflow is highly seasonal, however, with 183/insertion for winter starts versus only 59/insertion for summer starts. This is likely due to enhanced export through the FSC in summer, corresponding to the six-month average travel time of outflowing particles. During this time, the particles move fairly slowly, covering 500-1000 km.

Faroe-Shetland Channel Inflow

Finally we come to those particles initialized in the Faroe-Shetland Channel, whose tracks are shown in figure 3.18. The odd, handle-like shape of the easternmost box was, as alluded to previously, necessary to avoid the area where the particles were inserted while simultaneously not interfering with the IFR

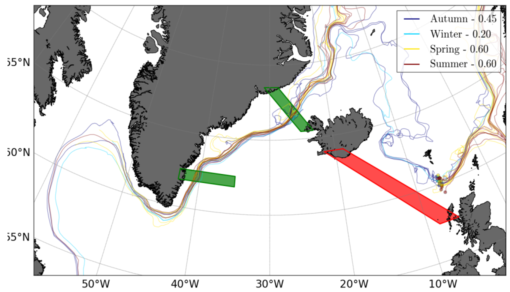

(a) Exit through the Denmark Strait (seasonal colouring). 19 particles total.

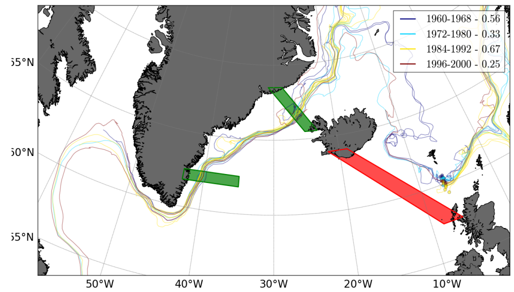

(b) Exit through the Denmark Strait (decadal colouring). 19 particles total.

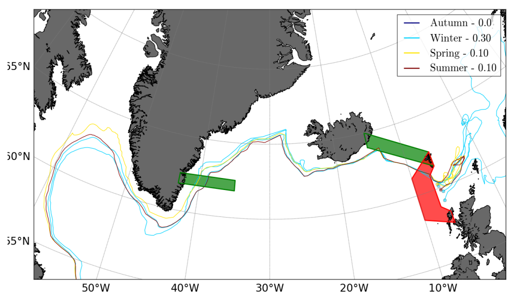

(c) Exit over the Iceland-Faroe Ridge (seasonal colouring). 5 particles total.

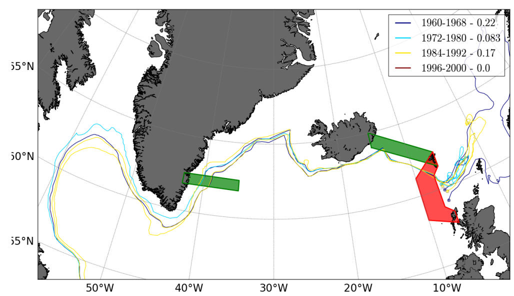

(d) Exit over the Iceland-Faroe Ridge (decadal colouring). 5 particles total.

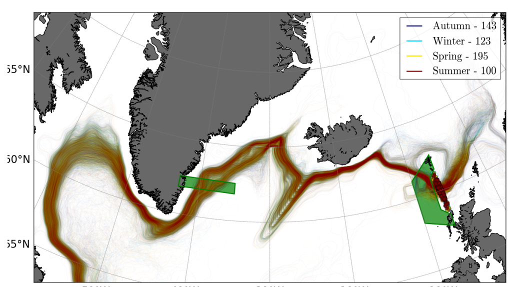

(e) Exit through the Faroe-Shetland Channel (seasonal colouring). 5755 particles total.

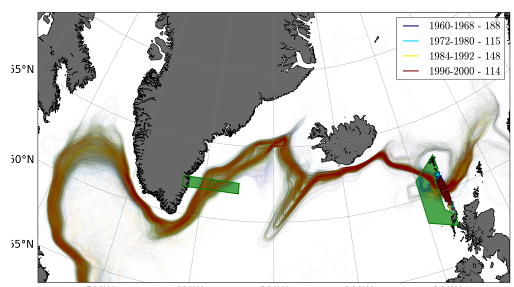

(f) Exit through the Faroe-Shetland Channel (decadal colouring). 5755 particles total.

Figure 3.18: Paths of all particles which are initialized in the **Faroe-Shetland Channel**, and exit as deep water. Particles must pass through the green box near the southern end of Greenland at 300 m or deeper, and through the other green boxes at 200 m or deeper. They may not pass through the red box at all in (a) and (b), and no deeper than 150 m in (c) and (d). Coloured dots represent start locations for particles, using the same colouring as the lines in each plot. Numbers in legend represent number of particles per insertion to be captured as outflow.

region. Of 73426 particles which started here, 5779 (7.9%) actually overflowed – the highest percentage of the three entrance straits. Of these overflowing particles, nearly all (99.6%) exited back through the FSC itself.

In doing so, they again follow the paths first seen on the DS-FSC route, but here tend to do more of their cooling on the south side of the Norwegian Coastal Current, rather than to the northeast of the IFR. The most particles (195/insertion) are exported 2-3 months after being inserted in April, again corresponding with the peak FSC outflow season of summer. The fewest particles (100/insertion) were exported after a July insertion. The particles travel 300-1000 km during their round trip back to the FSC.

Those few which exit over the DS really fall into two groups. Four of the 19 actually are washed back out of the strait upon insertion, for the same reasons discussed previously in section 3.3.2. These then cross the IFR before circling the Icelandic sea – therefore, they are not actually from the FSC at all. The remainder follow the expected path around the rim of the GIN seas, first flowing with the Norwegian Coastal Current to Fram Strait, then with the East Greenland Current back to the DS. This journey of 5000-5500 km takes a little over two years, with an average velocity of about 7 cm/s.

Similarly, in reality *none* of the particles actually exited over the IFR. Instead, they speed through the exclusion box in the manner discussed at the beginning of this section, or pass through it above the allowed 150 m depth. They then dogleg north just enough to enter the box over the IFR and get detected. Therefore, I can say that *no* particles entering through the FSC exit over the IFR.

	DS	IFR	FSC	Total
DS	1552 **46.4%**	51 **1.5%**	1744 **52.1%**	3347 **4.2%**
IFR	27 **0.6%**	56 **1.1%**	4795 **98.3%**	4878 **5.6%**
FSC	19 **0.3%**	5 **0.1%**	5755 **99.6%**	5779 **7.9%**
Total	1598 **11.4%**	112 **0.8%**	12294 **87.8%**	13794 **5.6%**

Table 3.5: Summary of outflows. Rows are the inflow straits; columns are outflow straits. Integers represent the absolute number of particles following each inflow/outflow pair. Percentages for each pair represent the fraction of all overflowing particles from that entrance strait which used that route. Percentages in the "Total" column are the fraction of particles inserted in each strait to overflow; percentages in the "Total" row are the fraction of all overflowing particles to exit through that strait. The "Total/Total" box shows the number of all particles which overflowed, with a percentage relative to the total number of particles initialized.

Comparison

Of the three straits, it is clear that the Faroe-Shetland Channel is the most important in terms of outflow, accounting for fully 87.8% of the total (see table 3.5 for the numbers discussed here). It is fed by all three straits, but mostly by the two southern ones (14% from the DS, 39% from the IFR, and 47% from the FSC itself). In contrast, the Denmark Strait contributes only 11.4% to the total export, and is fed almost entirely by itself (97%).

Meanwhile, the Iceland-Faroe Ridge exports essentially no particles. The only particles which *do* pass over the Ridge come from the Denmark Strait, flowing through the deeper northwestern rift in the sill. This is likely for two reasons: first, the relatively shallow maximum depth of the sill, and second, the local flow characteristics along the Nordic side of the ridge. These are usually quite strong, and are directed toward the southeast and the FSC. Therefore, any particles originating over the IFR will be swept downstream into the FSC by the time they are ready to exit the GIN seas. This same reasoning would explain why no particles from the FSC cross the IFR either – any that travel far enough west to do so would be quickly swept back towards the FSC by the current. The reason some particles from the DS *can* cross is because they stay on the southern side of the North Icelandic Irminger Current until meeting the inflowing IFR water, and so do not have to cross a band of prevailing currents to make the exit.

In terms of inflow importance, it is clear that the two southern straits are the most critical, feeding a combined 77% of the total overflow. The Denmark Strait is comparatively less important since it imports less water, with that water which is imported tending to stay nearer the GIN Seas interior than that from the IFR and FSC, limiting its opportunities to cross the Greenland-Scotland Ridge.

It should also be noted how few particles actually exit back through these straits – only 5.6% of the total inserted over all years and all seasons. Most of the inserted particles flow up the Norwegian coast and either enter the Arctic through Fram Strait, or the Barents Sea across the Barents Shelf. After a typical three-year Ariane experiment, perhaps only half of the particles inserted in the Denmark Strait remain in the GIN seas, mainly in the Iceland Sea and the northern Norwegian Sea. Around 20% of the IFR and FSC-initialized particles remain in the northern Norwegian Sea as well. This may be seen in figure 3.19, showing the final positions of each particle after three experiments from different decades were run. It is interesting to note in that same figure that there are very few particles in the center of the main gyres (the Greenland Sea and over the Norwegian Sea).

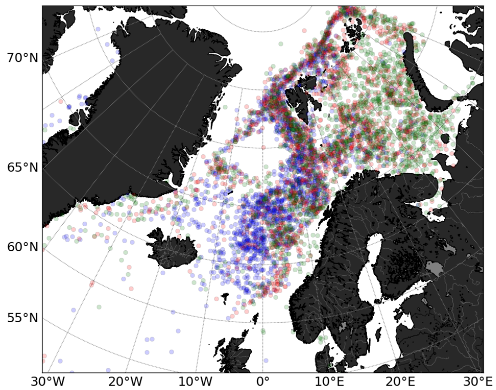

(a) October 1964

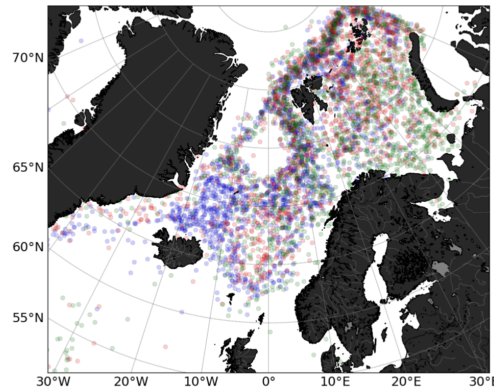

(b) April 1980

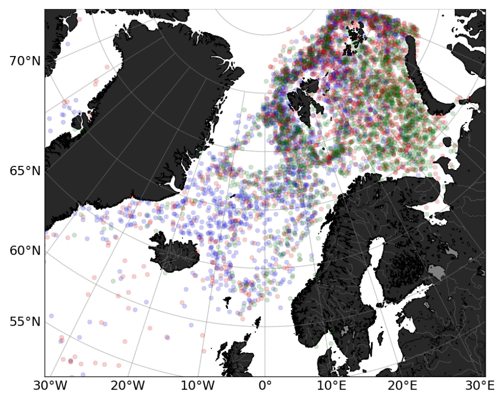

(c) October 1996

Figure 3.19: Positions of all particles at the conclusion of selected experiments. Blue dots came from the Denmark Strait, red from the IFR, and green from the FSC. The GIN Seas region as discussed in the text is defined as 30°W – 20°E longitude, 60°N – 80°N latitude.

Travel times and distances to the overflow boxes are shown for the various strait pairs in figure 3.20a. The four interesting strait pairs are the DS-DS (upper left histograms), and all the FSC outflows (the right-hand column of histograms). Notice that all of these pairs in the distance plots have prominent peak values, suggesting a definite path that must be followed. In fact, the DS-DS distance plot could be said to have two peaks, one for each of the two major routes seen in figures 3.16a and (b). The time plots are similar, suggesting that particles tend to flow at a set velocity along these paths. The exception is the DS-DS time plot, which is spread out rather uniformly. This suggests that the flows along this route are more eddy-driven, following less of a straight line.

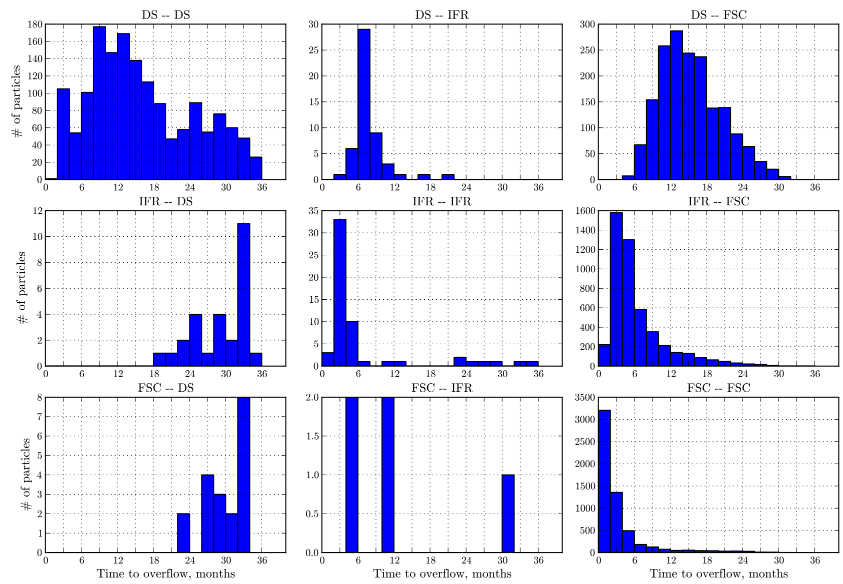

(a) Travel times to overflow box

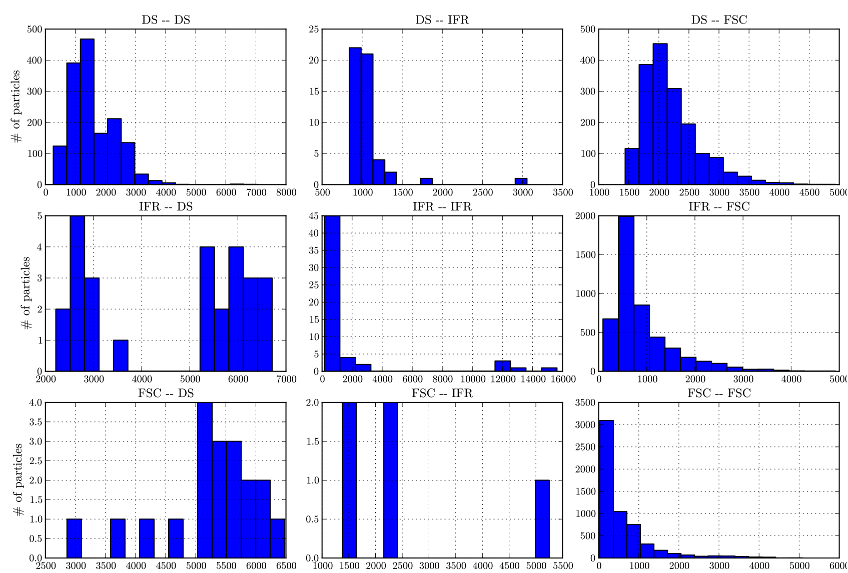

(b) Travel distances to overflow box

Figure 3.20: Travel times and distances for all inflow-outflow strait pairings from start to overflow.

However, when one calculates the average velocities on a per-particle basis, one produces the histogram shown in figure 3.21. Here it is clear that all four of the major straits enjoy a similar, fairly wide velocity distribution with a distinct peak. In fact, the spread-out nature of the DS-DS time histogram could be explained as being two time distributions superimposed on top of one another, one for each route taken. In general, water from the DS moves slowest (around 4 cm/s), while that from the FSC is fastest (about 7 cm/s). This is due to a variety of factors, including different wind forcings, density structures, transport depths, and driving processes between the two regions.

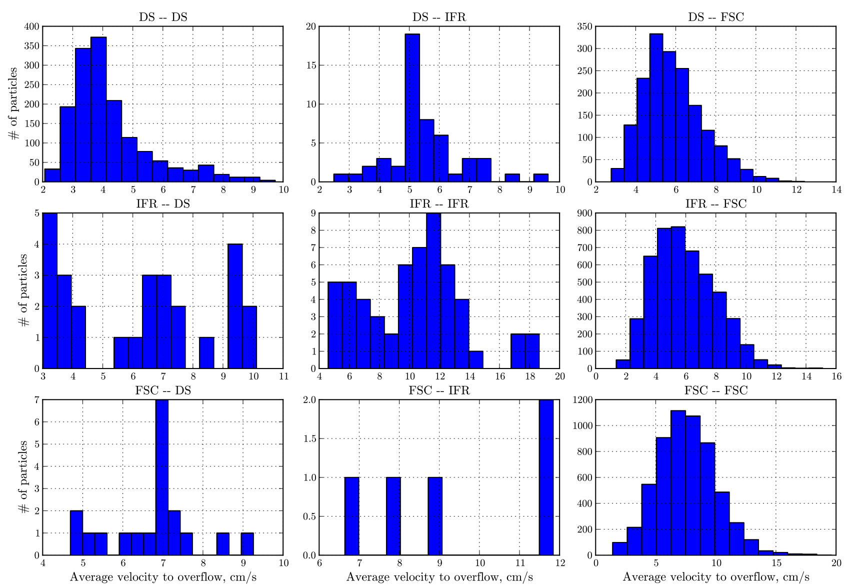

Figure 3.21: Average velocity of particles for all inflow-outflow strait pairings from start to overflow.

3.3.3 Overflow Properties

Now that we have a relatively clear picture of the paths taken by particles which exit the GIN seas as non-surface water within a three-year timespan, let us examine the evolution of properties in that water. I shall focus on the depth and density distributions here, and only discuss those strait pairs which export significant volumes of water – that is, DS-DS, DS-FSC, IFR-FSC, and FSC-FSC. The other pairs either don't have any particles actually overflowing (IFR-IFR, FSC-IFR), or export in such small and irregular numbers that statistics, and any conclusions made from those statistics, would be questionable at best (DS-IFR, IFR-DS, FSC-DS).

I have shown the mean and standard deviation for both depth and density distributions for all strait pairings in table 3.6. Note that the values for "N" in this table differ from those in table 3.5. This is because, as discussed in the previous section, there were some computational problems in determining the time-to-overflow, and therefore also the distance-to-overflow, values for subsets of particles in both the DS-DS and FSC-FSC pairings. Only those particles whose overflow times were properly found are used for the statistics in table 3.6.

Denmark Strait - Denmark Strait

Let us begin with the Denmark Strait – Denmark Strait pairing, whose depth and density distributions are shown in figure 3.22. Water which will eventually overflow here is initially quite shallow and concentrated in a relatively thin layer (actually, at 122$\pm$47 m, it's the shallowest and nearly the most concentrated initial water mass of the four major pairings). By the time they exit, however, the particles have sunk well over 250 m (392$\pm$103 m), compared to a mean strait depth of 600 m. Therefore, the outflowing particles are not really true deep overflow water. That said, as they flow down the slope into the Atlantic, they do attain the greatest average depth of all particles from the four pairs at 1086$\pm$480 m, with the most extreme attaining about 2500 m.

In	Out	N	Depth, m		
			Start	Overflow	Downstream
DS	DS	1552	122±47	392±103	1086±480
IFR		27	179±110	306±82	724±495
FSC		19	185±120	318±66	641±357
DS	IFR	51	136±34	309±63	866±480
IFR		56	173±75	356±159	555±435
FSC		5	200±108	542±18	688±228
DS	FSC	1744	130±43	446±146	789±241
IFR		4795	200±79	340±141	749±239
FSC		5755	321±144	526±127	793±249

			Potential Density $\sigma_{1.0}$, kg/m^3		
			Start	Overflow	Downstream
DS	DS	1552	31.92±0.19	32.42±0.22	32.32±0.10
IFR		27	31.76±0.11	32.33±0.25	32.21±0.14
FSC		19	31.66±0.13	32.45±0.20	32.22±0.11
DS	IFR	51	32.03±0.13	32.17±0.15	32.26±0.17
IFR		56	31.75±0.15	31.83±0.17	32.16±0.16
FSC		5	31.59±0.09	32.20±0.07	32.30±0.08
DS	FSC	1744	31.96±0.17	32.23±0.24	32.24±0.17
IFR		4795	31.79±0.13	32.05±0.23	32.22±0.19
FSC		5755	31.70±0.13	32.11±0.32	32.25±0.17

Table 3.6: Summary of particle depth and density properties. "Start" values are the mean ± standard deviation at initialization; "Overflow" values are those upon entering the first green box; "Downstream" values are those 750 km in a strait line from the "Overflow" location. Densities are referenced to 1000 m.

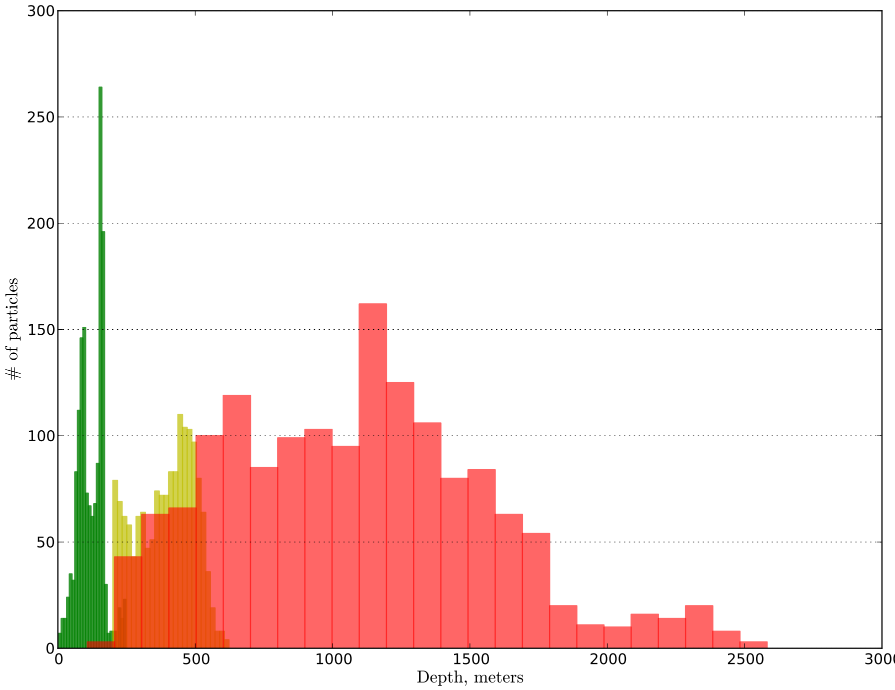

(a) Depth distribution

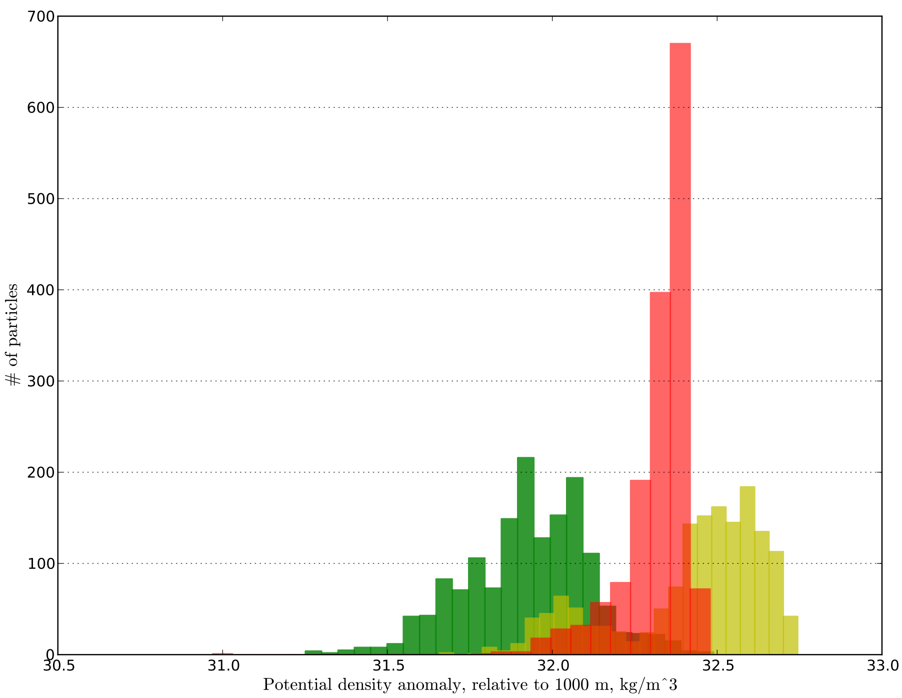

(b) Potential density anomaly distribution

Figure 3.22: Depth and potential density (referenced to 1000 m) distributions for particles which both enter and exit through the **Denmark Strait**. Green bars represent the distribution upon insertion; yellow the distribution at overflow; red the distribution 750 km downstream from overflow.

This great depth is achieved through the simple expedient of high density. The particles flowing into the Denmark Strait, in fact, are the densest of the three inflows: $\sigma_{1.0} = 31.92 \pm 0.19\,\mathrm{kg/m^3}$, versus $31.76 \pm 0.11\,\mathrm{kg/m^3}$ for those in the IFR. The subsequent evolution of this value, however, is more difficult to explain. Between inflow and overflow, the water mass gains a significant amount of salt – 34.56±0.19 to 34.80±0.11. It is also cooled, dropping from 4.8±1.2°C to 2.2±1.6°C. Both of these factors cause the density to increase to $\sigma_{1.0} = 32.42 \pm 0.22\,\mathrm{kg/m^3}$ by the time the particles overflow, easily making it the densest of the major outflows (as first guessed at in section 3.1.3). As these particles mix with their surroundings after exiting the strait, they continue to gain a bit of salt (increasing their salinity to 34.94±0.08) while warming again to near their original temperature (4.1±0.7°C). The net result is a downstream potential density of $\sigma_{1.0} = 32.32 \pm 0.10\,\mathrm{kg/m^3}$, or about $0.1\,\mathrm{kg/m^3}$ less than at overflow.

Denmark Strait - Faroe-Shetland Channel

The depth and density distributions for these particles are shown in figure 3.23. This water again starts off quite shallow, at 130±43 m. That said, it is also the densest, at $\sigma_{1.0} = 31.96 \pm 0.17\,\mathrm{kg/m^3}$. This is slightly greater than the DS-DS water, likely since it tends to be nearer the core of the jet than DS-DS water. Its overflow depth tends to be greater than DS-DS water as well, at 446±46 m. This, however, is likely due not to its (marginally) greater initial density, but to the larger distance it travels (2200 km, vs. 1600 km). Most of the $0.27\,\mathrm{kg/m^3}$ increase in density between start and overflow is due to an increase in salt – temperature remains, for all intents and purposes, constant.

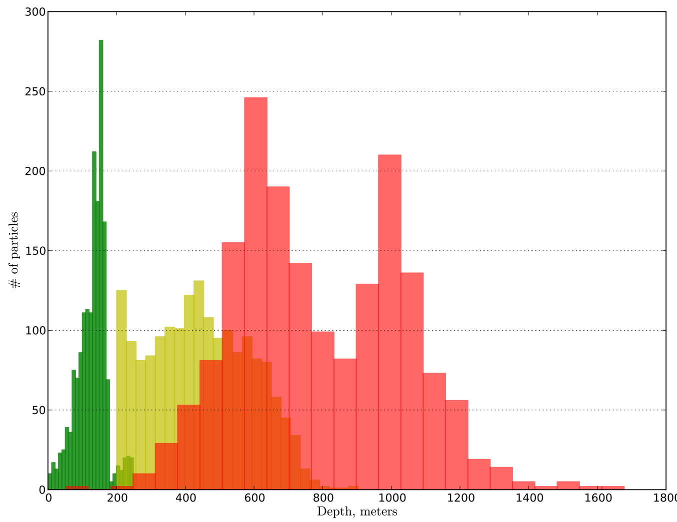

(a) Depth distribution

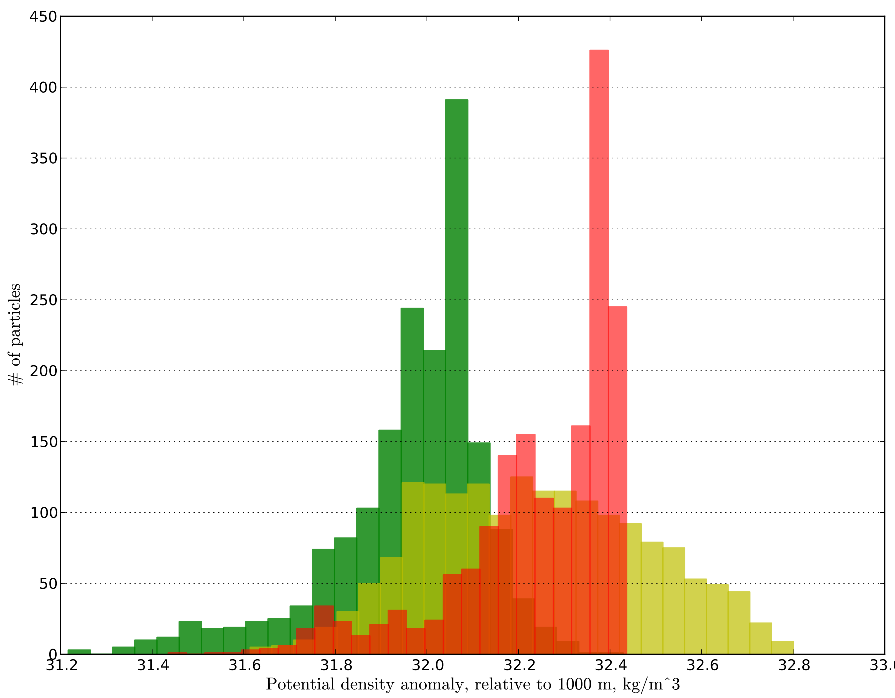

(b) Potential density anomaly distribution

Figure 3.23: Depth and potential density (referenced to 1000 m) distributions for particles which enter through the **Denmark Strait** and exit through the **Faroe-Shetland Channel**. Green bars represent the distribution upon insertion; yellow the distribution at overflow; red the distribution 750 km downstream from overflow.

Both of these effects are likely due to the relatively warm, salty water it flows next to as it travels south.

In contrast to its DS-DS compatriot, the DS-FSC water tends to stay nearer its overflow depth after exiting the FSC. Where the DS-DS water sinks nearly 700 m after crossing the Greenland-Scotland Ridge, this mass sinks a mere 300 m, and extends over a smaller depth range. In addition, its density stays nearly constant. Both of these facts suggest that it does not experience much downslope mixing or entrainment upon entering the Atlantic.

Iceland-Faroe Ridge - Faroe-Shetland Channel

Water here (distributions shown in figure 3.24) starts off with a density slightly less than that for the outflows of DS origin ($\sigma_{1.0} = 31.8$ vs. 31.95 kg/m^3) despite being saltier (35.0 vs. 34.5), mostly due to being four degrees warmer (8° vs. 4°C). It also begins 70 m deeper. It maintains a 0.17 kg/m^3 density advantage at overflow, but loses the depth advantage – despite having started nearer the surface, as the Denmark Strait water flowed south its comparatively high density makes it inevitable it will sink much deeper than its warmer surroundings. In fact, the mean depth shown in table 3.6 for the IFR-FSC water actually understates this fact – the statistical depth value of 340$\pm$141 m is correct due to the data's long tail, but the histogram clearly shows that much of the water is concentrated between 200 and 300 m.

After overflow, the differences between DS-FSC and IFR-FSC water disappears. 750 km downstream, they occupy essentially the same depth ranges (500-1100 m), and possess the essentially same densities ($\sigma_{1.0} = 32.24 \pm$

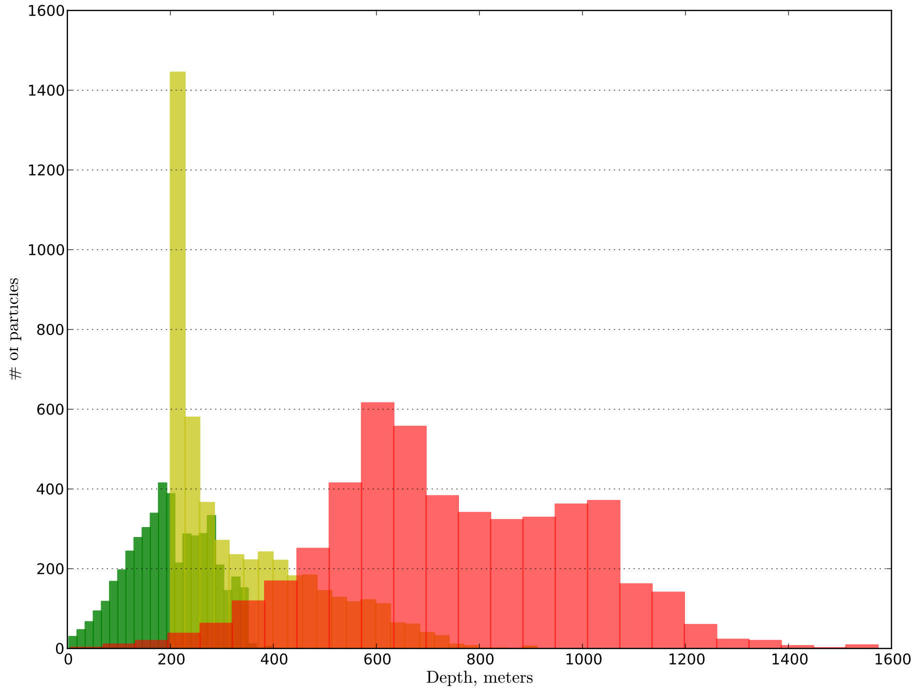

(a) Depth distribution

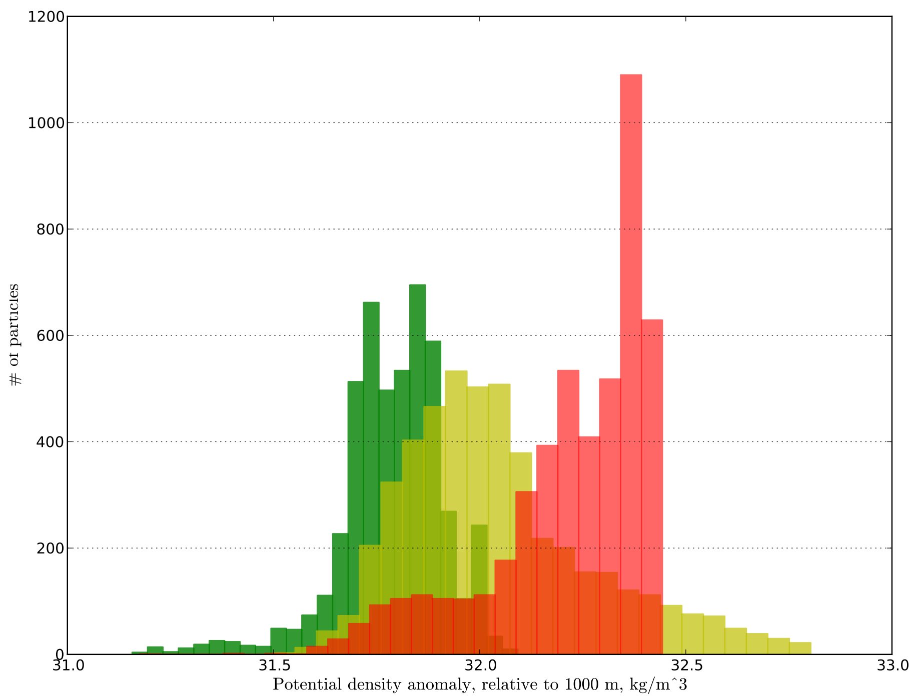

(b) Potential density anomaly distribution

Figure 3.24: Depth and potential density (referenced to 1000 m) distributions for particles which enter over the **Iceland-Faroe Ridge** and exit through the **Faroe-Shetland Channel**. Green bars represent the distribution upon insertion; yellow the distribution at overflow; red the distribution 750 km downstream from overflow.

$0.17\,\mathrm{kg/m^3}$ and $32.22 \pm 0.19\,\mathrm{kg/m^3}$, respectively).

Faroe-Shetland Channel - Faroe-Shetland Channel

This water starts off fully 0.1 saltier (35.18±0.07), but only 1°C warmer (9.1±0.7°C), than that following the IFR-FSC route, and as a result is $0.1\,\mathrm{kg/m^3}$ denser ($\sigma_{1.0} = 31.70 \pm 13\,\mathrm{kg/m^3}$). In addition, it is distributed practically evenly over the top 600 m of the strait, as shown (along with its density distribution) in figure 3.25. Unlike the IFR-FSC water, however, when these FSC-FSC particles exit their median depth is quite similar to the mean of 526±127 m. This is 180 m deeper than the mean of the IFR-FSC overflow (though the difference in median values is greater, at around 300 m), and is even deeper than the DS-FSC water. However, since the detection box for the FSC-FSC flow is necessarily further west than that for the DS-FSC and IFR-FSC water, the FSC-FSC mass will have had time to mix with its surroundings (decreasing its density), and will have already flowed partway down the slope into the Atlantic.

In addition, downstream of the overflow the particles once again attain depth and density characteristics very similar to their DS-FSC and IFR-FSC compatriots – 793±249 m and $\sigma_{1.0} = 32.25 \pm 0.17\,\mathrm{kg/m^3}$. This means that particles from the three different sources, after having exited through the FSC, have average depths within 50 m, and average densities within $0.03\,\mathrm{kg/m^3}$, of one another by the time they reach the Reykjanes Ridge. The distributions of these values are also similar. Evidently all three water masses are mixing with each other just after exiting the FSC, entraining little extra water and causing their own properties to converge. Crucially, the resulting density is still low

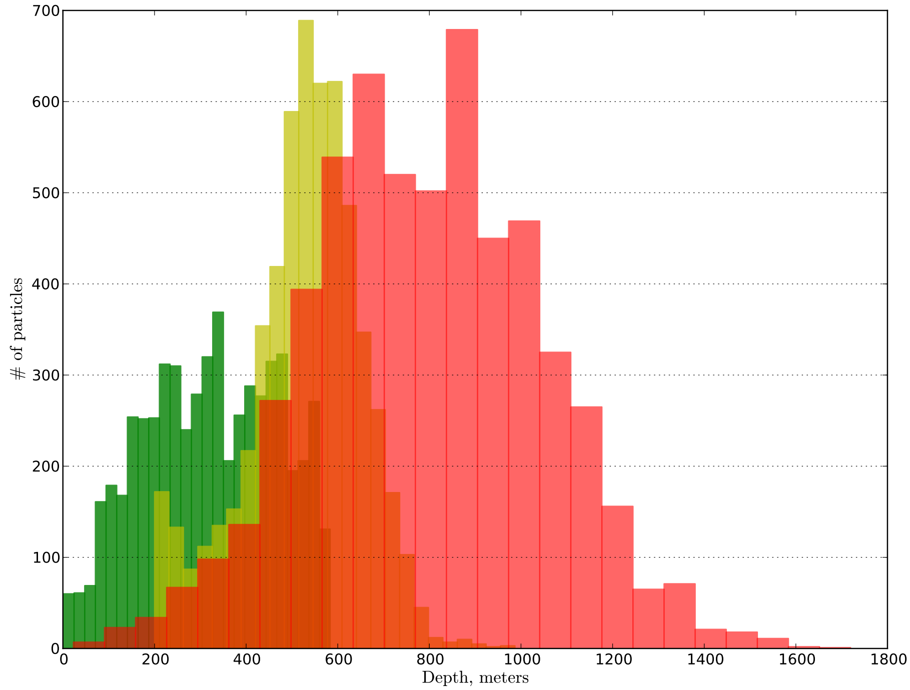

(a) Depth distribution

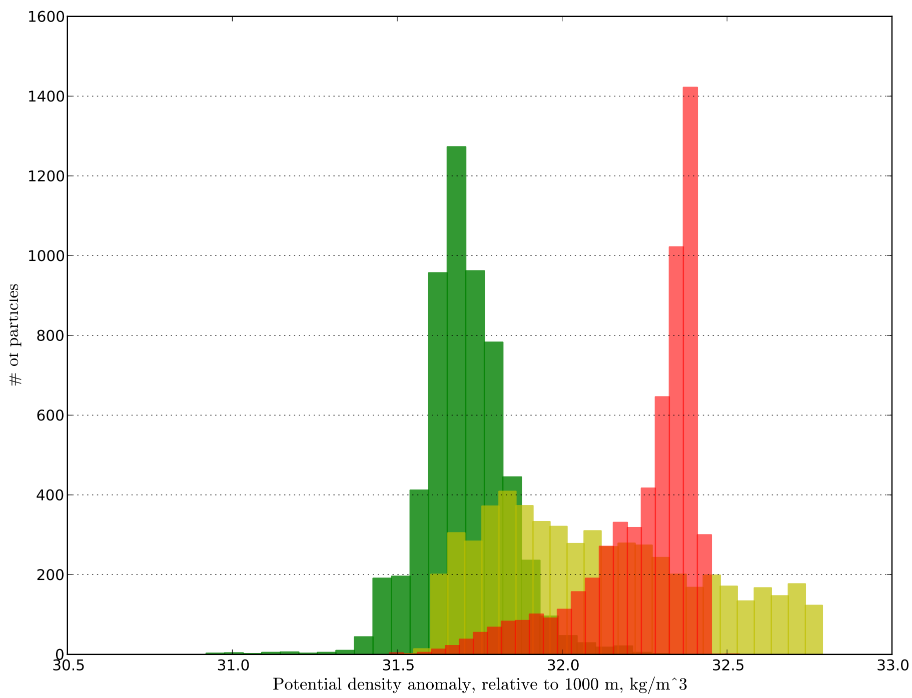

(b) Potential density anomaly distribution

Figure 3.25: Depth and potential density (referenced to 1000 m) distributions for particles which both enter and exit through the **Faroe-Shetland Channel**. Green bars represent the distribution upon insertion; yellow the distribution at overflow; red the distribution 750 km downstream from overflow.

enough that the new mass does not sink below 1000 m, thus preventing its becoming part of the deep overflow. In fact, this behaviour is a well-known problem with models in general (Legutke & Maier-Reimer, 2002) – most mixing occurs along isopycnals in the horizontal, instead of across isopycnals in the vertical. Attempts to solve this issue have so far been largely unsuccessful.

As a result of this mixing, it is largely meaningless to infer anything about the history of particles after they exit through the FSC – in reality, they will have rather different depth and property values than those calculated by the model.

Chapter 4

Summary

In the first stage of this thesis, it was found that the NEMO ORCA025 model, in its KAB001 configuration, performs acceptably well in terms of horizontal currents and properties. No long-term trends in volume transports into and out of the Nordic Seas across the Greenland-Scotland Ridge were found, which in the case of the deep flows at least is in agreement with (Hansen & Østerhus, 2000). However, the model is not optimal for representing vertical processes such as deep convection, most notably in the Greenland Sea where numerous observations (Schott et al. (1993); Rudels et al. (1989); Visbeck et al. (1995); Watson et al. (1999)) confirm the occurrence of that process. Therefore, the remainder of the study concentrated on the formation of intermediate water masses which, due to their formation over longer timescales of weeks to months (rather than hours to days as with deep convection) and less vigorous vertical motion (i.e. much less than deep convection's 4 cm/s), are quite well-represented in the model.

Of the particles inserted in the Ariane particle tracking experiments, only 5.6% flowed out again over the Greenland-Scotland Ridge below 200 m within the three-year span of each experiment. Most of this flow was through the Faroe-Shetland Channel; only the Denmark Strait inflow flowed back out through the Denmark Strait, accounting for 11% of the total particle outflow. The Denmark Strait inflow contributed an additional 13% to the total particle outflow when it exited the Faroe-Shetland Channel, while inflow over the Iceland-Faroe Ridge contributed 35% by exiting through its southern neighbour. Particles both entering and exiting the Faroe-Shetland Channel, however, dominated the outflow, accounting for 42% of the total. Almost no particles exited over the Iceland-Faroe Ridge, the exception being a random few from the Denmark Strait which crossed over the northern rift in the IFR. The other strait pairings were not significant.

Water properties at overflow related to each other as expected – DS-DS water was the coldest (2.23±1.56°C) and densest ($\sigma_{1.0} = 32.42 \pm 0.22\,\mathrm{kg/m^3}$), while the FSC-FSC variety was the saltiest (35.06±0.11) and nearly the warmest (6.01±2.68°C). Inflow salinities were generally found to be too low by about 0.5, while temperature was fairly well represented (Hansen et al., 2003; Rudels et al., 1999). After exiting the Nordic Seas, particles became mixed as they travelled downstream. During this phase, those particles which exited Denmark Strait sank deepest to around $1100 \pm 480\,\mathrm{m}$. The Faroe-Shetland water, however, sank to only $750 \pm 250\,\mathrm{m}$.

Water mass transformations occurred mainly in or near boundary currents (e.g. the Iceland Sea gyre, the North Icelandic Irminger Current), with some also taking place over the extreme southern end of the Norwegian basin. Most particles which underwent these transformations did so in what appeared to be an eddy-like flow, wherein they meandered somewhat. This less-than-direct path likely allowed them to experience greater heat loss to the atmosphere and become denser than their surroundings, causing them to join the intermediate-level outflows.

The lack of true convective sites suggests that work still needs to be done on representations of vertical instability – the widely varying scales involved make this difficult, yet the formation of deep water in convective cells is rather important to the overall dynamics of the ocean, especially over longer timescales. The problem of relating small-scale processes to larger scales is also shown by the poorly represented downstream mixing of particles after exiting over the Greenland-Scotland Ridge. Despite this, most "normal" (i.e. processes which are mostly horizontal or of limited vertical scale) are represented quite well by the model.

The numbers of particles which exited over the Greenland-Scotland Ridge at the middle depths suggests that in addition to deep outflow, the Nordic Seas may also export significant amounts of mid-depth water which has transformed in boundary currents instead of gyre interiors. The trajectories produced by these outflowing particles suggest that most of this mid-depth outflow in the Denmark Strait actually originates from water transformed in the boundary currents of the Iceland Sea, with very little being contributed by water of North Atlantic Current origin from the two southern straits. They also show that the FSC gathers its export waters from many sources, including the boundary currents from the two northern straits and water masses transformed in the southern Norwegian Sea. Conclusions as to what other water masses may mix with the North Atlantic Current masses, however, are difficult to draw.

In total, the FSC is the larger exporter of Nordic Seas-derived mid-level and deep water, likely due to its larger number of sources and deeper maximum depth when compared to the Denmark Strait (though in the model the mesh around this region has been hand-edited to better reproduce the observed outflows, with the result that it is slightly deeper than the FSC). By contrast, the Iceland-Faroe Ridge exports very little deep water as a consequence of its relatively shallow depth simply forming an impenetrable barrier to such flows.

These conclusions are tempered by several items that could be improved in my analysis, however. Perhaps the most obvious is the way in which I defined North Atlantic Current water, with fixed lower limits. The Hövmoller plots shown in figures 3.11 to 3.13 clearly show that this lower limit is not fixed, changing both seasonally and decadally. A better way of defining that water mass may be placing a limit on potential density, while keeping the requirement for an inward-flowing current.

The number and frequency of particles inserted could also be improved. While 2000 is certainly enough to get an idea for what various circulation patterns look like, as many as 10,000 would allow even better statistics to be produced. In addition, running an experiment in each season of each year, or every two years, instead of merely every four, would go a long way to reducing potential issues with aliasing and/or undersampling.

Finally, there is the model itself. As mentioned previously, it currently does not accurately represent the dynamics of deep convection in this region, or turbulent mixing in general. Also, this configuration accidently omitted the effects of katabatic winds (DRAKKAR Group, 2010), a potentially important driver of convection in seas near the Greenland ice sheet, and uses strong sea surface salinity restoration north of Fram Strait, potentially impacting the properties of water masses influenced by the East Greenland Current.

Therefore, I see two ways in which to continue this work. First, refine the definition of North Atlantic Current water and the setup scheme of the Ariane experiments. Second, try the same experiments with a different model, perhaps one that does not restore so heavily in the Arctic. This would give insight into the generality of my conclusions, whether or not they are, indeed, applicable to reality or if they are simply signatures of the KAB001 model configuration. The issue of missing convection is common to most modern models, and is a separate issue to be solved on its own.

In short, this study examines when, where, and how North Atlantic Current inflow evolves within the Nordic Seas to intermediate and deep outflow water. Classically, much of this outflow was thought to have formed directly through deep convection of North Atlantic Current water in the centres of gyres. However, this study shows that very little, if any, water enters the gyre interiors, and that none at all becomes part of the deep flows (mainly due to the model's poor representation of deep-convection). Instead, significant portions (5.6%) of the inflow were transformed within the boundary currents to mid-depth masses (300-500 m), which were subsequently transported across the Greenland-Scotland Ridge primarily by the FSC. Assuming Mauritzen (1996b)'s nominal 8 Sv of total North Atlantic Current inflow, one can then predict about 0.45 Sv of North Atlantic Current water undergoing such transformations compared to Hansen & Østerhus (2000)'s 6 Sv estimate of total intermediate and deep outflow. Therefore, this study shows that much, if not most, of the intermediate and deep outflow is formed either in the Arctic Ocean or from Arctic outflow.

Bibliography

Aagaard, K., Swift, J., & Carmack, E. (1985). Thermohaline Circulation in the Arctic Mediterranean Seas. *Journal of Geophysical Research*, *90*(C3), 4833–4846.

Aksenov, Y., Bacon, S., Coward, A. C., & Holliday, N. P. (2010). Polar outflow from the Arctic Ocean: A high resolution model study. *Journal of Marine Systems*, *83*, 14–37.

Arakawa, A. (1966). Computational Design for Long-Term Numerical Integration of the Equations of Fluid Motion: Two-Dimensional Incompressible Flow. Part 1. *Journal of Computational Physics*, (1), 119–143.

Bjerknes, J. (1969). Atmospheric Teleconnections from the Equatorial Pacific. *Monthly Weather Review*, *97*(3), 163–172.

Blanke, B., & Raynaud, S. (1997). Kinematics of the Pacific Equatorial Undercurrent: An Eulerian and Lagrangian Approach from GCM Results. *Journal of Physical Oceanography*, *27*(6), 1038–1053.

Bouillon, S., Maqueda, M. A. M., Legat, V., & Fichefet, T. (2009). An elastic-viscous-plastic sea ice model formulated on Arakawa B and C grids. *Ocean Modelling*, *27*(3-4), 174–184.

Bryan, F. O., & Danabasoglu, G. (2006). Respone of the North Atlantic

Thermohaline circulation and Ventilation to Increasing Carbon Dioxide in CCSM3. *Journal of Climate*, *19*, 2382–2397.

Chelton, D. B., deSzoeke, R. A., Schlax, M. G., El Naggar, K., & Siwertz, N. (1998). Geographical Variability of the First Baroclinic Rossby Radius of Deformation. *Journal of Physical Oceanography*, *28*, 433–460.

Deacu, D., & Myers, P. G. (2005). Effect of a Variable Eddy Transfer Coefficient in an Eddy- Permitting Model of the Subpolar North Atlantic Ocean. *Journal of Physical Oceanography*, *35*, 289–307.

Dickson, R., Rudels, B., Dye, S., Karcher, M., Meincke, J., & Yashayaev, I. (2007). Current estimates of freshwater flux through Arctic and subarctic seas. *Progress in Oceanography*, *73*, 210–230.

DRAKKAR Group (2007). Eddy-permitting Ocean Circulation Hindcasts of past decades. *CLIVAR Exchanges*, *42*(12), 8–10.

DRAKKAR Group (2010). The DRAKKAR project: The ocean circulation in the North Atlantic and the Nordic seas: Variability, processes and interactions with the global ocean. Website.
URL `http://www-meom.hmg.inpg.fr/Web/Projets/DRAKKAR/`

Emile-Geay, J., & Madec, G. (2008). Geothermal heating, diapycnal mixing and the abyssal circulation. *Ocean Science Discussions*, *5*(3), 281–325.
URL `http://www.ocean-sci-discuss.net/5/281/2008/`

Encyclopædia Britannica (2010). Ocean. Website.
URL `http://www.britannica.com/EBchecked/topic/424285/ocean`

Feltham, D. L. (2008). Sea Ice Rheology. *Annual Review of Fluid Mechanics*, *40*, 91–112.

Feng, M., Biastoch, A., Böning, C., Caputi, N., & Meyers, G. (2008). Seasonal and interannual variations of upper ocean heat balance off the west coast of Australia. *Journal of Geophysical Research*, *113*, C12025.

Fofonoff, N., & Millard Jr., R. (1983). Algorithms for computation of fundamental properties of seawater. Tech. Rep. 44, Unesco technical papers in marine science. 53 pp.

Foldvik, A., & Gammelsrød, T. (1988). Notes on Southern Ocean hydrography, sea-ice and bottom water formation. *Palaeogeography, Palaeoclimatology, Palaeoecology*, *67*, 3–17.

Foldvik, A., Gammelsrød, T., & Tørresen, T. (1985). Physical oceanography studies in the Weddell Sea during the Norwegian Antarctic Research Expedition 1978/79. *Polar Research*, *3*, 195–207.

GMM02 Group (2004). GRACE Gravity Model GGM02. Tech. rep., Center for Space Research, University of Texas at Austin.

Griffies, S. M., & et. al. (2009). Coordinated Ocean-ice Reference Experiments (COREs). *Ocean Modelling*, *26*(1-2), 1–46.

Haidvogel, D. B., & Beckmann, A. (1999). *Numerical Ocean Circulation Modeling*, vol. 2 of *Series on environmental science and management*. Imperial College Press.

Haine, T. W. N., Watson, A. J., Liddicoat, M. I., & Dickson, R. R. (1998). The flow of Antarctic bottom water to the southwest Indian Ocean estimated using CFCs. *Journal of Geophysical Research*, *103*(C12), 27637–27653.

Halliday, D., Resnick, R., & Walker, J. (2001). *Fundamentals of Physics*, chap. 2, (p. 18). John Wiley & Sons, 6 ed.

Hansen, B., & Østerhus, S. (2000). North Atlantic - Nordic Seas exchanges. *Progress in Oceanography*, *45*, 109–208.

Hansen, B., Østerhus, S., Hátún, H., Kristiansen, R., & Larsen, K. M. H. (2003). The Iceland-Faroe inflow of Atlantic water to the Nordic Seas. *Progress in Oceanography*, *59*, 443–474.

Hansen, B., Turrell, W. R., & Østerhus, S. (2001). Decreasing overflow from the Nordic seas into the Atlantic Ocean through the Faroe Bank channel since 1950. *Nature*, *411*, 927–930.

Hátún, H., & McClimans, T. A. (2003). Monitoring the Faroe Current using altimetry and coastal sea-level data. *Continental Shelf Research*, *23*, 859–868.

Hurrell, J. W., & Deser, C. (2009). North Atlantic climate variability: The role of the North Atlantic Oscillation. *Journal of Marine Systems*, *78*, 28–41.

Jackett, D. R., & McDougall, T. J. (1995). Minimal Adjustment of Hydrographic Profiles to Achieve Static Stabilities. *Journal of Atmospheric and Oceanic Technology*, *12*, 381–389.

Joint WHO/FAO Expert Consultation on Diet, Nutrition and the Prevention of Chronic Diseases (2003). Diet, nutrition and the prevention of chronic diseases. Tech. Rep. 916, World Health Organization, Geneva, Switzerland.

Jones, H., & Marshall, J. (1997). Restratification after Deep Convection. *Journal of Physical Oceanography*, *27*, 2276–2287.

Khatiwala, S., Schlosser, P., & Visbeck, M. (2002). Rates and Mechanisms of Water Mass Transformations in the Labrador Sea as Inferred from Tracer Observations. *Journal of Physical Oceanography*, *32*, 666–686.

Kieke, D., & Rhein, M. (2006). Variability of the Overflow Water Transport in the Western Subpolar North Atlantic, 1950-97. *Journal of Physical Oceanography*, *36*, 435–456.

Knutsen, Ø., Svendsen, H., Østerhus, S., Rossby, T., & Hansen, B. (2005). Direct measurements of the mean flow and eddy kinetic energy structure of the upper ocean circulation in the NE Atlantic. *Geophysical Research Letters*, *32*(14), L14604.

Koch-Larrouy, A., Madec, G., Bouruet-Aubertot, P., Gerkema, T., Bessières, L., & Molcard, R. (2007). On the transformation of Pacific Water into Indonesian Throughflow Water by internal tidal mixing. *Geophysical Research Letters*, *34*, L04604.

Kundu, P. K., & Cohen, I. M. (2008). *Fluid Mechanics*. Academic Press, 4th ed.

Large, W., & Yeager, S. (2004). Diurnal to decadal global forcing for ocean and sea-ice models: the data sets and flux climatologies. Tech. Rep. NCAR/TN-460+STR, NCAR Technical Note.

Lavery, T. J., Roudnew, B., Gill, P., Seymour, J., Seuront, L., Johnson, G., Mitchell, J. G., & Smetacek, V. (2010). Iron defecation by sperm whales stimulates carbon export in the Southern Ocean. *Proceedings of the Royal Society B*, *277*(1699), 3527–3531.

Lazure, P., Garnier, V., Dumas, F., Herry, C., & Chifflet, M. (2009). Development of a hydrodynamic model of the Bay of Biscay. Validation of hydrology. *Continental Shelf Research*, *29*(8), 985–997.

Legutke, S., & Maier-Reimer, E. (2002). The impact of a downslope water-transport parameterization in a global ocean general circulation model. *Climate Dynamics*, *18*, 611–623.

Lide, D. R. (Ed.) (2000). *Handbook of Chemistry and Physics*. CRC, 81 ed.

Lipscomb, W. H. (2001). Remapping the thickness distribution in sea ice models. *Journal of Geophysical Research*, *106*(C7), 13989–14000.

Madec, G. (2008). *NEMO Ocean Engine Manual*.

Marshall, J., & Schott, F. (1999). Open-Ocean Convection: Observation, Theory, and Models. *Reviews of Geophysics*, *37*(1), 1–64.

Mauritzen, C. (1996a). Production of dense overflow waters feeding the North Atlantic across the Greenland-Scotland Ridge. Part 1: Evidence for a revised circulation scheme. *Deep-Sea Research 1*, *43*(6), 769–806.

Mauritzen, C. (1996b). Production of dense overflow waters feeding the North Atlantic across the Greenland-Scotland Ridge. Part 2: An inverse model. *Deep-Sea Research 1*, *43*(6), 807–835.

Minobe, S., Kuwano-Yoshida, A., Komori, N., Xie, S.-P., & Small, R. J. (2008). Influence of the Gulf Stream on the troposphere. *Nature*, *452*, 206–209.

Molines, J. M., Barnier, B., Penduff, T., Brodeau, L., Treguier, A.-M., Theetten, S., & Madec, G. (2006). Definition of the 45 years interannual experiment ORCA025-G70. Tech. rep., DRAKKAR Group.

Molines, J. M., Treguier, A.-M., & Theetten, S. (2004). Drakkar ORCA025-2004 experiments. Tech. rep., DRAKKAR Group. 2$^{\text{nd}}$ Draft.

National Oceanic and Atmospheric Administration (2010). Ocean. Website. URL `http://www.noaa.gov/ocean.html`

Newman, P. (1989). *Company of Adventurers*. Penguin Canada.

NODC (1998). World Ocean Atlas 1998. Tech. rep., NOAA, US Department of Commerce.

Nowlin Jr., W. D., Whitworth III, T., & Pillsbury, R. D. (1977). Structure and Transport of the Antarctic Circumpolar Current at Drake Passage from Short-Term Measurements. *Journal of Physical Oceanography*, *7*, 788–802.

Orsi, A. H., Whitworth III, T., & Nowlin Jr., W. D. (1995). On the meridional extent and fronts of the Antarctic Circumpolar Current. *Deep-Sea Research I*, *42*(5), 641–673.

Pickard, G. L., & Emery, W. J. (1990). *Descriptive Physical Oceanography*. Pergamon Press, 5th ed.

Reverdin, G., Cayan, D., & Kushnir, Y. (1997). Decadal variability of hydrography in the upper northern North Atlantic in 1948-1990. *Journal of Geophysical Research*, *102*(C4), 8505–8531.

Roberts, J. L., Heil, P., Murray, R. J., Holloway, D. S., & Bindoff, N. L. (2006). Pole relocation for an orthogonal grid: An analytic method. *Ocean Modelling*, *12*, 16–31.

Rudels, B., Eriksson, P., Grönvall, H., Hietala, R., & Launiainen, J. (1999). Hydrographic Observations in Denmark Strait in Fall 1997, and their Implications for the Entrainment into the Overflow Plume. *Geophysical Research Letters*, *26*(9), 1325–1328.

Rudels, B., Quadfasel, D., Friedrich, H., & Houssais, M.-N. (1989). Greenland Sea Convection in the winter of 1987-1988. *Journal of Geophysical Research*, *94*(C3), 3223–3227.

Sarmiento, J., & Gruber, N. (2002). Sinks for Anthropogenic Carbon. *Physics Today*, *55*(8), 30–36.

Sarmiento, J., Gruber, N., Brzezinski, M., & Dunne, J. (2004). High-latitude controls of thermocline nutrients and low latitude biological productivity. *Nature*, *427*, 56–60.

Schott, F., Visbeck, M., & Fischer, J. (1993). Observations of Vertical Currents and Convection in the Central Greenland Sea During the Winter of 19881989. *Journal of Geophysical Research*, *98*(C8), 14401–14421.

Schumacher, J. D., Stabeno, P. J., & Roach, A. T. (1989). Volume transport in the Alaska Coastal Current. *Continental Shelf Research*, *9*(12), 1071–1083.

Serra, N., Käse, R. H., Köhl, A., Stammer, D., & Quadfasel, D. (2010). On the low-frequency phase relation between the Denmark Strait and the Faroe-Bank Channel overflows . *Tellus A*, *62*, 530–550.

Smith, R. D., & Gent, P. R. (2004). Anisotropic GentMcWilliams Parameterization for Ocean Models. *Journal of Physical Oceanography*, *34*, 2541–2564.

Smith, W. H., & Sandwell, D. T. (1997). Global Sea Floor Topography from Satellite Altimetry and Ship Depth Soundings. *Science*, *277*(5334), 1956–1962.
URL `http://www.sciencemag.org/cgi/content/abstract/277/5334/1956`

Stommel, H., & Yoshida, K. (Eds.) (1972). *Kuroshio: Physical Aspects of the Japan Current*. University of Washington Press.

Straneo, F. (2006). Heat and Freshwater Transport through the Central Labrador Sea. *Journal of Physical Oceanography*, *36*, 606–628.

Tanhua, T., Olsson, K. A., & Jeansson, E. (2005). Formation of Denmark Strait overflow water and its hydro-chemical composition. *Journal of Marine Systems*, *57*, 264–288.

Tapley, B., Ries, J., Bettadpur, S., Chambers, D., Cheng, M., Condi, F., Gunter, B., Kang, Z., Nagel, P., Pastor, R., Pekker, T., Poole, S., & Wang, F. (2005). GGM02 - An improved Earth gravity field model from GRACE. *Journal of Geodesy*, *79*(8), 467–478.

Taylor, A. H., & Stephens, J. A. (1998). The North Atlantic Oscillation and the latitude of the Gulf Stream. *Tellus A*, *50*(1), 134–142.

Thiede, J., Pfirman, S., Schenke, H.-W., & Reil, W. (1990). Bathymetry of Molloy Deep: Fram Strait between Svalbard and Greenland. *Marine Geophysical Researches*, *12*(3), 197–214.

Tilstone, G. H., Figueiras, F. G., & Fraga, F. (1994). Upwelling-downwelling sequences in the generation of red tides in a coastal upwelling system. *Marine Ecology Progress Series*, *112*, 241–253.

Tsimplis, M., Marcos, M., Somot, S., & Barnier, B. (2008). Sea level forcing in the Mediterranean Sea between 1960 and 2000. *Global and Planetary Change*, *63*(4), 325–332.

Ueda, H., & Yasunari, T. (1996). Maturing Process of the Summer Monsoon over the Western North Pacific – A coupled Ocean/Atmosphere System. *Journal of the Meteorological Society of Japan*, *74*(4), 493–508.

Visbeck, M., Fischer, J., & Schott, F. (1995). Preconditioning the Greenland Sea for deep convection: Ice formation and ice drift. *Journal of Geophysical Research*, *100*(C9), 18489–18502.

Voituriez, B. (2006). *The Gulf Stream*. IOC Ocean Forum Series. UNESCO Publishing.

Watson, A., Messias, M.-J., Fogelqvist, E., Van Scoy, K., Johannessen, T., Oliver, K., Stevens, D., Rey, F., Tanhua, T., Olsson, K., Carse, F., Simonsen, K., Ledwell, J., Jansen, E., Cooper, D., Kruepke, J., & Guilyardi, E. (1999). Mixing and convection in the Greenland Sea from a tracer-release experiment. *Nature*, *40*, 902–904.

Whipple, A. (Ed.) (1980). *The Clipper Ships*. The Seafarers. Time-Life Books.

Williams, R. G., & Follows, M. J. (1998). The Ekman transfer of nutrients and maintenance of new production over the North Atlantic. *Deep Sea Research I*, *45*, 461–489.

Wong, G. S., & Zhu, S.-m. (1995). Speed of sound in seawater as a function of salinity, temperature, and pressure. *Journal of the Acoustical Society of America*, *97*(3), 1732–1736.

Yashayaev, I., & Loder, J. W. (2009). Enhanced production of Labrador Sea Water in 2008. *Geophysical Research Letters*, *36*, L01606.